

**HYDROKINETIC POWER HARNESSING UTILIZING  
VORTEX INDUCED VIBRATIONS THROUGH A  
VIRTUAL c-k VIVACE MODEL**

by

Jonghun Lee

A dissertation submitted in partial fulfillment  
of the requirements for the degree of  
Doctor of Philosophy  
(Naval Architecture and Marine Engineering)  
in The University of Michigan  
2010

**Doctoral Committee:**

Professor Michael M. Bernitsas, Chair  
Professor Armin W. Troesch  
Professor Jing Sun  
Associate Professor Bogdan Epureanu  
Assistant Professor Nikolaos I. Xiros, Florida Atlantic University

© Jonghun Lee

---

2010

To my family, for their invaluable love, support and encouragement

## **ACKNOWLEDGEMENTS**

I wish to express my gratitude to Professor Michael M. Bernitsas, the chairman of my dissertation committee, for suggesting this research topic and for his guidance and valuable suggestions throughout my graduate work. I also would like to express sincere appreciation to the members of my dissertation committee, Professor Armin W. Troesch, Professor Jing Sun, Professor Bogdan Epureanu and Professor Nikolaos Xiros for their suggestions and comments throughout the course of this research, especially during the final states.

I would like to thank the faculty, staff and colleagues of the Department of Naval Architecture and Marine Engineering for their much appreciated assistance. I wish to extend my warmest thanks to Dr. Hyun Chung, Dr. Taemin Earmme, Dr. Ajithkumar Raghavan, Dr. Kamaldev Raghavan, Mr. Daehyun Kim, Mr. Che-Chen Chang, Mr. Hongrae Park, Mr. Eunsoo Kim, Ms. Wei Wu and Ms. Ayoung Kim.

Finally, I wish to thank my parents and my wife Eunjung for their loving and continuous encouragement throughout my stay at the University of Michigan.

The financial support by (1) ONR grant N00014-08-1-0601 to the University of Michigan, Program Manager Kelly Copper, and (2) Michigan Universities Commercialization Initiative (MUCI) grant 06-1-P2-042DOC-133 to the University of Michigan, PI Andrew McColm of the Officer of Technology Transfer is gratefully acknowledged.

## TABLE OF CONTENTS

DEDICATION.....	ii
ACKNOWLEDGEMENTS.....	iii
LIST OF FIGURES.....	vii
LIST OF TABLES.....	xiii
ABSTRACT .....	xiv
CHAPTER 1. MARINE RENEWABLE ENERGY CONVERSION .....	1
1.1. Background.....	1
1.2. Literature Review .....	4
1.2.1. Ocean Energy Conversion.....	4
1.2.2. Vortex Induced Vibrations .....	6
1.2.3. VIVACE Converter .....	11
1.2.4. Virtual Damper/Spring System .....	15
1.3. Scope and Outline of This Dissertation.....	16
PART A: VIRTUAL VIVACE CONVERTER.....	18
CHAPTER 2. BUILDING A VIRTUAL DAMPER-SPRING SYSTEM....	18
2.1. Description of the VIVACE Apparatus.....	18
2.1.1. Old $V_{CK}$ VIVACE Apparatus .....	18
2.1.2. New $V_{CK}$ VIVACE Apparatus .....	21
2.2. Motor-Controller Systems for Virtual Damper-Spring System.....	23
2.3. Mathematical Modeling.....	26
2.4. Calibration of Motor Torque .....	30

CHAPTER 3. IDENTIFICATION OF INERTIAL MASS .....	34
3.1. Estimation of Inertial Mass.....	34
3.1.1. Estimation of Inertial Mass by Fourier Series Analysis.....	35
3.1.1.1. Solution Approach.....	35
3.1.1.2. Experimental Results and Analysis.....	40
3.1.2. Estimation of Inertial Mass by Free Decay Tests.....	43
3.1.2.1. Solution Approach.....	43
3.1.2.1. Experimental Results and Analysis.....	45
CHAPTER 4. IDENTIFICATION OF NONLINER STATIC DAMPING MODEL .....	47
4.1. Identification of Linear Viscous Damping + Kinetic Friction Model .....	47
4.2. Identification of 3 <sup>rd</sup> Order Polynomial Damping Model .....	55
4.2.1. 3 <sup>rd</sup> Order Polynomial Damping Model.....	55
4.2.1. Damping Model Identification .....	57
4.3. Identification of Nonlinear Viscous Damping + Kinetic Friction Model and Controller Design.....	63
4.3.1. Damping Model and Identification .....	63
4.3.2. Validation of Nonlinear Static Damping Model .....	67
4.3.3. Controller Design and Validation by VIV Experiments .....	75
4.3.3.1. Controller Design.....	75
4.3.3.1. Validation of the Designed Controller by VIV Experiments.....	75
CHAPTER 5. IDENTIFICATION OF NONLINEAR DYNAMIC DAMPING MODEL AND CONTROLLER DESIGN .....	78
5.1. Dynamic Damping Model Identification.....	78
5.1.1. Damping Force Calculation using $y$ and $dy/dt$ .....	78
5.1.2. Validation of Calculated $f$ .....	82
5.1.3. Autoregressive Friction Modeling in the Velocity Dead Zone .....	84
5.2. Controller Design and Verification .....	94
5.2.1. Validation of the Designed Controller by VIV Experiments.....	95
PART B: VIVACE POWER CURVE .....	97

CHAPTER 6. HIGH DAMPING VIV FOR POWER HARNESSING USING THE VIVACE CONVERTER .....	97
6.1. Experimental Facility.....	97
6.2. Experimental Results for High Damping VIV .....	98
6.2.1. Effect of Damping on VIV .....	99
6.2.1.1. Range of Synchronization .....	99
6.2.1.2. Amplitude of Oscillation .....	104
6.2.1.3. Frequency of Oscillation .....	106
6.2.2. Effect of Stiffness K on VIV .....	111
CHAPTER 7. OPTIMAL POWER HARNESSING.....	117
7.1. Mathematical Model of Harnessed Power and Dissipated Power .....	117
7.2. Harnessed Power Calculation using Experimental Results .....	119
7.3. Theoretical Power Limit of VCK VIVACE model .....	124
7.4. VIVACE Power Density.....	126
7.5. Optimal Power Envelop of the VCK VIVACE Model .....	128
CHAPTER 8. POWER DENSITY ASSESSMENT .....	132
CHAPTER 9. CONCLUSIONS AND RECOMMENDATIONS .....	138
9.1. Main Findings and Thesis Contributions.....	138
9.2. Recommendations for Future Research.....	141
APPENDIX A. VIVACE POWER CHARTS.....	142
REFERENCES .....	153

## LIST OF FIGURES

Figure 1-1. Amplitude of oscillation from experiments in air by Feng (1968) and experiments in water by Khalak and Williamson (1999) .....	9
Figure 1-2. The VIVACE Converter mounted on the channel .....	13
Figure 2-1. Lab scale model of the old $V_{CK}$ VIVACE apparatus .....	19
Figure 2-2. Lab scale model of the new $V_{CK}$ VIVACE apparatus .....	21
Figure 2-3. Motor controller system .....	23
Figure 2-4. Coordinate system of the $V_{CK}$ VIVACE model .....	26
Figure 2-5. Input vs. output voltage of DAC before calibration was conducted. ....	31
Figure 2-6. Schematic of the device for calibration test .....	32
Figure 2-7. Displacement vs. weight after torque-voltage calibration.....	33
Figure 3-1. Frequency response: forcing amplitude = 15N, forcing frequency = 0.8Hz. 35	
Figure 3-2. Frequency response: forcing amplitude = 40N, forcing frequency = 1.2Hz. 35	
Figure 3-3. Simulation model for the inertial mass estimation.....	38
Figure 3-4. Experimental Result: $A_{force} = 12N, \Omega = 1.5Hz$ .....	41
Figure 3-5. Experimental Result: $A_{force} = 14N, \Omega = 1.5Hz$ .....	41
Figure 3-6. Experimental Result: $A_{force} = 10N, \Omega = 1.6Hz$ .....	42
Figure 3-7. Experimental Result : $A_{force} = 10N, \Omega = 1.6Hz$ .....	42
Figure 3-8. Result of the free-decay test for the motor-pulley-belt system: $k = 1000 N/m$ , initial displacement = 0.2 m.....	45
Figure 4-1. Block diagram of identification method (Johnson and Lorenz 1992).....	48
Figure 4-2. Input profile and measured output in case 1 .....	50
Figure 4-3. Estimated viscous damping + Coulomb friction in case 1 .....	50
Figure 4-4. Input profile and measured output in case 2 .....	51



Figure 4-5. Estimated viscous damping + Coulomb friction in case 2.....	51
Figure 4-6. Input profile and measured output in case 3 .....	52
Figure 4-7. Estimated viscous damping + Coulomb friction in case3.....	52
Figure 4-8. $A/D : V_{CK}$ VIVACE model vs. VIVACE model with real springs when $k=883$ N/m .....	54
Figure 4-9. Force, velocity and their Fourier transform – Forcing Freq. = 1Hz, Forcing Amp. = 10N .....	55
Figure 4-10. FFT and time series of velocity from experiment and simulation - Forcing Freq. = 1.4Hz, Forcing Amp. = 10N.....	59
Figure 4-11. FFT and time series of velocity from experiment and simulation - Forcing Freq. = 1.6Hz, Forcing Amp. = 10N.....	60
Figure 4-12. FFT and time series of velocity from experiment and simulation - Forcing Freq. = 1.6Hz, Forcing Amp. = 14N.....	60
Figure 4-13. FFT and time series of velocity from experiment and simulation - Forcing Freq. = 1.2Hz, Forcing Amp. = 20N.....	61
Figure 4-14. FFT and time series of velocity from experiment and simulation - Forcing Freq. = 1.2Hz, Forcing Amp. = 25N.....	61
Figure 4-15. Force-velocity map – circles : experimental data. Solid line: nonlinear regression curve .....	64
Figure 4-16. Comparison between free decay test and simulation .....	66
Figure 4-17. Simulation model for validation of damping model .....	68
Figure 4-18. Comparison between experiment and simulation - forcing amplitude = 10N, forcing frequency = 0.5Hz .....	70
Figure 4-19. Comparison between experiment and simulation - forcing amplitude = 15N, forcing frequency = 0.5Hz .....	70
Figure 4-20. Comparison between experiment and simulation - forcing amplitude = 10N, forcing frequency = 0.6Hz .....	71
Figure 4-21. Comparison between experiment and simulation - forcing amplitude = 15N, forcing frequency = 0.6Hz .....	71
Figure 4-22. Comparison between experiment and simulation - forcing amplitude = 10N, forcing frequency = 0.7Hz .....	72
Figure 4-23. Comparison between experiment and simulation - forcing amplitude = 15N, forcing frequency = 0.7Hz .....	72

Figure 4-24. Comparison between experiment and simulation - forcing amplitude = 50N, forcing frequency = 1.2Hz .....	73
Figure 4-25. Comparison between experiment and simulation - forcing amplitude = 60N, forcing frequency = 1.1Hz .....	73
Figure 4-26. Comparison between experiment and simulation - forcing amplitude = 30N, forcing frequency = 0.8Hz .....	74
Figure 4-27. Comparison of $A/D$ with the VIVACE model with real springs to that with the $V_{CK}$ VIVACE model with NS damping model .....	77
Figure 5-1. Frequency response of $y$ and $\dot{y}$ for $A = 20N$ and $\Omega = 0.9$ Hz .....	79
Figure 5-2. Comparison between filtered and unfiltered $\dot{y}$ for $A = 20N$ and $\Omega = 0.9$ Hz .....	80
Figure 5-3. Comparison of displacement, damping force and frequency response between simulation and experimental results for $A = 20N$ and $\Omega = 0.9$ Hz .....	82
Figure 5-4. Comparison of displacement, damping force and frequency response between simulation and experimental results for $A = 70N$ and $\Omega = 0.9$ Hz .....	83
Figure 5-5. Comparison of displacement, damping force and frequency response between simulation and experimental results for $A = 90N$ and $\Omega = 0.9$ Hz .....	83
Figure 5-6. $f$ vs. $y$ for $A = 15N$ and $\Omega = 1$ Hz .....	84
Figure 5-7. Comparison of normalized $f$ with the output of AR model .....	90
Figure 5-8. Comparison of NS and LARNOS model with experimental result for $A = 15N$ and $\Omega = 1.0$ Hz .....	92
Figure 5-9. Comparison of NS and LARNOS model with experimental result for $A = 120N$ and $\Omega = 0.8$ Hz .....	93
Figure 5-10. Comparison of $A/D$ with VIVACE model with real springs to that with $V_{CK}$ VIVACE model .....	96
Figure 6-1. $A/D$ vs. $U^*$ , $U$ and $Re$ for $k_{virtual} = 400N/m$ and various values of $\zeta h_{arn}$ .....	100
Figure 6-2. $A/D$ vs. $U^*$ , $U$ and $Re$ for $k_{virtual} = 600N/m$ and various values of $\zeta h_{arn}$ .....	100
Figure 6-3. $A/D$ vs. $U^*$ , $U$ and $Re$ for $k_{virtual} = 800N/m$ and various values of $\zeta h_{arn}$ .....	101
Figure 6-4. $A/D$ vs. $U^*$ , $U$ and $Re$ for $k_{virtual} = 1000N/m$ and various values of $\zeta h_{arn}$ .....	101

Figure 6-5. $A/D$ vs. $U^*, U$ and $Re$ for $k_{virtual} = 1200\text{N/m}$ and various values of $\zeta_{harn}$ .....	102
Figure 6-6. $A/D$ vs. $U^*, U$ and $Re$ for $k_{virtual} = 1400\text{N/m}$ and various values of $\zeta_{harn}$ .....	102
Figure 6-7. $A/D$ vs. $U^*, U$ and $Re$ for $k_{virtual} = 1600\text{N/m}$ and various values of $\zeta_{harn}$ .....	103
Figure 6-8. $A/D$ vs. $U^*, U$ and $Re$ for $k_{virtual} = 1800\text{N/m}$ and various values of $\zeta_{harn}$ .....	103
Figure 6-9. $f_{osc}/f_{n,water}$ vs. $U^*, U$ and $Re$ when $k_{virtual} = 400\text{N/m}$ for various values of $\zeta_{harn}$ .....	107
Figure 6-10. $f_{osc}/f_{n,water}$ vs. $U^*, U$ and $Re$ when $k_{virtual} = 600\text{N/m}$ for various values of $\zeta_{harn}$ .....	107
Figure 6-11. $f_{osc}/f_{n,water}$ vs. $U^*, U$ and $Re$ when $k_{virtual} = 800\text{N/m}$ for various values of $\zeta_{harn}$ .....	108
Figure 6-12. $f_{osc}/f_{n,water}$ vs. $U^*, U$ and $Re$ when $k_{virtual} = 1000\text{N/m}$ for various values of $\zeta_{harn}$ .....	108
Figure 6-13. $f_{osc}/f_{n,water}$ vs. $U^*, U$ and $Re$ when $k_{virtual} = 1200\text{N/m}$ for various values of $\zeta_{harn}$ .....	109
Figure 6-14. $f_{osc}/f_{n,water}$ vs. $U^*, U$ and $Re$ when $k_{virtual} = 1400\text{N/m}$ for various values of $\zeta_{harn}$ .....	109
Figure 6-15. $f_{osc}/f_{n,water}$ vs. $U^*, U$ and $Re$ when $k_{virtual} = 1600\text{N/m}$ for various values of $\zeta_{harn}$ .....	110
Figure 6-16. $f_{osc}/f_{n,water}$ vs. $U^*, U$ and $Re$ when $k_{virtual} = 1800\text{N/m}$ for various values of $\zeta_{harn}$ .....	110
Figure 6-17. Amplitude ratios for $\zeta_{harn} = 0$ for various values of $k_{virtual}$ .....	113
Figure 6-18. Amplitude ratios for $\zeta_{harn} = 0.04$ for various values of $k_{virtual}$ .....	113
Figure 6-19. Amplitude ratios for $\zeta_{harn} = 0.08$ for various values of $k_{virtual}$ .....	114
Figure 6-20. Amplitude ratios for $\zeta_{harn} = 0.12$ for various values of $k_{virtual}$ .....	114
Figure 6-21. Amplitude ratios for $\zeta_{harn} = 0.16$ for various values of $k_{virtual}$ .....	115
Figure 6-22. Drag and lift coefficients for a stationary circular cylinder (Zdravkovich 1990). .....	115
Figure 7-1. 30 cycle-averaged $Pharn$ for $k_{virtual} = 400\text{ N/m}$ .....	120

Figure 7-2. 30 cycle-averaged $Ph_{arn}$ for $k_{virtual} = 600$ N/m.....	120
Figure 7-3. 30 cycle-averaged $Ph_{arn}$ for $k_{virtual} = 800$ N/m.....	121
Figure 7-4. 30 cycle-averaged $Ph_{arn}$ for $k_{virtual} = 1000$ N/m.....	121
Figure 7-5. 30 cycle-averaged $Ph_{arn}$ for $k_{virtual} = 1200$ N/m.....	122
Figure 7-6. 30 cycle-averaged $Ph_{arn}$ for $k_{virtual} = 1400$ N/m.....	122
Figure 7-7. 30 cycle-averaged $Ph_{arn}$ for $k_{virtual} = 1600$ N/m.....	123
Figure 7-8. 30 cycle-averaged $Ph_{arn}$ for $k_{virtual} = 1800$ N/m.....	123
Figure 7-9. Configuration of cylinder deployment of the VIVACE Converter.....	126
Figure 7-10. Optimal Power Envelop and Corresponding Dissipated Power .....	128
Figure 7-11. Power chart for $U=1.04$ m/s.....	129
Figure A-1. Power chart for $U=0.41$ m/s.....	142
Figure A-2. Power chart for $U=0.44$ m/s.....	143
Figure A-3. Power chart for $U=0.48$ m/s.....	143
Figure A-4. Power chart for $U=0.52$ m/s.....	144
Figure A-5. Power chart for $U=0.55$ m/s.....	144
Figure A-6. Power chart for $U=0.59$ m/s.....	145
Figure A-7. Power chart for $U=0.63$ m/s.....	145
Figure A-8. Power chart for $U=0.67$ m/s.....	146
Figure A-9. Power chart for $U=0.7$ m/s.....	146
Figure A-10. Power chart for $U=0.74$ m/s.....	147
Figure A-11. Power chart for $U=0.78$ m/s.....	147
Figure A-12. Power chart for $U=0.81$ m/s.....	148
Figure A-13. Power chart for $U=0.85$ m/s.....	148
Figure A-14. Power chart for $U=0.89$ m/s.....	149
Figure A-15. Power chart for $U=0.92$ m/s.....	149
Figure A-16. Power chart for $U=0.96$ m/s.....	150
Figure A-17. Power chart for $U=1$ m/s.....	150

Figure A-18. Power chart for $U=1.04$ m/s .....	151
Figure A-19. Power chart for $U=1.07$ m/s .....	151
Figure A-20. Power chart for $U=1.11$ m/s .....	152

## LIST OF TABLES

Table 2-1. Components of the old $V_{CK}$ VIVACE model.....	19
Table 2-2. Components of the $V_{CK}$ VIVACE model.....	22
Table 2-3. Descriptions of the motor-controller system.....	24
Table 2-4. Particulars of the motor.....	24
Table 2-5. Description of components of the $V_{CK}$ VIVACE model.....	27
Table 3-1. Simulation parameters.....	38
Table 3-2. Estimated mass and error for different Coulomb friction cases.....	39
Table 3-3. Experimental conditions and estimated mass.....	40
Table 3-4. Results of free-decay tests.....	46
Table 4-1. Input profile particulars.....	49
Table 4-2. System identification results.....	53
Table 4-3. Input force particulars.....	57
Table 4-4. Estimated coefficients.....	59
Table 4-5. Estimation errors of Eq. (4-8).....	65
Table 4-6. Input force particulars.....	67
Table 4-7 Comparison between experiment and simulation.....	69
Table 4-8. Results of free decay tests to identify real spring constants $k$ .....	76
Table 5-1. Estimated elements of $aOPT$ in LAR model.....	90
Table 5-2. Roots of the $pC(z - 1)$ of LAR term.....	91
Table 6-1. Maximum amplitude ratio for each combination of $k_{virtual}$ and $\zeta_{harn}$ ...	105
Table 7-1. Power generated by the VIVACE Converter.....	131

## ABSTRACT

An apparatus,  $V_{CK}$ , is designed and built to replace the physical damper and springs of the VIVACE (Vortex Induced Vibrations for Aquatic Clean Energy) Converter with a motor-controller system. VIVACE harnesses hydrokinetic energy of water currents by converting it to mechanical energy using VIV. Next, it converts the mechanical energy of cylinders in VIV into electricity.  $V_{CK}$  enables conducting high number of model tests quickly as damping and springs are set by software rather than hardware. The controller provides a damper-force and spring-force feedback based on displacement and velocity measurements, thus, introducing no additional artificial force-displacement phase lag, which would bias energy conversion. The damping of even such a simple spring-damper-mass system is strongly nonlinear, even in air, particularly away from the system's natural frequency and strongly affects modeling near the ends of the VIV synchronization range. System identification in air reveals nonlinear viscous damping, static friction, and kinetic friction. Hysteresis, which occurs in the zero velocity limit, is successfully modeled by a proposed nonlinear dynamic damping model LARNOS (Linear Autoregression combined with Nonlinear Static model).

To obtain the optimal VIVACE power at a given current speed, extensive VIV tests are performed with the  $V_{CK}$  VIVACE apparatus for Reynolds number  $40,000 < Re < 120,000$  and damping  $0 < \zeta < 0.16$  in the Low Turbulence Free Surface Water Channel of the Marine Renewable Energy Laboratory at the University of Michigan. Scarce VIV data exist in

that parametric subspace of  $Re$  and  $\zeta$ . From the VIV tests, the optimal damping for energy harnessing is found for velocity  $0.41\text{m/s} < U < 1.11\text{m/s}$  using spring stiffness  $400\text{N/m} < k < 1800\text{N/m}$ . Thus, the VIVACE converter power envelope is developed. The following experimental observations are made: (1) In the high-lift TrSL3 and TrBL0 flow regimes, high-amplitude, high-damping VIV is maintained. (2) VIV strongly depends on Reynolds. (3) The amplitude ratio ( $A/D$ ) increases with Reynolds number within the upper branch of the VIV synchronization range. (4) In TrSL3/TrBL0,  $A/D$  of 1.78 was achieved for a smooth cylinder routinely in low damping. (5) Power density of  $98.2\text{W/m}^3$  at 2 knots is achieved including space between cylinders. This exceeds previous measurements by a factor of five.



# **CHAPTER 1.**

## **MARINE RENEWABLE ENERGY CONVERSION**

### **1.1. Background**

Energy is essential for the day-to-day activities of human life. The progress that humans being made in the past and also at present is so much integral with the production and consumption of energy that one apparently becomes the synonym of the other. Since the non-renewable energies such as coal, oil, nuclear energy and natural gas are fast depleting, it is mandatory for human existence to search for other types of energy freely available in nature, i.e., renewable energy. Among various forms of renewable energy, ocean energy, wind energy and solar energy bear at most importance. Ocean energy manifests in five forms basically: as waves, currents, tides, thermal gradient and salinity gradient and this provides non-pollutant (clean) and renewable energy (Schiller and Linke 1933; Pontes and Falcao 2001). Literature reports several studies revealing the availability of ocean energy (Cavanagh et al. 1993; WEC 2001); tidal energy potential is estimated to be 79 EJ, wave energy potential is estimated to be 65 EJ, ocean thermal energy is estimated to be 7200 EJ, and lastly salt gradient energy is estimated to be 83 EJ (WEC 2001). However, ocean / tidal power has been under utilized owing to higher installation and maintenance cost and also, due to less advanced research and

development. (Cavanagh et al. 1993). Needless to say, there are challenges which have to be surmounted to generate electricity from Ocean power. The VIVACE (Vortex-Induced Vibration Aquatic Clean Energy) Converter invented by Bernitsas and Raghavan in 2005 at University of Michigan, Ann Arbor deserves much credit in the present scenario where the world is getting closer to an 'Energy Crisis'. The VIVACE Converter utilizes the phenomenon of Vortex-Induced Vibrations (VIV) to convert the fluid power to electricity and has been patented by Bernitsas & Raghavan (Bernitsas and Raghavan 2005a; Bernitsas and Raghavan 2005b). It is to be emphasized that, VIV is generally known to be a potentially disastrous phenomenon to structures world-wide. But, the VIVACE Converter successfully utilizes VIV to generate power from flow currents.

Even though the foundation of research idea to generate power using the VIVACE Converter was laid down by Bernitsas & Raghavan (Bernitsas et al. 2008), the system initially built by them basically comprises of a spring-cylinder system. Due to the hardware limitations, harnessed power is optimized only in a limited range of spring stiffness and damping ratio. In an attempt to overcome this lacuna, a virtual damper/spring ( $V_{CK}$ ) system has been developed wherein the action of springs and damping forces are replaced with equivalent force produced by a motor. Thus, in the new  $V_{CK}$  system, the system could be run for an extensive range of equivalent spring stiffness and damping values to produce power which was not possible with the previous mechanical system built by Bernitsas & Raghavan (Bernitsas et al. 2008; Bernitsas et al. 2009). Apart from this distinct advantage the hardships encountered in changing the mechanical springs in order to vary the spring stiffness has also been completely

eliminated in the present  $V_{CK}$  system and thus, the system is made very simple and convenient to operate.

## 1.2. Literature Review

In this Section, a comprehensive review of the literature on the following areas is presented: Ocean Energy Conversion, Vortex-Induced Vibrations, VIVACE Converter and  $V_{CK}$  system. On the first two areas, only a limited review is presented since they form only a forerunner to the actual scope of this thesis, namely, development of the  $V_{CK}$  VIVACE system.

### 1.2.1. Ocean Energy Conversion

For licensed operation in USA, an Energy Conversion Device should meet some essential technical requirements laid down by the Department of Energy (DOE) and the California Energy Commission (CEC). They are (1) High energy density (2) Non-obtrusiveness (3) Low maintenance (4) Robustness (5) Compatibility with marine life (6) Meeting life cycle cost targets (7) Low dependence on ocean conditions (8) Have a minimum life of 10-20 years.

Serious efforts have been expended to satisfy the aforementioned requirements worldwide particularly in Europe and Japan and to a lesser extent in USA (Thorpe 1998; Pontes and Falcao 2001; WaveNet 2003). Numerous devices have been invented (patented) and several pilot devices have been launched (Technomare 1996; Pontes and Falcao 2001). In spite of all these efforts, a globally acceptable converter has not been developed (Thorpe 1998; WaveNet 2003).

As already mentioned in Section 1.1, ocean energy basically manifests in five forms: waves, currents, tides, thermal gradient and salinity gradient. However, Energy

Converters designed based on these sources could not meet some of the standards/requirements set by CEC/DOE as shown in the following paragraphs.

- (1) Converters based on Wind or tidal current energy (Watermills/turbines) can extract energy proportionally to their projected surface at efficiency of 15-30% (Website: Marine Turbines ; Technomare 1996). They function efficiently only for flow velocities greater than 2m/sec (~4 knots) (Website: Marine Turbines).
- (2) Converters based on surface oscillation, such as water column, buoy, flap, or pendulum (Pontes and Falcao 2001; WaveNet 2003; WMCE 2003) have high energy output only in a very narrow band of wave frequencies near resonance.
- (3) Tidal energy converters are usually very large and are as obtrusive as water dams and require at least a 5m head to operate. They also require a 5-7 year construction period and significant initial capital cost (Website: Marine Turbines).
- (4) Majority of other Converters operate on the surface occupying valuable coastal areas.
- (5) Unlike converters such as Watermills, Turbines or Tidal dams, the VIVACE Converter is less disturbing to marine life.

### 1.2.2. Vortex Induced Vibrations

The VIVACE Converter is basically a device operating based on the phenomenon of Flow-Induced Vibrations (FIV), particularly Vortex-Induced Vibrations (VIV) of circular cylinder. Hence, this topic, namely, VIV deserves a focused, brief review of the pertinent literature complementing the major scope of this thesis.

The literature on Vortex-Induced Vibrations of circular cylinder is very extensive covering both experimental and numerical methods of investigation. A VIVACE Converter modulo consists of an elastically mounted circular cylinder in its simplest form. Basically, circular cylinder undergoes VIV when it is subjected to a fluid flow. Hence, the free vibration of the cylinder is what is available to harness energy in the VIVACE Converter. In this context, literature pertains to both free and forced vibration studies are relevant to be discussed in this section. Many relevant studies were reported in the literature pertinent to VIV of circular cylinders (Bishop and Hassan 1964; Feng 1968; Gowda and Deshkulkarni 1988; Khalak and Williamson 1999; Govardhan 2000; Williamson and Govardhan 2004; Huera-Huarte and Bearman 2009). In the VIVACE Converter, basically cross-stream oscillations form the primary response mode of the cylinder. The response magnitude in the in-line direction is usually an order of magnitude lesser than that in the transverse direction. For cross-stream response, as the flow velocity increases, the vortex-shedding frequency ( $f_v$ ) the natural system frequency ( $f_{n,water}$ ) come closer and collapse in to a single frequency (close to the natural system frequency). This phenomenon is known by various names: lock-in, synchronization, wake capture, hydro-elastic or fluid-elastic oscillations or self-excited oscillations etc. (Sarpkaya 1979). In such a case, the interaction between the oscillating body and the action of fluid is non-

linear (Bishop and Hassan 1964). It is interesting and surprising to note is that during synchronization, the body oscillation frequency ( $f_{osc}$ ) and vortex-shedding frequency ( $f_v$ ) lock together encompassing a broad range of reduced velocity  $U^*$  which is defined as

$$U^* = U/(f_{n,water}D)$$

Another important parameter which influences the cylinder oscillation is the mass ratio,  $m^*$ .  $m^*$  is defined as  $m_{osc}/m_d$  where  $m_{osc}$  is the total oscillating mass of the cylinder (undergoing VIV including all the oscillating accessories and also 1/3<sup>rd</sup> of the spring mass) and  $m_d$  is the displaced fluid mass.  $m_d = (\rho_w \pi D^2 L/4)$ ;  $D$  is the cylinder diameter,  $L$  is the length of the cylinder and  $\rho_w$  is the density of water. Apart from  $m^*$ , the total system damping ( $\zeta$ ) plays an important role in VIV. According to Khalak and Williamson (1999), the range of synchronization is mainly controlled by  $m^*$  (when  $m^*\zeta$  is a constant) and the peak amplitude is controlled primarily by  $m^*\zeta$  in the range  $35000 \leq Re \leq 10000$ . It is to be mentioned that the VIVACE Converter is needed to be operated in high damping conditions for energy harnessing and hence, the effect of damping on the cylinder response and thus on the overall performance of the machine is critical.

As mentioned earlier, in lock-in condition, in the conventional sense,  $f_n \sim f_{osc}$  for VIV systems operating in air (Feng 1968). But, for systems with low mass ratios (such as in water), the body oscillation frequency could be distinctly different (higher) from the system natural frequency (Govardhan and Williamson 2002). This deviation of  $f_{osc}$  from  $f_{n,water}$  is brought about by virtue of ‘added mass’,  $m_a$  (Sarpkaya 1979; Sarpkaya 2004).

For a circular cylinder,  $m_a$  is given by the product of  $C_a$  and  $m_d$ ;  $C_a = 1.0$  (potential added mass coefficient) for a circular cylinder (Sarpkaya 2004).

One of the most important aspects in VIV is the amplitude of cylinder oscillation  $A/D$ .  $A/D$  appears to be very much dependent on the value of  $m^*$ . Feng (1968) has observed only two amplitude branches (the initial and the lower) in the response characteristics of a flexibly mounted circular cylinder in air ( $m^* \sim 250$ ). However, Khalak and Williamson (1999) has observed three amplitude branches (initial, upper and lower) and a larger peak amplitude with broader synchronization range for a flexibly mounted circular in water ( $m^* \sim 2.4$ ). Figure 1-1 shows the data of Feng (1968) and Khalak & Williamson (1999).  $A/D$  is closely linked to the near-wake structure (mainly, the vortex-shedding mode) of the cylinder (Williamson and Roshko 1988; Govardhan and Williamson 1999; Morse and Williamson 2009); shedding modes such as 2S, 2P, P+S, 2T and 2F have been reported in the literature. Most of the previous studies report amplitude values up to 1.13 diameters (Williamson and Govardhan 2004). But, the studies conducted at much higher Reynolds numbers (TrSL3 regime according to the classification of flow by Zdravkovich (1990); TrSL3 regime is a high-lift regime) and have yielded much higher amplitudes of oscillation (Raghavan et al. 2007; Bernitsas et al. 2009).



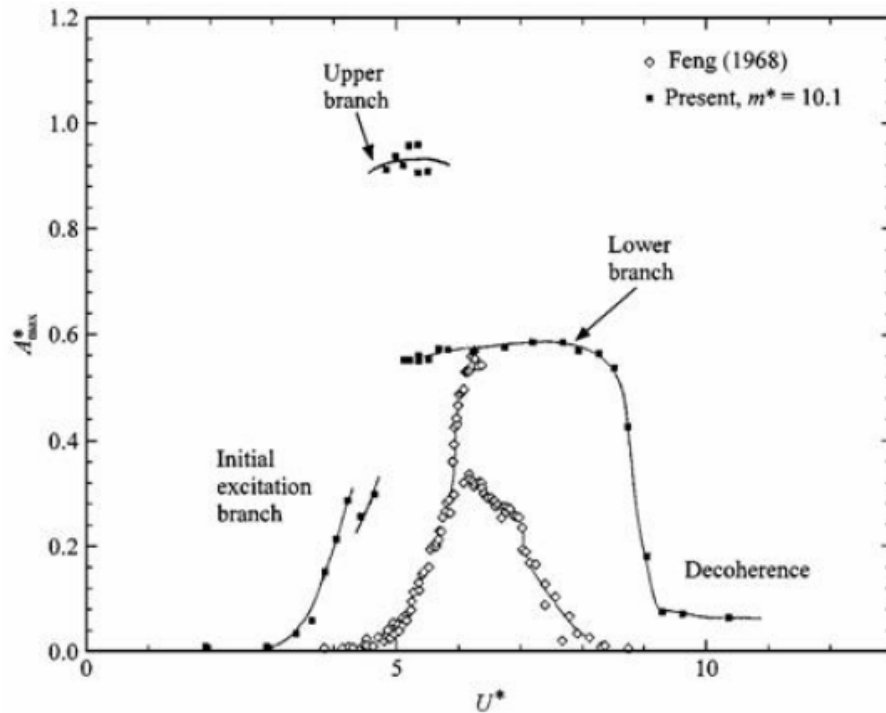


Figure 1-1. Amplitude of oscillation from experiments in air by Feng (1968) and experiments in water by Khalak and Williamson (1999)

Studies of Szepessy & Bearman (1992) and Norberg (1994) indicate that aspect ratio ( $L/D$ ) is an important response-governing parameter for a circular cylinder. Hence,  $L/D$  is carefully selected ( $L/D \sim 20$ ) for the VIVACE Converter as it primarily affects the correlation length of the vortex shedding along the cylinder span.

Previous studies reveal that proximity of cylinder to the free surface induces changes in the flow structure around the cylinder and thereby modifies its vibratory response (Sheridan et al. 1995; Carberry 2002; Bernitsas et al. 2007a). Similarly, bottom boundary also significantly influences the near-wake flow and induced oscillations of the cylinder (Price et al. 2002; Raghavan et al. 2007b). But, the VIVACE Converter is designed to

operate completely submerged and neither not too close to the free surface nor to the bottom surface yielding the best possible performance.

### 1.2.3. VIVACE Converter

The phenomenon of Vortex-Induced Vibration (VIV) is known since 1878. But, till recently, no attempts were made to harness energy from this ‘potentially catastrophic’ phenomenon. In 2006, Bernitsas & Raghavan have built the device, ‘VIVACE Converter’ which utilizes VIV to produce power. Previous works (Clark 1999; Yoshitake et al. 2004) in this direction had not yielded satisfactory results.

The VIVACE Converter is designed based on the simple idea of enhancing vortex shedding rather than spoiling it and maximizing VIV under high damping conditions rather than suppressing it. The VIVACE Converter consists of a bluff body (such as a circular cylinder) which is flexibly mounted (such as on springs) and subjected to a fluid flow. The body thus undergoes vortex-induced, self-excited oscillations giving out a visible mechanical energy output. This mechanical energy is converted to electrical energy through a generator. In the case of presented study, circular cylinder (mounted on elastic springs) is used as the bluff body. The VIVACE Converter is scalable and can extract energy from flow currents with velocities ranging from 0.5knots to 5knots (Bernitsas and Raghavan 2005b; Bernitsas and Raghavan 2005a). It is very robust being not easily affected by the environmental conditions because the lock-in or synchronization between the oscillating body and the wake occurs over a broad range of Reynolds number.

The VIVACE Converter works on the following basic principles (Bernitsas et al. 2008):

(a) *Vortex-induced vibrations of a rigid circular cylinder mounted on linear springs:*

The phenomenon of VIV has been extensively studied and investigated for the

past 100 years. Bluff bodies exposed to a fluid flow give rise to vortex shedding on its either side generating oscillatory lift leading to cross-flow vibrations. Since long, this phenomenon is known to be disastrous to structures and all efforts were to spoil vortex-shedding and the consequent VIV. However, the VIVACE Converter exploits these vibrations by generating useful power.

- (b) *Non-linear resonance*: As mentioned earlier, during VIV, the oscillating body frequency locks on to the vortex shedding frequency over a broad range of Reynolds number. Here, the body oscillations control the shedding process and thus the vortices are shed at about the natural frequency of the system in apparent violation of the Strouhal relationship. Hence, when compared to other Ocean Energy Converters (such as buoys, water columns etc.) working on the principle of linear resonance, the VIVACE Converter has more productive operating range for power generation.
- (c) *Correlation length*: In Vortex-Induced Vibrations, correlation length is defined as the body span over which the vortex shedding is occurring nearly in phase. Higher the correlation length, higher is the induced force. Usually, an aspect ratio ( $L/D$ ) of 7 to 20 is employed for a circular cylinder undergoing VIV. The VIVACE Converter is designed with an aspect ratio in this range.
- (d) *Electricity generation*: In VIVACE Models I, II and III, a belt and gear system transmits the mechanical energy to a generator to convert it to electrical energy. Important aspect in energy conversion is the system damping. Too high damping will suppress VIV, whereas too little damping will end up in negligible energy harnessing.

A picture of the VIVACE Converter mounted on the channel is shown in Figure 1-2.



Figure 1-2. The VIVACE Converter mounted on the channel

The elements of this module are as follows: a circular rigid cylinder of diameter  $D$  and length  $L$ , two supporting linear springs, one or more generators, and a gear box for transmission of harnessed power. The cylinder is placed perpendicular to the flow direction. The cylinder oscillates under VIV in transverse direction of the flow. Most of the information available on circular cylinder is either on the induced oscillations at low Reynolds number and low damping (Gopalkrishnan 1993; Jauvtis and Williamson 2003; Klamo et al. 2005) or on field tests at high Reynolds numbers but with suppression devices attached to the cylinder (Blevins 1990; Sumer and Fredsøe 1997). Whereas for

the VIVACE Converter, specific data at high Reynolds number and high damping is required which are scarce in the present literature. Hence, tests were to be conducted for VIVACE Models I, II and III in the Low Turbulence Free Surface Water (LTFSW) Channel of the University of Michigan (UoM) and results were reported (Bernitsas et al. 2008; Bernitsas et al. 2009).

#### 1.2.4. Virtual Damper/Spring System

Hover et al. built and upgraded the Virtual Cable Testing Apparatus (VCTA) which combines force-feedback control with on-line numerical simulation of a modeled-structure (Hover et al. 1997; Hover et al. 1998). Even though VCTA is the first VIV testing apparatus which enables to replace physical mass, damper and spring with virtual ones, it causes an artificial additional phase lag of 12 deg (Hover et al. 1997) and 5 deg (Hover et al. 1998) respectively to the cylinder with respect to the actual oscillating cylinder in VIV with real springs. This phase lag is due to filtering of noisy measured fluid force signal which is fundamentally inevitable for the cylinder position control in the nonyielding water environment. The induced artificial phase lag would bias energy conversion (Bernitsas et al. 2008). Whereas,  $V_{CK}$  that will be designed and built in this dissertation, provides damper-spring force based on displacement and velocity feedback, thus introducing no additional artificial phase lag. In order to design a controller for the  $V_{CK}$  VIVACE model, proper damping model selection and accurate system identification should be performed in advance. Digital controller design and system identification have been discussed in many books and papers (Karnopp 1985; Kubo et al. 1986; Johnson and Lorenz 1992; Ogata 1995; Franklin et al. 1998; Xiros 2002).

### 1.3. Scope and Outline of This Dissertation

This dissertation consists of two parts, PART A and B.

In PART A,  $V_{CK}$  system is designed and built to replace the physical damper and springs of the VIVACE Converter with virtual elements. PART A has four chapters, CHAPTER 2 to CHAPTER 5 and is organized as follows:

- CHAPTER 2: Describes the  $V_{CK}$  VIVACE model and also the pertinent mathematical modeling.
- CHAPTER 3: Describes the method of estimation of inertial mass of the  $V_{CK}$  VIVACE model.
- CHAPTER 4: Describes three non-linear static damping models proposed and identified for the  $V_{CK}$  VIVACE.
- CHAPTER 5: Describes neural network damping model which considers non-linear memory effect of velocity, is proposed and identified. Also, a controller which works on the identified neural network damping model, is designed and verified.

In PART B, the effects of design parameters such as  $k$ ,  $\zeta$  and  $Re$  are studied through extensive and systematic VIV experiments performed with the  $V_{CK}$  VIVACE model. The optimal harnessed power is also calculated at a given design current speed. PART B is organized as follows:

- CHAPTER 6: Presents the study of the effect of  $k$  and  $\zeta$  on range of synchronization, amplitude of oscillation and frequency of oscillation.



- CHAPTER 7: Presents the study on harnessed power calculation using experimental results. Also, optimal power envelop is developed for the velocity range  $0.41\text{m/s} < U < 1.11\text{m/s}$ .
- CHAPTER 8: Presents the assessment of the VIVACE power density. The power density of the VIVACE Converter is compared with that of wind turbines and Diesel engines.
- CHAPTER 9: Contains some concluding remarks and suggestions for future work.

## **PART A: VIRTUAL VIVACE CONVERTER**

### **CHAPTER 2.**

## **BUILDING A VIRTUAL DAMPER-SPRING SYSTEM**

### **2.1. Description of the VIVACE Apparatus**

#### **2.1.1. Old $V_{CK}$ VIVACE Apparatus**

Figure 2-1 shows a SolidWorks drawing of the lab scale model of the  $V_{CK}$  VIVACE that was used previously. The motor generates virtual spring torque and damping torque using the angle and angular velocity measurements while the hydrodynamic force is exerted on the cylinder. The rotational motion of the motor is converted to a linear motion by the timing-belt which encircles the two pulleys. The moving part consisting of the cylinder and its support strut is connected to the timing-belt and oscillates along the shafts driven by the motor. Components of the  $V_{CK}$  VIVACE model are listed in Table 2-1.

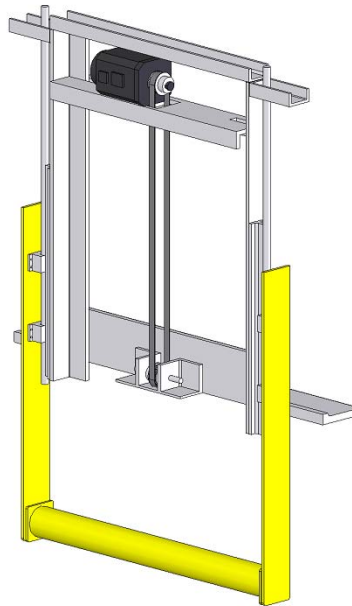


Figure 2-1. Lab scale model of the old  $V_{CK}$  VIVACE apparatus

Table 2-1. Components of the old  $V_{CK}$  VIVACE model

Cylinder diameter $D$ [in, cm]	3.5/8.99
Cylinder length $L$ [in, cm]	36/91.44
Mass of the oscillating components [kg]	9.81
Pulley radius [cm]	5.6

One problem observed with the old version of the  $V_{CK}$  VIVACE model was vibration of timing-belt due to the tension difference of the time-belt in upper and lower sides of the place where oscillating part is connected. Also, it does not have any safety measure when

excessive disturbance torque is applied to the motor. These problems motivated the design of a new version of the  $V_{CK}$  VIVACE model.

### 2.1.2. New $V_{CK}$ VIVACE Apparatus

In order to address the problems mentioned above, a new  $V_{CK}$  VIVACE apparatus is designed. Figure 2-2 shows a SolidWorks drawing of the new  $V_{CK}$  VIVACE apparatus. Also, the particulars of the  $V_{CK}$  VIVACE model are listed in Table 2-2.

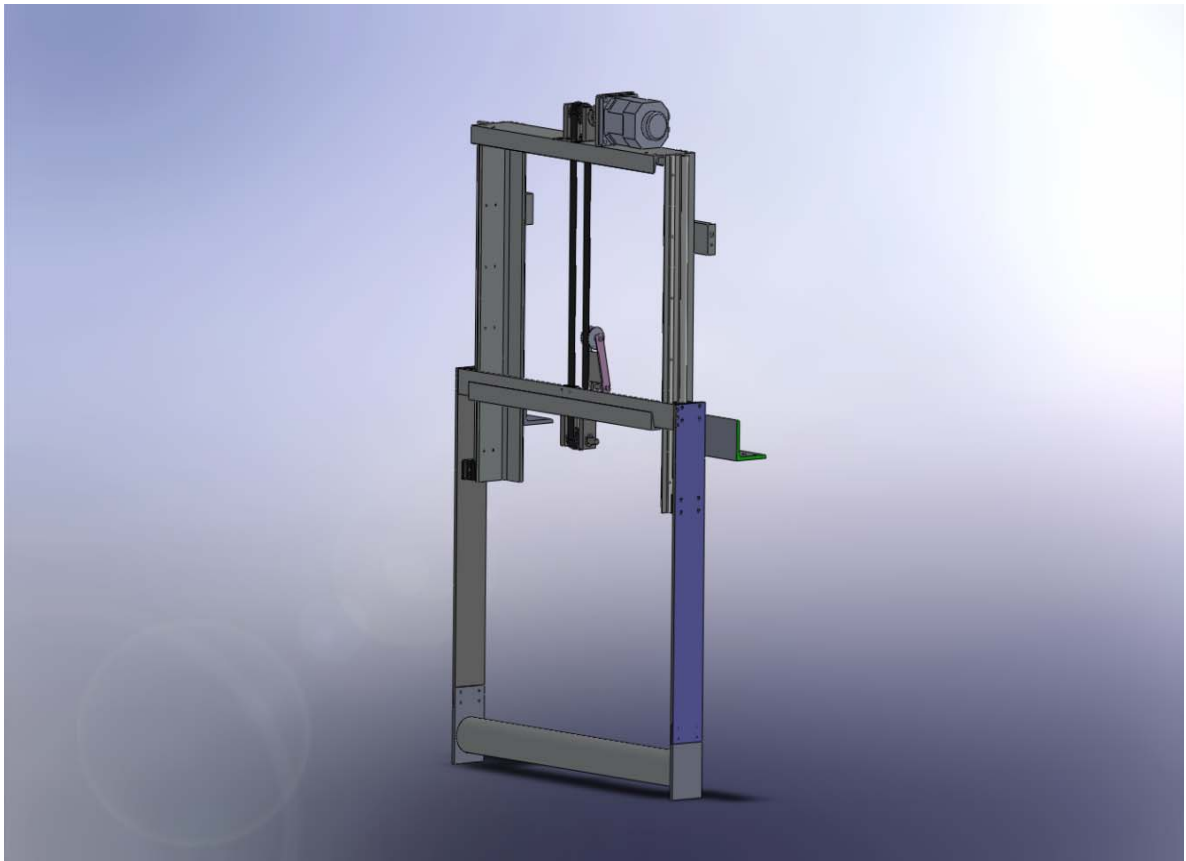


Figure 2-2. Lab scale model of the new  $V_{CK}$  VIVACE apparatus

Table 2-2. Components of the  $V_{CK}$  VIVACE model

Cylinder diameter $D$ [in, cm]	3.5/8.99
Cylinder length $L$ [in, cm]	36/91.44
Mass of oscillating components [kg]	8.88
Pulley radius [cm]	4.9

The basic working mechanism of the  $V_{CK}$  VIVACE apparatus is the same as that of the old  $V_{CK}$  VIVACE. Improvement on the vibration of the timing-belt is made by using an idler. The idler gives force at the timing-belt in longitudinal direction to reduce vibration. Also, a coupling is used between the upper pulley and motor shaft. When excessive torque is applied, it slips to protect the motor. As shown in Table 2-2, mass of oscillating part is reduced by 0.93 kg. The size of pulley is a little bit smaller than that of the old  $V_{CK}$  VIVACE apparatus. Also, it will turn out in the later section that damping of the system is reduced, which is beneficial for harnessing more hydrokinetic energy.

## 2.2. Motor-Controller Systems for Virtual Damper-Spring System

Figure 2-3 shows a digital controller-motor system. Details of four labeled components are listed in Table 2-3.

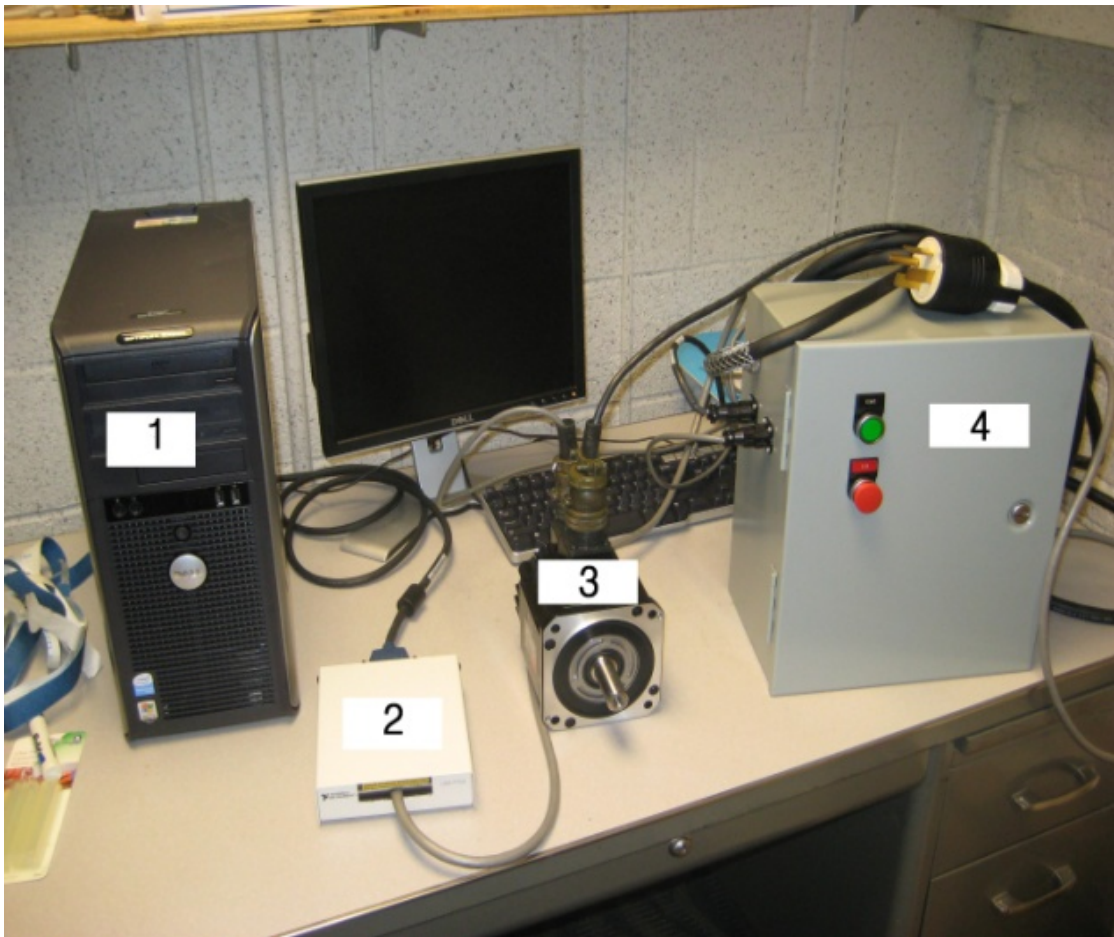


Figure 2-3. Motor controller system

Table 2-3. Descriptions of the motor-controller system

Part no.	Description
1	Controller board embedded in a computer (National Instruments: NI-7340)
2	Universal Motion Interface (National Instruments: UMI-7764)
3	Motor+embedded encorder (Sanyo Denki: P60B13150HXS00M)
4	Servo drive (Sanyo Denki: QS1A05AA)

The  $V_{CK}$  VIVACE model is powered by the 200 VAC 3-phase servo motor listed in Table 2-3. Particulars of the motor are presented in Table 2-4.

Table 2-4. Particulars of the motor

Rotor inertia [ $\text{kg}\cdot\text{m}^2$ ]	$8.28 \times 10^{-4}$
Rated torque [Nm]	7.5
Max. stall torque [Nm]	20

The embedded encoder inside the motor is a quadrature type optical encoder. It provides angle and angular velocity of the motor which are used for feedback control. In this application, one revolution of the motor corresponds to 2000 encoder counts. Communication and control are achieved by means of NI-7340 connected to a Microsoft Windows based PC. Controllers are programmed using LabView and loaded on the NI-



7340 for closed-loop operation. In this application, NI-7340 samples data at every 5 msec. The servo drive QS1A05AA is connected to the controller board through Universal Motion Interface UMI-7764. The servo drive operates in torque-command mode and receives a command signal from the controller, amplifies the signal, and transmits electric current to a servo motor in order to produce motion proportional to the command signal.

### 2.3. Mathematical Modeling

A SolidWorks drawing for the physical modeling of the VIVACE with  $V_{CK}$  is shown in Figure 2-4 and the description of each component of it summarized in Table 2-5.

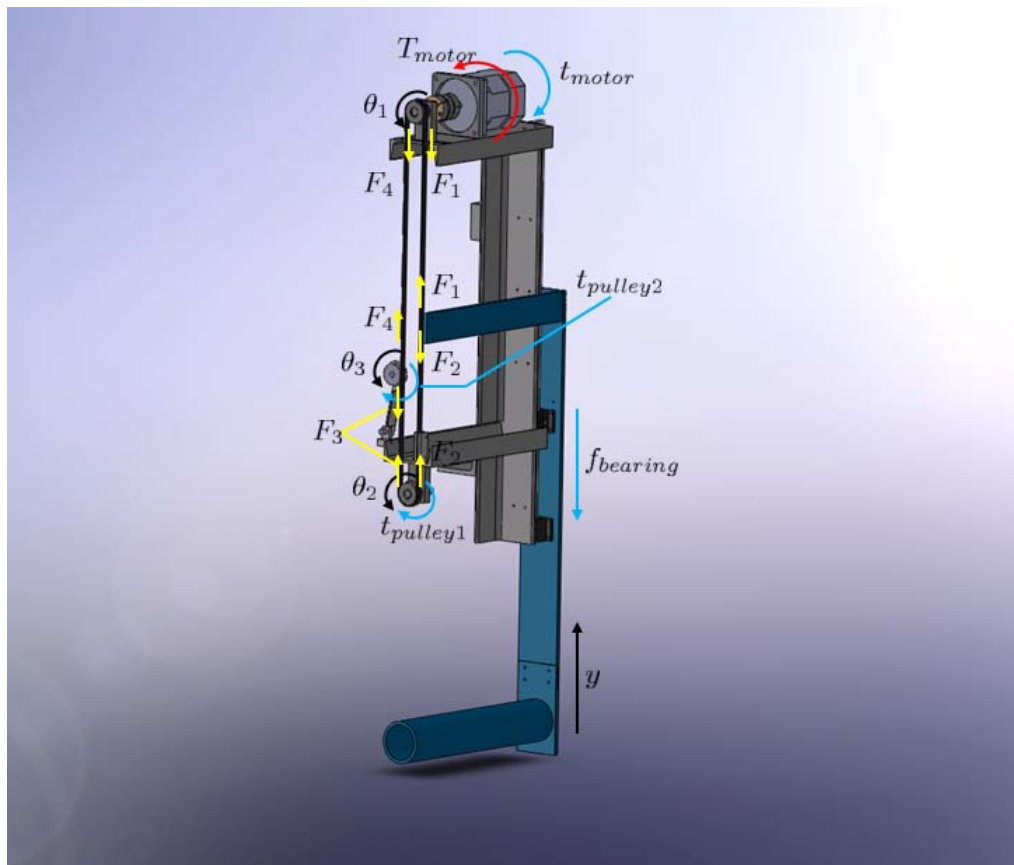


Figure 2-4. Coordinate system of the  $V_{CK}$  VIVACE model

Table 2-5. Description of components of the V<sub>CK</sub> VIVACE model

$\theta_i, i = 1,2,3$	$i=1$ :angle of the rotor $i=2$ :angle of the lower pulley $i=3$ :angle of the idler
$y$	Displacement of the cylinder
$M_{osc}[\text{kg}]$	Mass of oscillating components
$J_{motor}[\text{kg} \cdot \text{m}^2]$	Mass moment of inertia of the rotor
$t_{motor}[\text{N}]$	Damping torque of the motor
$T_{motor}[\text{N}]$	Torque generated by the motor
$J_{pulley}[\text{kg} \cdot \text{m}^2]$	Mass moment of inertia of the pulley
$t_{pulley1}[\text{N}]$	Damping torque of the lower pulley
$t_{pulley2}[\text{N}]$	Damping torque of the idler
$r_{pulley}[\text{m}]$	Radius of the pulley
$f_{bearing}[\text{N}]$	Damping force of all bearings
$F_i, i = 1,2,3,4[\text{N}]$	$i^{\text{th}}$ tension in the timing-belt

Since electrical dynamics of the motor is much faster than mechanical dynamics of the motor, electrical dynamics of the motor is neglected. Also, the gravitational force is ignored assuming the cylinder will be oscillating around the equilibrium position after the virtual spring and damper have been implemented. Thus, equations of motion of the V<sub>CK</sub> VIVACE in the air can be written as:

$$(J_{motor} + J_{pulley})\ddot{\theta}_1 = T_{motor} - t_{motor} + r_{pulley} (F_4 - F_1) , \quad (2-1)$$

$$J_{pulley}\ddot{\theta}_2 = -t_{pulley1} + r_{pulley}(F_2 - F_3) , \quad (2-2)$$

$$J_{pulley}\ddot{\theta}_3 = -t_{pulley2} + r_{pulley}(F_3 - F_4) , \quad (2-3)$$

$$M_{osc}\dot{y} = -f_{bearing} + F_1 - F_4 . \quad (2-4)$$

Assuming that the timing-belt is inelastic, kinematic relationships among  $\theta_1$ ,  $\theta_2$ ,  $\theta_3$  and  $y$  are

$$\theta_1 = \theta_2 = \theta_3 = \theta , \quad (2-5)$$

$$y = r_{pulley}\theta , \quad (2-6)$$

Thus, Eq. (2-1) - Eq. (2-4) are simplified to Eq. (2-7) utilizing Eq. (2-5) and Eq. (2-6).

$$\begin{aligned} & (J_{motor} + 3J_{pulley} + r_{pulley}^2 M_{osc})\ddot{\theta} \\ & = T_{motor} - (t_{motor} + t_{pulley1} + t_{pulley2} + r_{pulley}f_{bearing}) . \end{aligned} \quad (2-7)$$

The linear motion version of Eq. (2-7) is

$$\left(\frac{J_{motor}}{r_{pulley}^2} + \frac{3J_{pulley}}{r_{pulley}^2} + M_{osc}\right)\ddot{y} = F_{motor} - \left(\frac{t_{motor}}{r_{pulley}} + \frac{t_{pulley1}}{r_{pulley}} + \frac{t_{pulley2}}{r_{pulley}} + f_{bearing}\right), \quad (2-8)$$

where  $F_{motor} = T_{motor}/r_{pulley}$ .

Eq. (2-8) can be simplified to Eq. (2-9) for convenience in designing the controller.

$$m\ddot{y} = F_{motor} - f, \quad (2-9)$$

where

$$m = m_{eff} + M_{osc} = \frac{J_{motor}}{r_{pulley}^2} + \frac{3J_{pulley}}{r_{pulley}^2} + M_{osc},$$

$$f = \left(\frac{t_{motor}}{r_{pulley}} + \frac{t_{pulley1}}{r_{pulley}} + \frac{t_{pulley2}}{r_{pulley}} + f_{bearing}\right).$$

## 2.4. Calibration of Motor Torque

A digital controller is composed of an analog/digital converter (ADC), control algorithm and digital/analog converter (DAC). The controller calculates the motor torque using the measurement signals; converts it to corresponding voltage, and applies the voltage to the motor through the DAC and the motor drive. Generally, output voltage of DAC is a scaled and biased version of input voltage of the DAC. Also, we need a correct relationship between output voltage of DAC and the motor torque. Thus, two kinds of calibration tests are needed sequentially: the calibration test between input voltage ( $V_{in}$ ) and output voltage ( $V_{out}$ ) of the DAC and the calibration test between  $V_{out}$  and the motor torque ( $T_{motor}$ ).

In the voltage calibration test,  $V_{out}$  was measured for each  $V_{in}$ . Figure 2-5 shows the input-output relationship of the DAC before calibration was conducted.

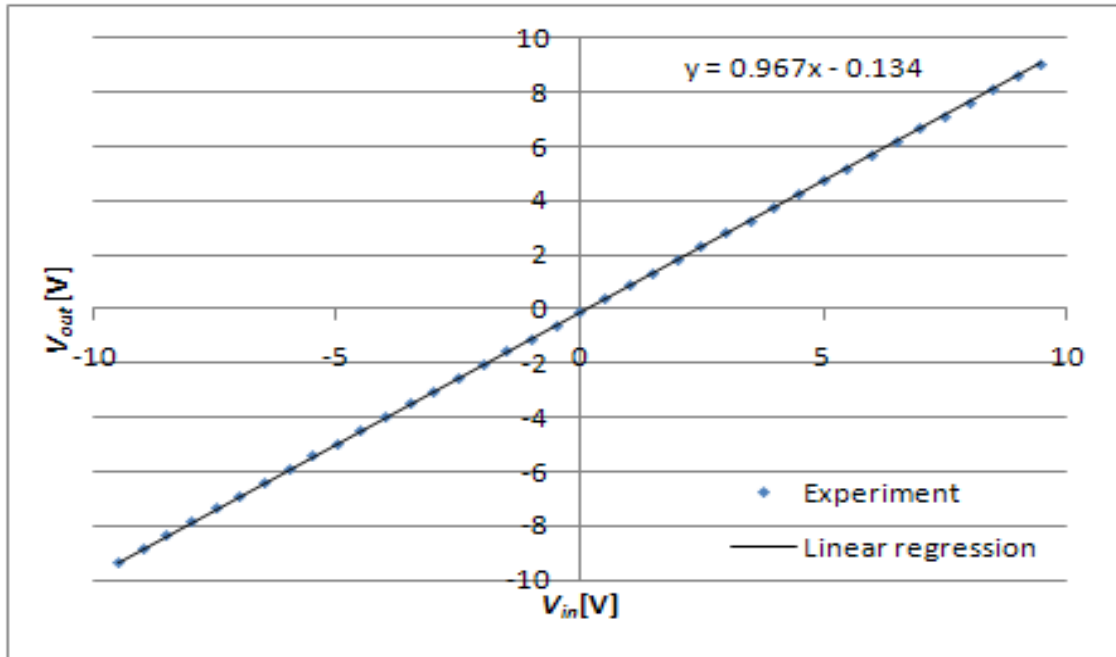


Figure 2-5. Input vs. output voltage of DAC before calibration was conducted.

Linear regression analysis is performed yielding Eq. (2-10).

$$V_{in} = (V_{out} + 0.134)/0.967 . \quad (2-10)$$

The calibration test between  $T_{motor}$  and  $V_{out}$  was performed subsequently. In this test, weights of known value were added on the plate and the displacement of weight was measured. Figure 2-6 shows a schematic of the device for the calibration test.

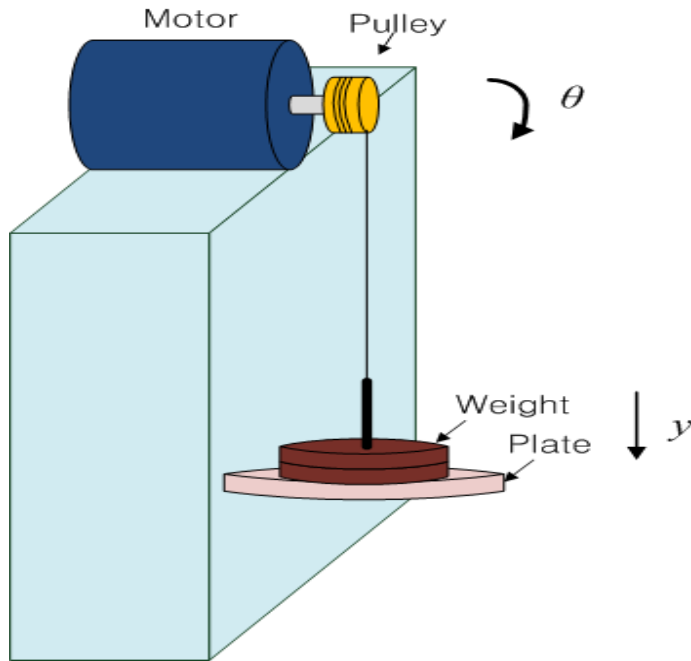


Figure 2-6. Schematic of the device for calibration test

The voltage range of  $V_{out}$  is from -10V to 10V. The desired relationship between  $T_{motor}$  and  $V_{out}$  is that  $T_{motor}$  reaches the nominal torque 7.5 Nm when 10V of  $V_{out}$  is applied. Assuming that  $T_{motor}$  and  $V_{out}$  have linear relationship,  $T_{motor}$  is calculated as:

$$T_{motor} = (k \cdot y) \cdot r_{pulley} = (k \cdot r_{pulley}^2) \cdot \theta = mg \cdot r_{pulley} = a \cdot V_{out}, \quad (2-11)$$

where  $k$ [N/m] is spring constant,  $y$ [m] is the displacement of the weights,  $\theta$ [rad] is the angle measurement,  $m$ [kg] is mass of weights, and  $g$ [m/s<sup>2</sup>] is gravitational acceleration.



In the test,  $k$  is pre-determined and coefficient  $a$  is adjusted until  $y$  satisfies Eq. (2-11).

After trial and error, the resulting calibration formula derived is

$$V_{out} = 0.595 \cdot T_{motor} . \quad (2-12)$$

Eq. (2-12) was verified by checking the displacements of the plate after adding weights one by one. Figure 2-7 shows the relationship between displacement and velocity when  $k = 400 \text{ N/m}$ .

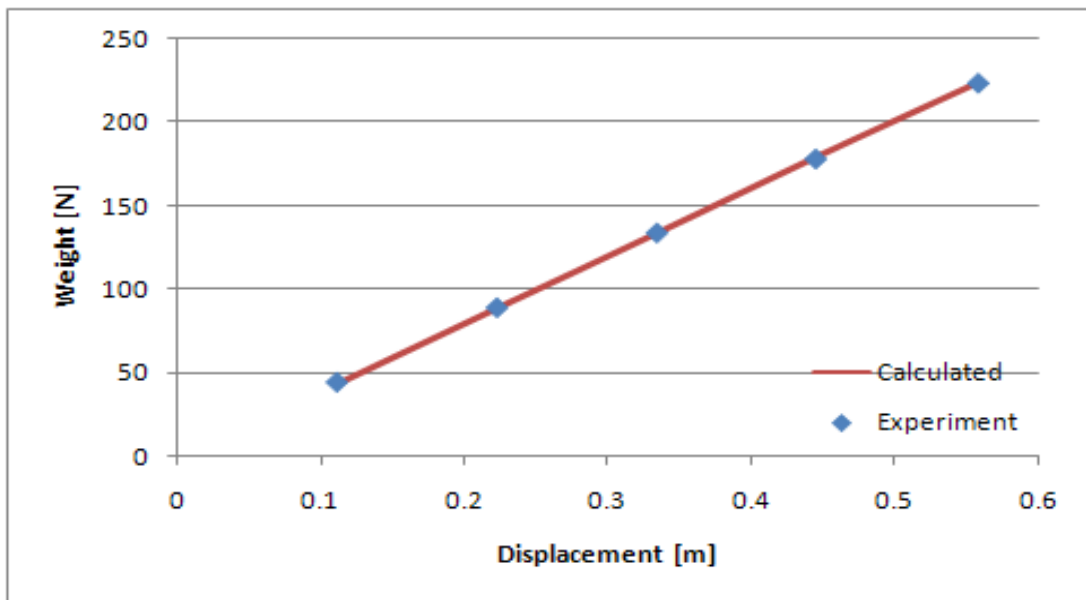


Figure 2-7. Displacement vs. weight after torque-voltage calibration

From Figure 2-7, the relationship between  $T_{motor}$  and  $V_{out}$  is linear as expected and it can be concluded that calibration was done with adequate accuracy.

## **CHAPTER 3.**

### **IDENTIFICATION OF INERTIAL MASS**

#### 3.1. Estimation of Inertial Mass

To design  $V_{CK}$  system, it is necessary to identify the system damping and friction accurately. To perform system identification of the damping and friction inside of the system, the inertial mass shown in Eq. (2-9) should be known priori. Two inertial mass identification methods, free-decay tests and Fourier series method are proposed and compared.

### 3.1.1. Estimation of Inertial Mass by Fourier Series Analysis

#### 3.1.1.1. Solution Approach

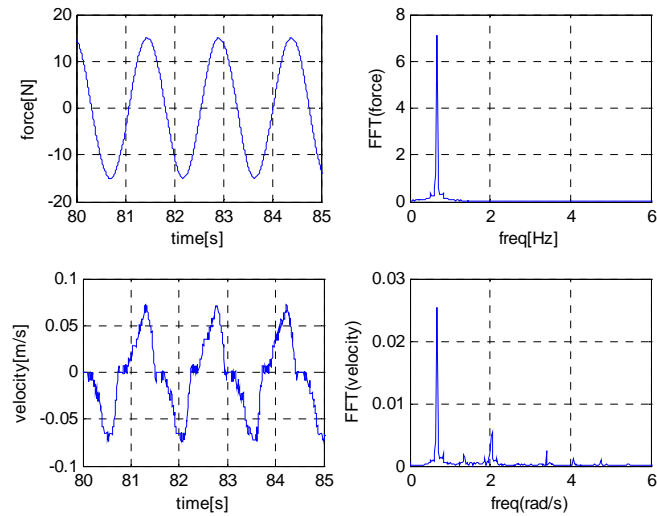


Figure 3-1. Frequency response: forcing amplitude = 15N, forcing frequency = 0.8Hz

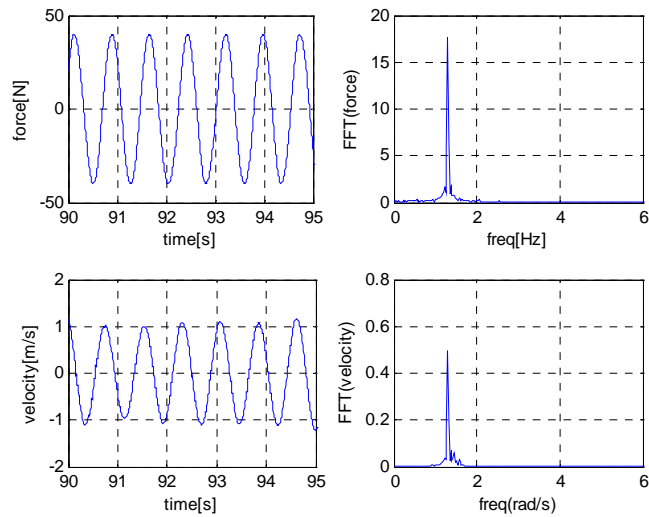


Figure 3-2. Frequency response: forcing amplitude = 40N, forcing frequency = 1.2Hz

Figure 3-1 and Figure 3-2 show typical time history and Fourier Transform results of velocity with low and high amplitude respectively when the motor produces both monochromatic sinusoidal force and spring force to the system. As shown in Figure 3-1 and Figure 3-2, nonlinear behavior becomes significant in the low speed range due to friction force and response is quite linear when amplitude of velocity is high. Thus, Eq. (3-1) approximates the system well if it is guaranteed that the amplitude of the oscillating velocity is high.

$$m\ddot{y} + c\dot{y} + ky = f(t) . \quad (3-1)$$

Fourier series analysis can be used to estimate  $m$  . The motor produces the monochromatic sinusoidal force with the angular frequency  $\Omega$  to the system as well as the spring force. Then we have

$$\begin{aligned} y &= A\cos\Omega t , \\ \dot{y} &= -A\Omega\sin\Omega t , \\ \ddot{y} &= -A\Omega^2\cos\Omega t . \end{aligned} \quad (3-2)$$

Substituting Eq. (3-2) into Eq. (3-1), we have

$$(k - m\Omega^2)A\cos\Omega t - c\Omega A\sin\Omega t = f(t). \quad (3-3)$$

Multiplying  $\cos\Omega t$  on both sides of Eq. (3-3) and integrating them for N periods gives

$$\frac{k - m\Omega^2}{2} ANT = \int_0^{NT} f(t) \cos\Omega t dt . \quad (3-4)$$

Finally, inertial mass is given by

$$m = \frac{k}{\Omega^2} - \frac{1}{AN\Omega\pi} \int_0^{NT} f(t) \cos\Omega t dt . \quad (3-5)$$

The proposed inertial mass estimation method using Fourier series analysis is validated by simulation. In the simulation model, sinusoidal force input  $A_{force} \cos(\Omega t + \varphi)$  is applied. A kinetic friction model is included to investigate the error due to it on the estimated mass. Figure 3-3 shows the model used for the inertial mass estimation.

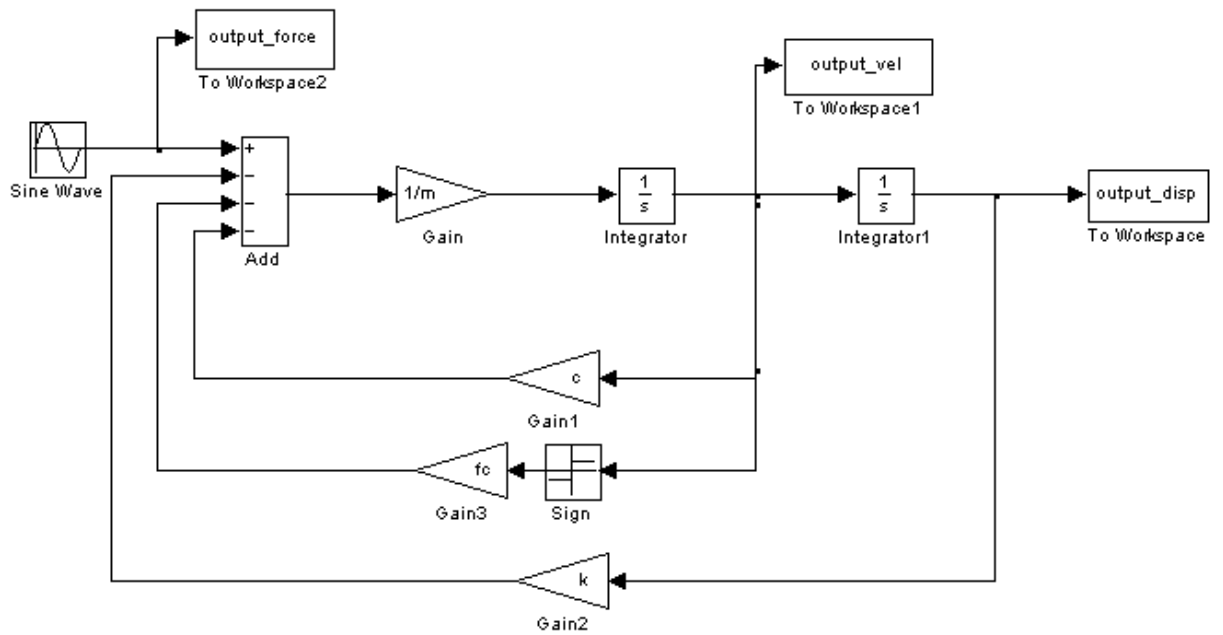


Figure 3-3. Simulation model for the inertial mass estimation

The values of  $m$ ,  $c$  and  $f_c$  are chosen based on those from the old VIVACE apparatus. Also, three different kinetic friction values are used and estimation errors are compared. Simulation parameters are listed in Table 3-1.

Table 3-1. Simulation parameters

$m$ [kg]	$c$ [Ns/m]	$k$ [N/m]	$\Omega$ [Hz]	$A_{force}$ [N]	$f_c$ [N]
11.333	18	1000	1	100	0,5,10

Runge-Kutta 4<sup>th</sup> order method is used as the simulation solver with time step 0.001 second and trapezoidal rule is used to evaluate the integration on the right hand side in Eq. (3-5). Simulation is performed for 100 seconds and only 50s – 100s data are used for the analysis to eliminate initial condition effect. Estimated mass and error for each case are listed in Table 3-2.

Table 3-2. Estimated mass and error for different Coulomb friction cases

$f_c$	Estimated $m$ [kg]	error
0N	11.349	0.14%
5N	11.294	0.35%
10N	11.214	1.05%

As shown in Table 3-2, kinetic friction makes Fourier series analysis underestimate the value of mass. However, Fourier series analysis results in good agreement even with 10N of Coulomb friction. Also, we can expect less error in mass estimation if we make the motor compensate some part of kinetic friction while performing the experiment.

### 3.1.1.2. Experimental Results and Analysis

Four tests with two forcing frequencies and two forcing amplitudes were performed to estimate inertial mass of the VIVACE apparatus. During experiments, spring stiffness  $k$  is fixed as 1000 N/m. Data were recorded for 100 seconds and only 50s – 100s data were used for the analysis to eliminate initial condition effect. Experimental conditions and estimated mass for each case are listed in Table 3-3. Experimental results for both cases are shown in Figure 3-4 through Figure 3-7.

Table 3-3. Experimental conditions and estimated mass

Test No.	$A_{force}$ [N]	$\Omega$ [Hz]	Estimated $m$ [kg]
1	12	1.5	11.03
2	14	1.5	11.07
3	10	1.6	10.83
4	12	1.6	10.87
Average	10.95	Standard Deviation	0.118



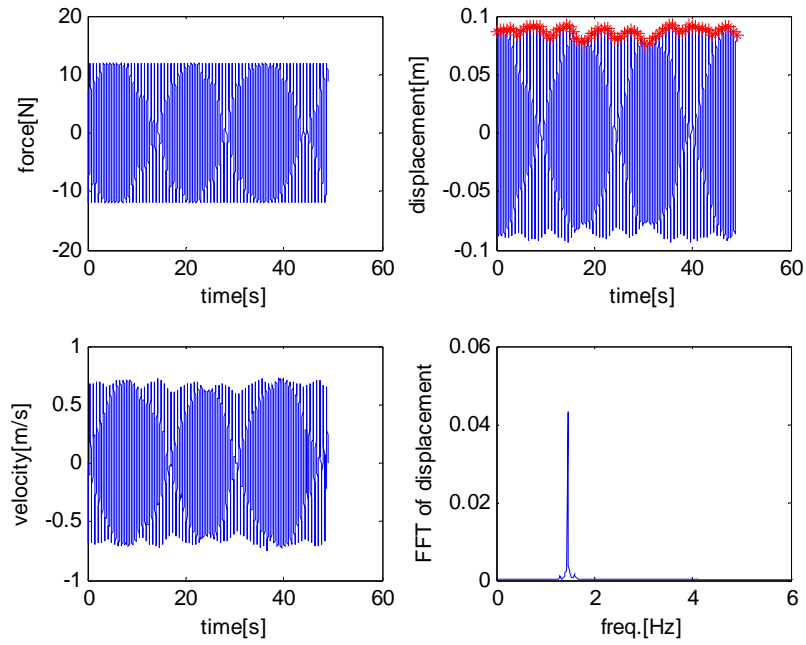


Figure 3-4. Experimental Result:  $A_{force} = 12\text{N}$ ,  $\Omega = 1.5\text{Hz}$

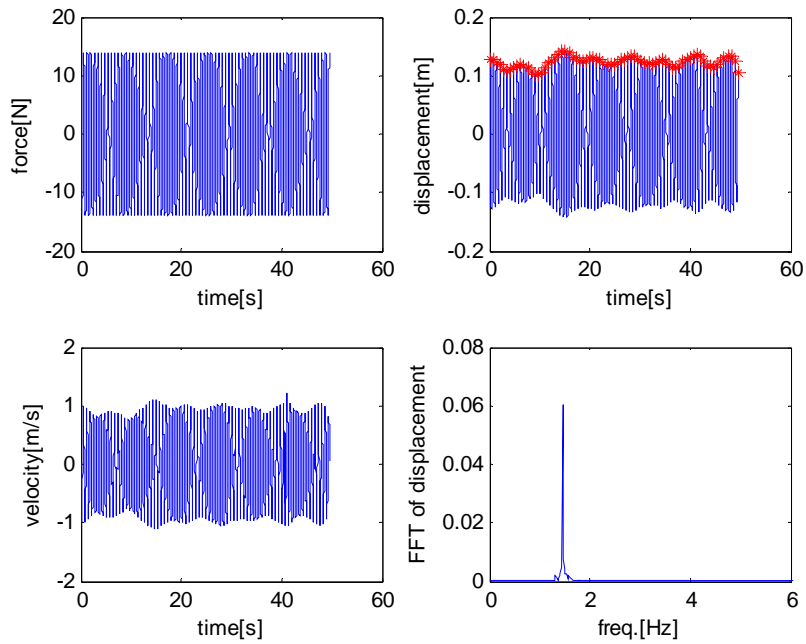


Figure 3-5. Experimental Result:  $A_{force} = 14\text{N}$ ,  $\Omega = 1.5\text{Hz}$

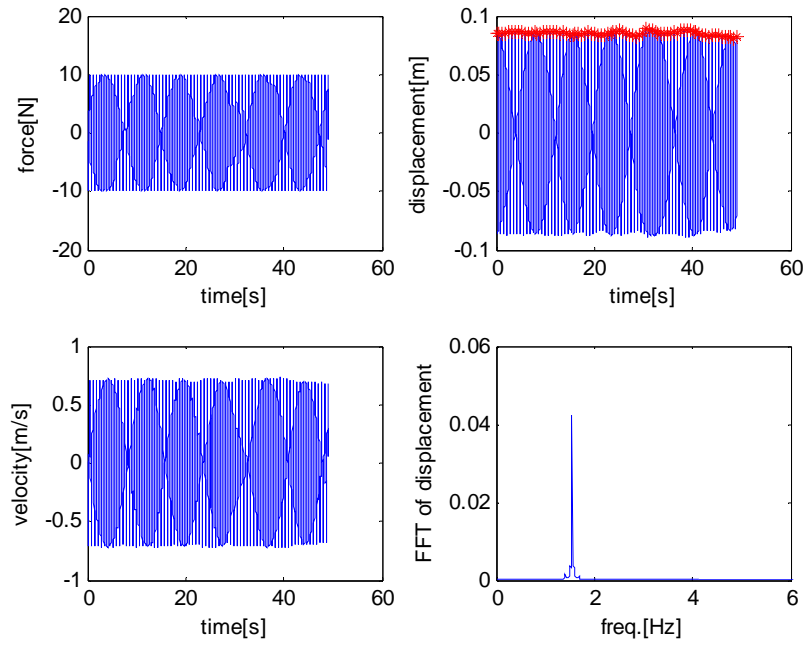


Figure 3-6. Experimental Result:  $A_{force}=10\text{N}$ ,  $\Omega=1.6\text{Hz}$

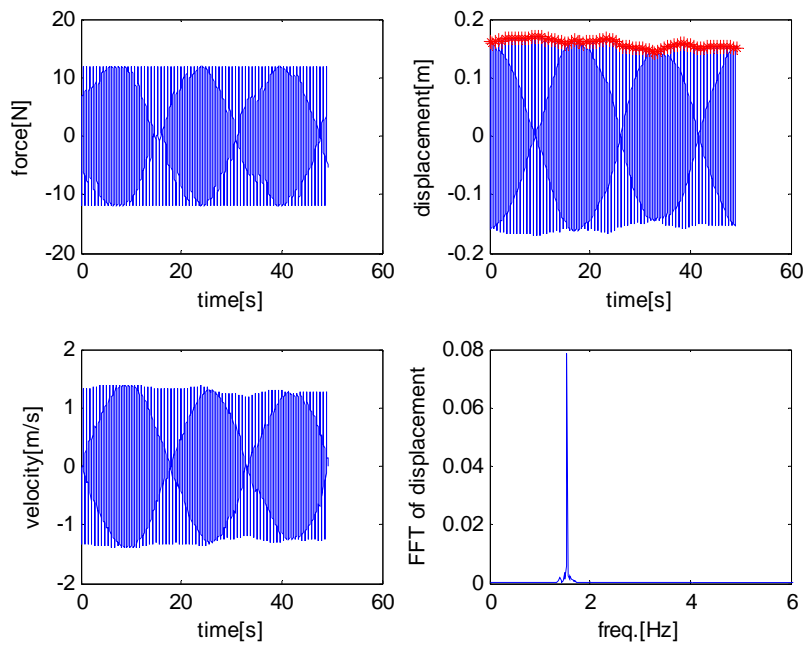


Figure 3-7. Experimental Result :  $A_{force}=10\text{N}$ ,  $\Omega =1.6\text{Hz}$

### 3.1.2. Estimation of Inertial Mass by Free Decay Tests

#### 3.1.2.1. Solution Approach

The inertial mass  $m$  is composed of the mass of the oscillating part  $M_{osc}$  and inertial mass effect of the motor-pulley-belt system  $m_{eff} = (J_{motor} + 3J_{pulley})/r_{pulley}^2$ .  $m$  can be estimated after performing the free-decay tests for the motor-pulley-belt system since the weight of  $M_{osc}$  was already measured. Practically, the viscous damping of the AC servo motor and pulleys is small and the friction of them is relatively high. Hence,  $f(\dot{y})$  in Eq. (2-9) is modeled as sum of linear viscous damping  $c_{eff}\dot{y}$  and kinetic friction  $f_c \text{sgn}(\dot{y})$ . Also, the motor produces restoring force with spring constant  $k$  to give the restoring force to the motor-pulley-belt system. Thus, the mathematical model for free-decay tests for the motor-pulley-belt system is:

$$m_{eff}\ddot{y} + c_{eff}\dot{y} + ky + f_c \text{sgn}(\dot{y}) = 0 . \quad (3-6)$$

Eq. (3-6) can be separated into two equations depending on the sign of the velocity.

$$m_{eff}\ddot{y} + c_{eff}\dot{y} + ky = -f_c \quad \text{for } \dot{y} > 0 . \quad (3-7)$$

$$m_{eff}\ddot{y} + c_{eff}\dot{y} + ky = f_c \quad \text{for } \dot{y} < 0 . \quad (3-8)$$

The solution of Eq. (3-6) is obtained by solving Eq. (3-7) and Eq. (3-8) alternatively considering the displacement and velocity at the moment that sign of  $\dot{y}$  changes. The general solution of Eq. (3-7) and Eq. (3-8) has the form of  $Ae^{-\zeta\omega_n t} \cos(\omega_d t + \phi) + B$ . Thus, we can see that kinetic friction does not affect the damped natural frequency or damped natural period. Also, when viscous damping is reasonably small following equations hold.

$$\omega_d = \frac{2\pi}{T_d} = \omega_n \sqrt{1 - \zeta^2} \cong \omega_n = \sqrt{\frac{k}{m}}. \quad (3-9)$$

Thus, inertial mass estimation of the motor-pulley-belt system is given by

$$m_{eff} \cong \frac{kT_d^2}{4\pi^2}. \quad (3-10)$$

### 3.1.2.1. Experimental Results and Analysis

Free-decay tests for the motor-pulley-belt system were performed 10 times with initial displacement of 0.2m and spring stiffness  $k$  of 1000N/m. Damped natural period  $T_d$  between 1<sup>st</sup> and 2<sup>nd</sup> peak was measured and inertial mass of the motor-pulley-belt was estimated using Eq. (3-10). Since all tests showed very consistent results only the first test result is shown in Figure 3-8.

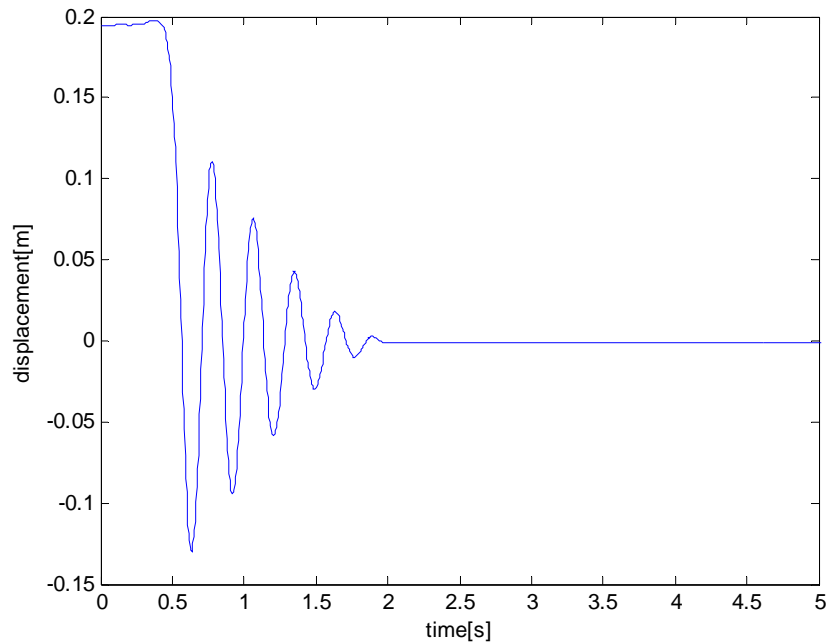


Figure 3-8. Result of the free-decay test for the motor-pulley-belt system:  $k=1000$  N/m, initial displacement = 0.2 m

The results of 10 tests and estimated mass are listed in Table 3-4.

Table 3-4. Results of free-decay tests

Test No.	Estimated $m_{eff}$ [kg]		$Td$ [s]
1	2.0575		0.285
2	2.0575		0.285
3	2.0575		0.285
4	2.0575		0.285
5	2.0575		0.285
6	2.0575		0.285
7	2.0575		0.285
8	2.0575		0.285
9	2.0575		0.285
10	2.0575		0.285
Average	2.0575	Standard Deviation	0
Mass of the oscillating part [kg]		8.88	
Estimated $m$ [kg]		10.9375	

## CHAPTER 4.

# IDENTIFICATION OF NONLINER STATIC DAMPING MODEL

A series of models of gradually increasing complexity are tried to identify the VIVACE model damping. These are described in this chapter in the next few sections.

### 4.1. Identification of Linear Viscous Damping + Kinetic Friction

#### Model

The first damping model is assumed to be composed of linear viscous damping and kinetic friction which comes from motor, pulleys and bearings:

$$\begin{aligned} f = f(\dot{y}) &= c\dot{y} + f_k \text{sgn}(\dot{y}) \\ &= (c_{motor} + c_{pulley} + c_{bearing})\dot{y} \\ &\quad + (f_{motor} + f_{pulley} + f_{bearing})\text{sgn}(\dot{y}). \end{aligned} \tag{4-1}$$

The damping model shown in Eq. (4-1) is used for the old  $V_{CK}$  VIVACE apparatus described in Section 2.1.1. Experiments to identify the coefficients in Eq. (4-1) were performed for the following three cases.

1. motor-only
2. system without oscillating parts
3. system with oscillating parts

The basic idea of the identification method is that the feedforward controller produces accurate command tracking, whereas the feedback controller tries to reject disturbances caused by modeling error. Thus, the feedback controller can be regarded as a disturbance torque estimator (Johnson and Lorenz 1992). The block diagram of the identification method is shown in Figure 4-1.

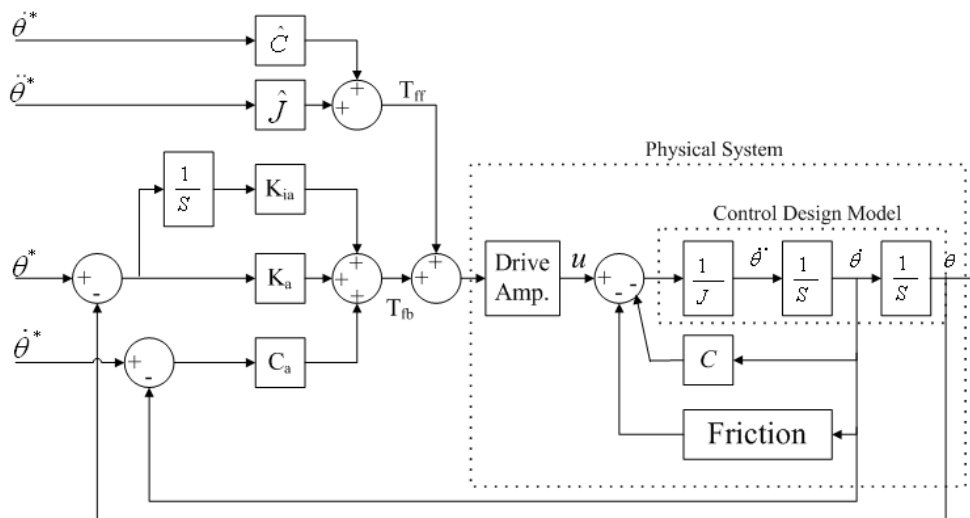


Figure 4-1. Block diagram of identification method (Johnson and Lorenz 1992)



Input profiles were selected as listed in Table 4-1, considering that maximum velocity of the cylinder undergoing vortex-induced vibration has been measured around 1.5 m/s.

Table 4-1. Input profile particulars

Case No.	Velocity Profile Shape	Max. Input Velocity[m/s]
1, 2	Trapezoidal	2.5
3	Triangular	0.5

As shown in Table 4-1, the input velocity in case 3 could not be raised to the maximum operating velocity of 1.5m/s due to the length limitation of the shaft, whereas case 1 and case 2 did not have the length limitation. When maximum input velocity higher than 0.5m/s was used with the particulars in case 3, parameters could not be identified because of the large overshoot in the response just after velocity changed its sign. Thus, in the velocity range greater than 0.5m/s in magnitude, extrapolation is inevitable when estimating viscous damping coefficient and kinetic friction. This can cause discrepancy in displacement when the velocity of the cylinder is much higher than 0.5 m/s. In Sections 4.3 and 5, other system identification methods that overcome the limitations of the length limit in the shaft will be introduced. Time histories of input, measured output, and estimated forces vs. velocity for each experiment are shown in Figure 4-2 through Figure 4-7.

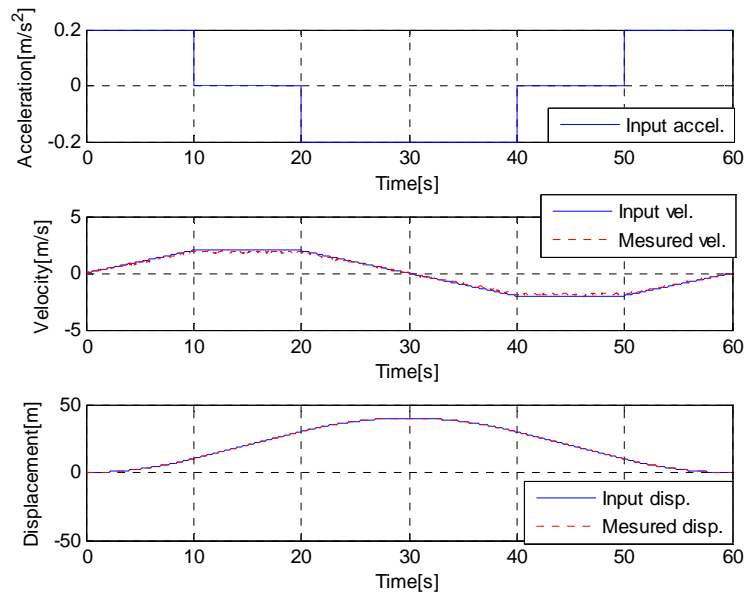


Figure 4-2. Input profile and measured output in case 1

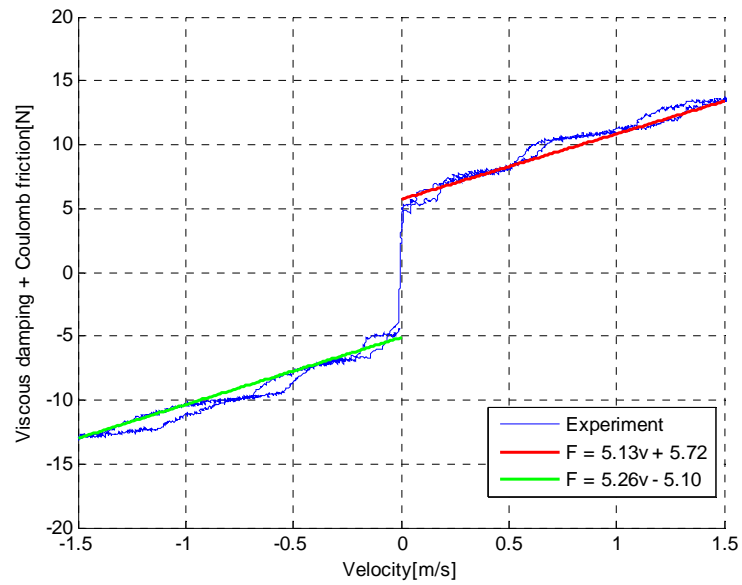


Figure 4-3. Estimated viscous damping + Coulomb friction in case 1

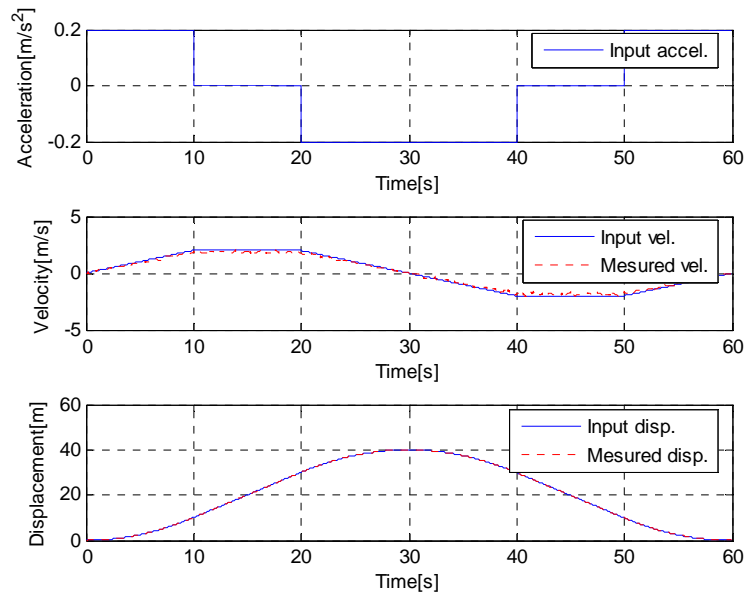


Figure 4-4. Input profile and measured output in case 2

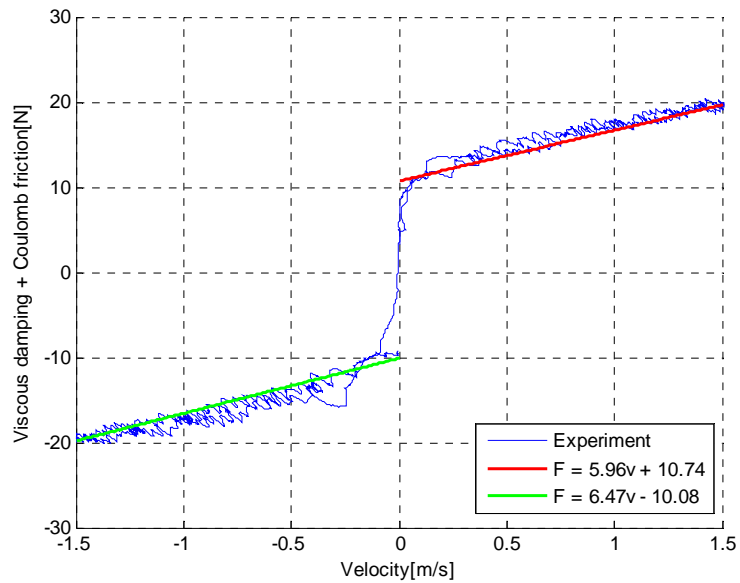


Figure 4-5. Estimated viscous damping + Coulomb friction in case 2

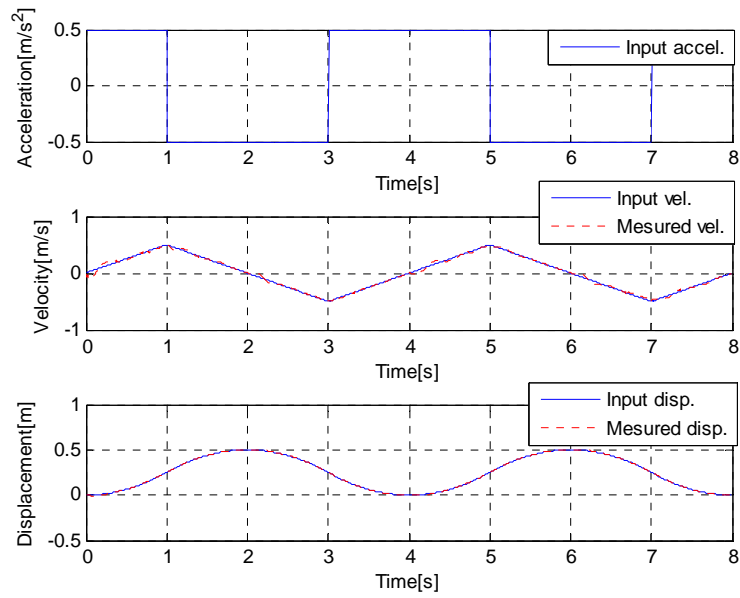


Figure 4-6. Input profile and measured output in case 3

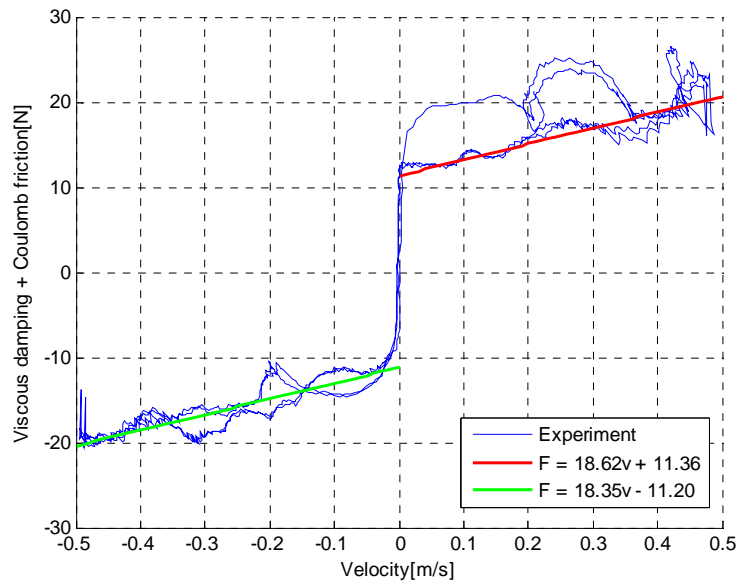


Figure 4-7. Estimated viscous damping + Coulomb friction in case3

Table 4-2 summarizes the results of system identification, where linear regression results of both positive and negative velocity cases were averaged.

Table 4-2. System identification results

$c_{motor}$	5.21Ns/m	$f_{motor}$	5.41N
$c_{pulley}$	1.01Ns/m	$f_{pulley}$	5.00N
$c_{bearing}$	12.27Ns/m	$f_{bearing}$	0.87N

Based on the system identification results listed in Table 4-2, a controller for the  $V_{CK}$  VIVACE model is designed in Eq. (4-2) which compensates the damping and friction forces from the motor and pulleys.

$$F_{motor} = f(\dot{y}) - c_{virtual}\dot{y} - k_{virtual}y = (c_{motor} + c_{pulley} + c_{bearing})\dot{y} + (f_{motor} + f_{pulley} + f_{bearing})\text{sgn}(\dot{y}) - (c_{motor} + c_{pulley})\dot{y} - (f_{motor} + f_{pulley})\text{sgn}(\dot{y}) - k_{virtual}\dot{y}. \quad (4-2)$$

The  $V_{CK}$  VIVACE model was tested in the Low Turbulence Free Surface Water Channel and the amplitude the ratio ( $A/D$ ) of the cylinder was recorded.  $A/D$  results produced by the  $V_{CK}$  VIVACE model are compared to  $A/D$  produced by the VIVACE model with real springs. Figure 4-8 shows  $A/D$  versus reduced velocity ( $U^*$ ) for both cases of the VIVACE model.

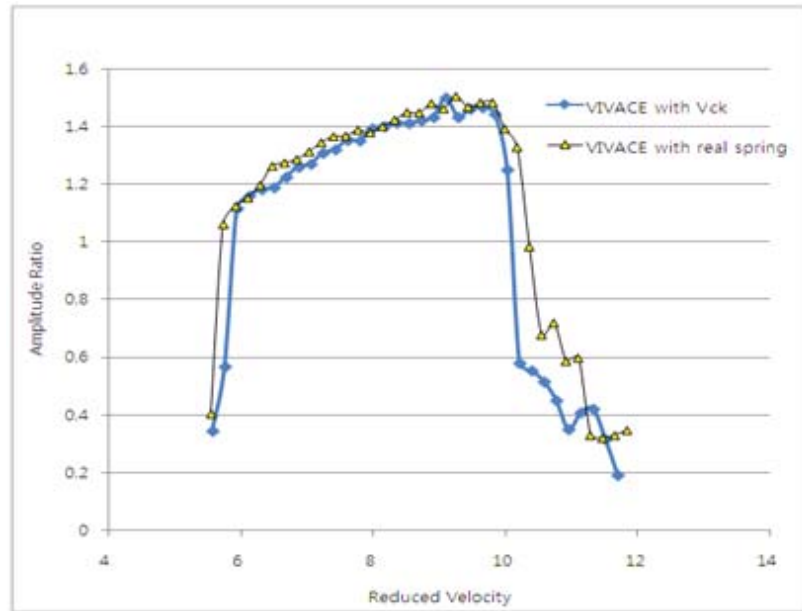


Figure 4-8.  $A/D$  :  $V_{CK}$  VIVACE model vs. VIVACE model with real springs when  $k=883$  N/m

Even though the  $A/D$  data for the two cases compare well in the synchronization range, VIV starts later and ends earlier, when the  $V_{CK}$  VIVACE model is used. The reason of the discrepancy between the two cases of  $A/D$  is attributed to the fact that only kinetic friction is considered in the mathematical model of the  $V_{CK}$  VIVACE model. Also, extrapolation where the velocity is greater than 0.5 m/s contributes to difference between VIV results generated by the  $V_{CK}$  VIVACE model and the VIVACE model with real springs.

## 4.2. Identification of 3<sup>rd</sup> Order Polynomial Damping Model

### 4.2.1. 3<sup>rd</sup> Order Polynomial Damping Model

As explained in Section 3.1.1.1, the kinetic friction effect in the velocity response is dominant when the forcing amplitude is small. Figure 4-9 shows a typical time history and the Fourier transform result of the velocity when the forcing amplitude is small.

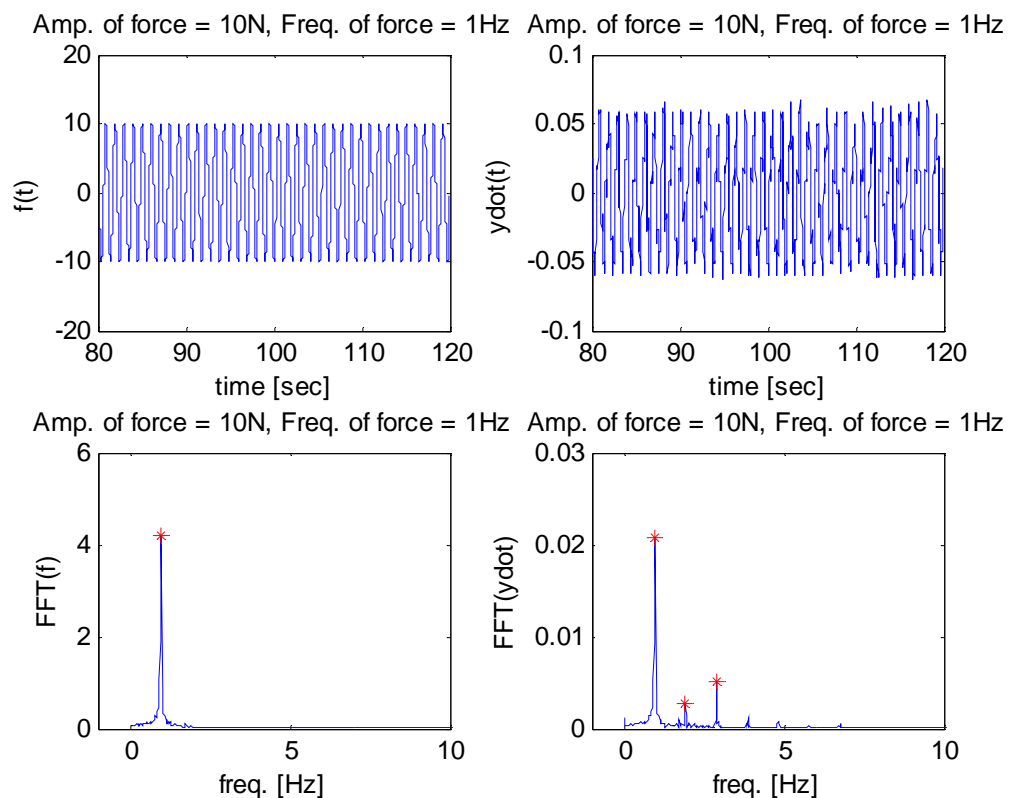


Figure 4-9. Force, velocity and their Fourier transform – Forcing Freq. = 1Hz, Forcing Amp. = 10N

We can see from Figure 4-9 that velocity is mainly composed of 1<sup>st</sup>, 2<sup>nd</sup> and 3<sup>rd</sup> harmonics. The higher-than-third order terms are expected to be attenuated, within the frequency band of interest, by the low-pass nature of the mechanical system at hand.

Therefore, only the first and third harmonics in the velocity response are expected to be of power level significantly higher than the noise. This observation motivates to make an assumption that damping force is composed of the kinetic friction approximated as third order polynomial and linear viscous damping. Thus, the damping model used in this section is given as:

$$f = f(\dot{y}) = c_1\dot{y} + c_3\dot{y}^3 . \quad (4-3)$$



### 4.2.1. Damping Model Identification

In order to determine the damping model structure in Eq. (4-1), a series of experiments was performed. In each experiment, the motor generated a sinusoidal force together with the spring force whose stiffness was 845 N/m. Five forcing frequencies were considered and for each forcing frequency, one to three amplitude values were applied. Input force particulars are summarized in Table 4-3.

Table 4-3. Input force particulars

Forcing frequency [Hz]	Amplitude [N]		
0.8	10	20	25
1.0	10	20	25
1.2	10	20	25
1.4	10	14	
1.6	10	14	

The input, driving force was applied for two minutes. To eliminate transient effects due to initial conditions, only the data of the last 40 seconds of each run were used for system identification. The equation of motion for the experiments is given as:

$$m\dot{v} + c_1v + c_3v^3 + ky = A_q\sin(\Omega_q t + \varphi), v(t) = \dot{y}(t), \quad (4-4)$$

where  $y(t)$  and  $v(t)$  are the cylinder's displacement (position) and velocity, respectively,  $m$  is the inertial mass,  $c_1$  and  $c_3$  the damping coefficients, and  $k$  is the spring constant of the system. Finally,  $A_q$  stands for the driving force's amplitude and  $\Omega_q$  for its frequency. The identification procedure is based on numerical minimization of the following cost function:

$$J(c_1, c_3) = \sum_q \left\{ \begin{aligned} & [V_{<1>}(A_q, \Omega_q) - \hat{V}_{<1>}(A_q, \Omega_q, c_1, c_3)]^2 \\ & + [V_{<3>}(A_q, \Omega_q) - \hat{V}_{<3>}(A_q, \Omega_q, c_1, c_3)]^2 \end{aligned} \right\}, \quad (4-5)$$

where  $V_{<1>}$  and  $V_{<3>}$  are the first and third harmonic of the velocity response of the system, respectively. The 'hat' indicates the velocity response of the mathematical model in Eq. (4-4). Both the actual system's and mathematical model's responses are functions of the driving force amplitude,  $A_q$ , and frequency  $\Omega_q$ . However, the 'hat' response is also function of the values of the unknown damping constants  $c_1$  and  $c_3$  to be determined through system identification. The numerical minimization algorithm is therefore attempting to minimize  $J$  in Eq. (4-5) so that the model response is as close as possible to the actual velocity response recorded in the experiments. The estimated values for  $c_1$  and  $c_3$  after system identification are listed in Table 4-4. Comparison of time history and Fourier transform of velocities from experiments with those from simulation are made in Figure 4-10 through Figure 4-14.

Table 4-4. Estimated coefficients

Coefficient	Estimated value	Value of J
$c_1$ [kg/s]	44.63	0.01
$c_3$ [kg·s/m <sup>2</sup> ]	-56.64	

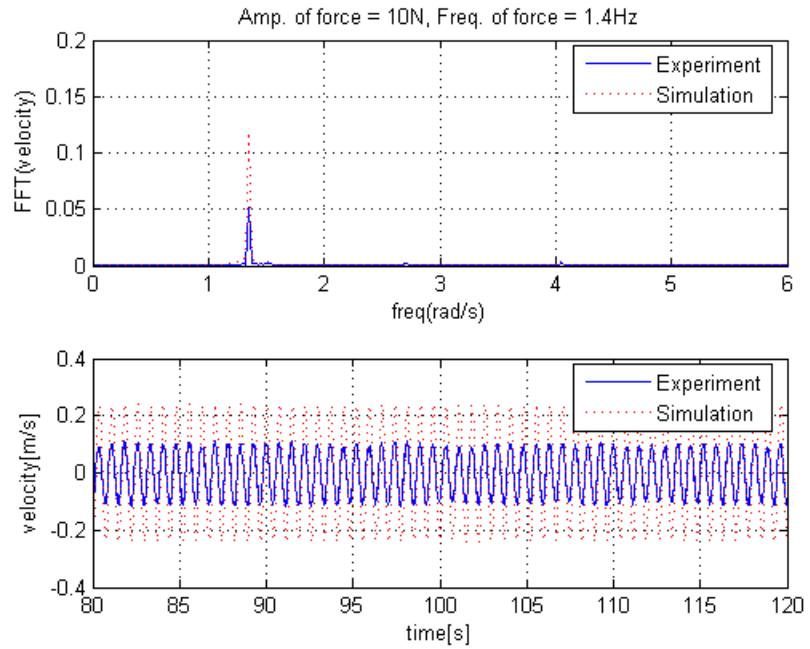


Figure 4-10. FFT and time series of velocity from experiment and simulation - Forcing Freq. = 1.4Hz, Forcing Amp. = 10N

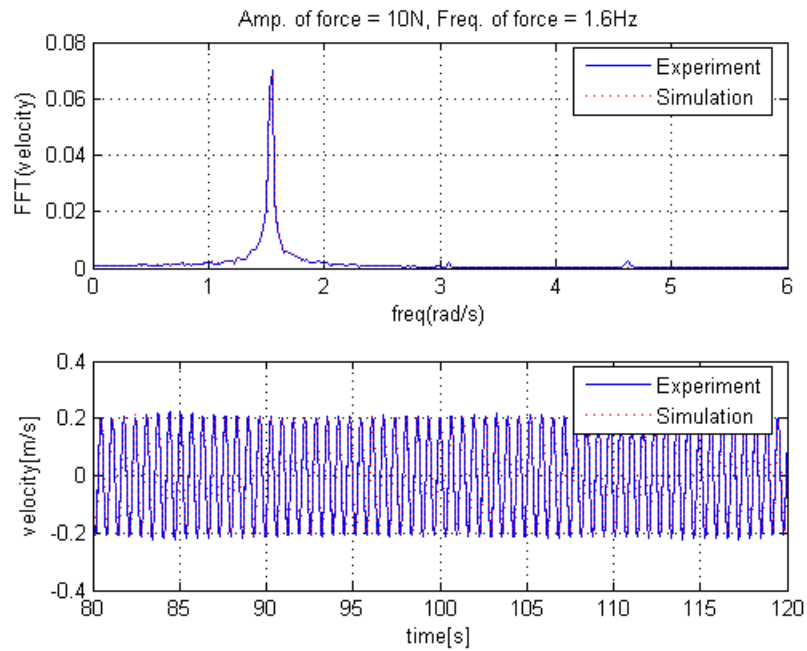


Figure 4-11. FFT and time series of velocity from experiment and simulation - Forcing Freq. = 1.6Hz, Forcing Amp. = 10N

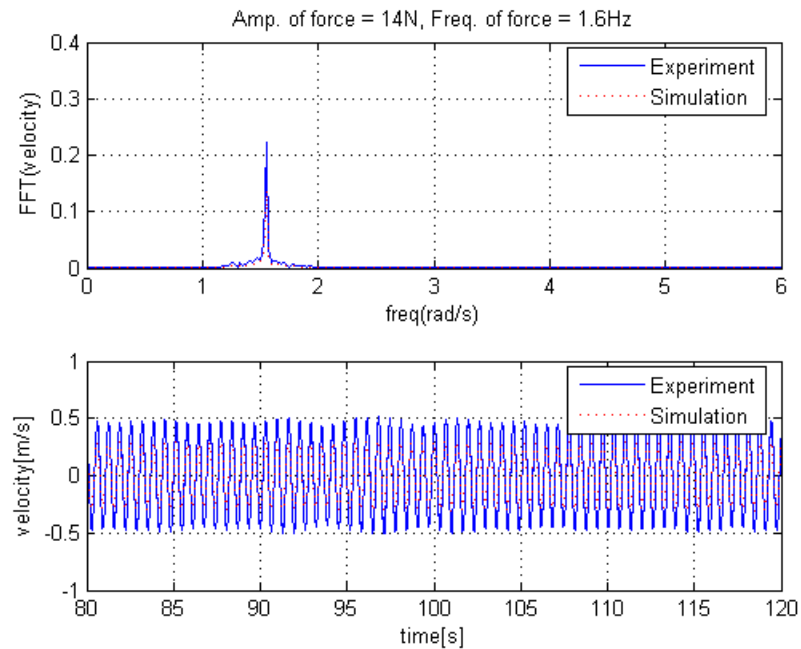


Figure 4-12. FFT and time series of velocity from experiment and simulation - Forcing Freq. = 1.6Hz, Forcing Amp. = 14N

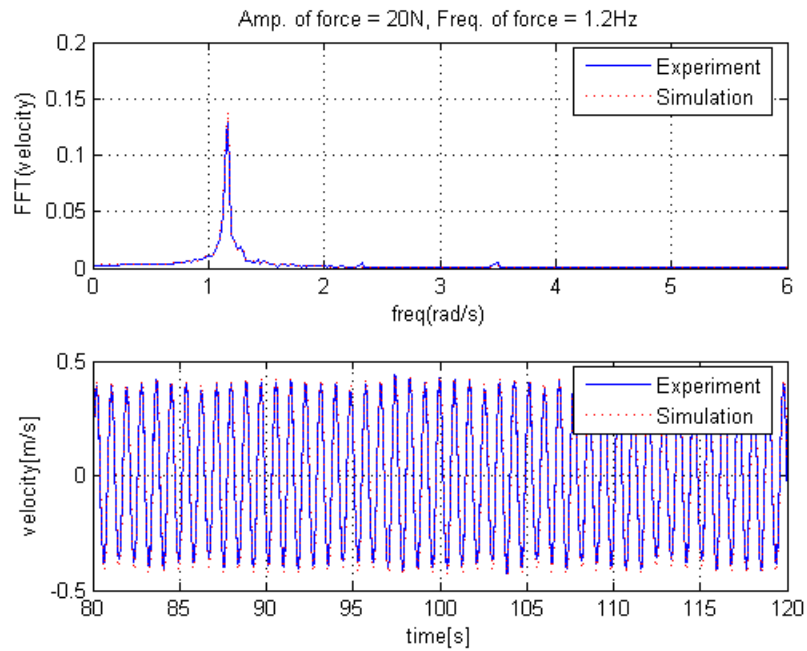


Figure 4-13. FFT and time series of velocity from experiment and simulation - Forcing Freq. = 1.2Hz, Forcing Amp. = 20N

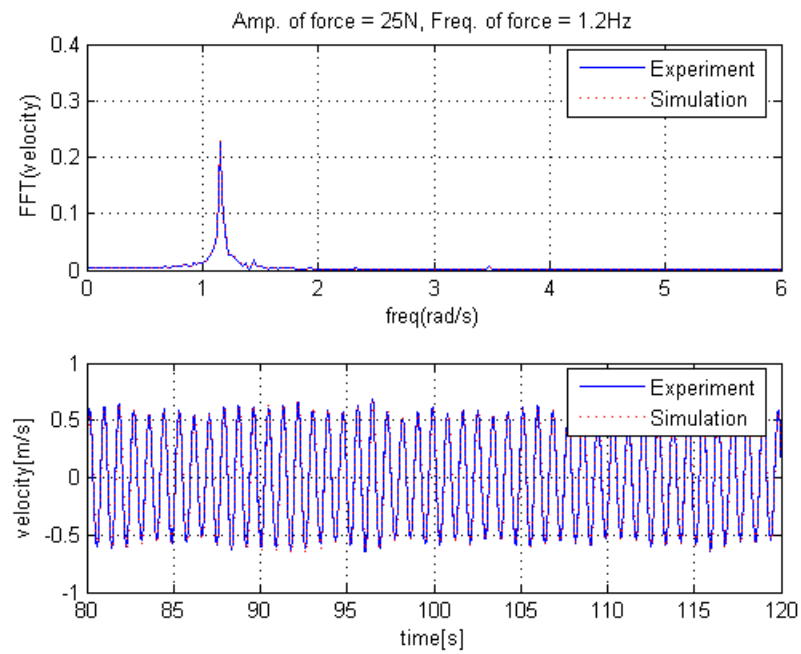


Figure 4-14. FFT and time series of velocity from experiment and simulation - Forcing Freq. = 1.2Hz, Forcing Amp. = 25N

Given the system identification results, the 3<sup>rd</sup> order polynomial damping model is fit to describe the damping process of the system only in the medium to high frequency range. An appropriate extension, by adding nonlinear dynamic terms in the associated mathematical model is needed for the low frequency range.

### 4.3. Identification of Nonlinear Viscous Damping + Kinetic Friction Model and Controller Design

#### 4.3.1. Damping Model and Identification

As shown in Eq. (2-9),  $f$  is total damping force which comes from the motor, pulleys and bearings. Thus  $f$  can be expressed as:

$$f = f_{motor+pulley} + f_{bearing} . \quad (4-6)$$

In this section,  $f_{motor+pulley}$  is assumed as sum of nonlinear viscous damping of 3<sup>rd</sup> order polynomials and kinetic friction.

$$f_{motor+pulley} = c_1\dot{y}^3 + c_2\dot{y}^2 \cdot \text{sgn}(\dot{y}) + c_3\dot{y} + c_4\text{sgn}(\dot{y}). \quad (4-7)$$

To identify  $f_{motor+pulley}$ , various constant forces are applied by the motor in turns and corresponding steady velocities are measured. Figure 4-15 shows the experimental and curve fitting results and resulting regression equations are shown in Eq. (4-8). Also, Table 4-5 shows the estimation errors of Eq. (4-8).

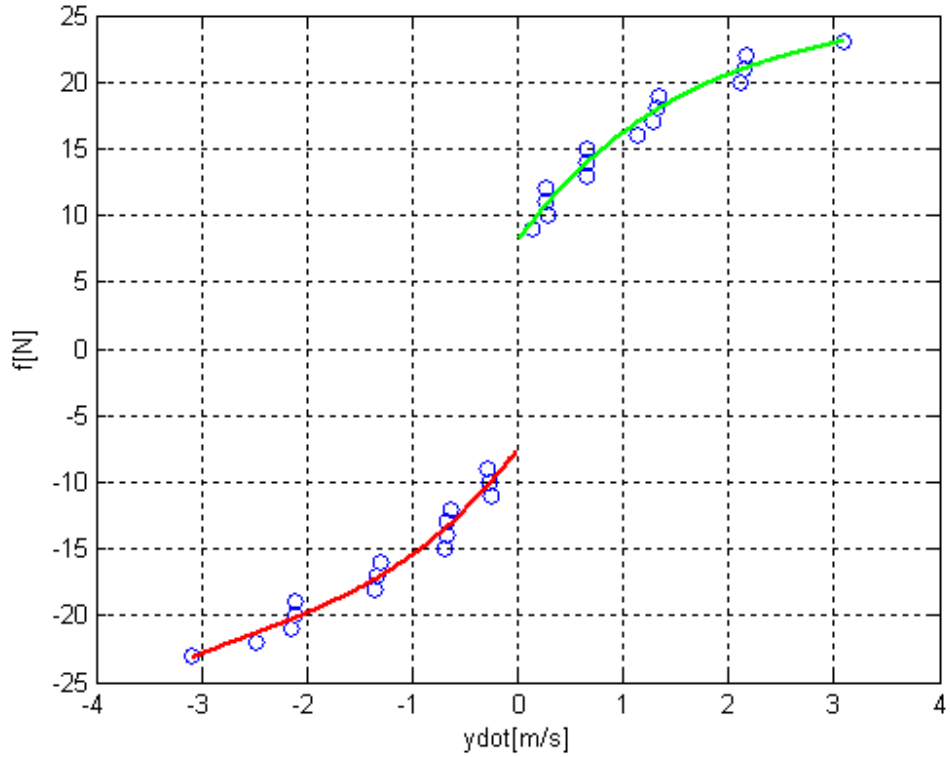


Figure 4-15. Force-velocity map – circles : experimental data. Solid line: nonlinear regression curve

$$f(\dot{y}) = 0.2683\dot{y}^3 - 2.6265\dot{y}^2 + 10.3846\dot{y} + 8.1392, \dot{y} > 0,$$

(4-8)

$$f(\dot{y}) = 0.3625\dot{y}^3 + 2.8255\dot{y}^2 + 10.3216\dot{y} - 7.5587, \dot{y} < 0.$$



Table 4-5. Estimation errors of Eq. (4-8)

$\dot{y} > 0$			$\dot{y} < 0$		
Force[N]	Velocity[m/s]	Residuals[N]	Force[N]	Velocity[m/s]	Residuals[N]
9	0.1415	-0.5569	-23	-3.0943	0.1839
12	0.2749	1.199	-22	-2.4818	-0.6868
11	0.2753	0.1956	-21	-2.1387	-0.744
10	0.2767	-0.8174	-20	-2.1039	0.1435
14	0.6494	0.1512	-19	-2.1017	1.1365
15	0.6498	1.1482	-18	-1.3497	-0.7662
13	0.6528	-0.8733	-17	-1.3341	0.1608
16	1.1259	-0.8848	-16	-1.3049	1.0216
17	1.2874	-0.7274	-15	-0.6994	-1.4807
18	1.3155	0.1347	-14	-0.6716	-0.6737
19	1.3409	1.0117	-13	-0.6648	0.2781
20	2.119	-0.903	-12	-0.6397	1.1004
21	2.1448	0.0235	-9	-0.2834	1.2652
22	2.1722	0.9469	-10	-0.261	0.0669
23	3.081	-0.0478	-11	-0.2529	-1.0057

where Residuals = Force  $-f(\dot{y})$

For estimation of  $f_{bearing}$ , the method mentioned above cannot be used because there is length limitation due to the shaft. Instead, free decay tests are used to estimate  $f_{bearing}$ . During the tests, the oscillating part is disconnected from the timing belt so that damping force is only from  $f_{bearing}$ . Thus, in order to perform free decay tests, restoring force is given by two real springs with total spring stiffness of 775N/m instead of the motor. It is assumed that damping force is only proportional to the velocity. Ten free decay tests are

performed and one of test results is shown in Figure 4-16. Averaged linear damping coefficient is 4.33 Ns/m and standard deviation is 0.07 Ns/m.

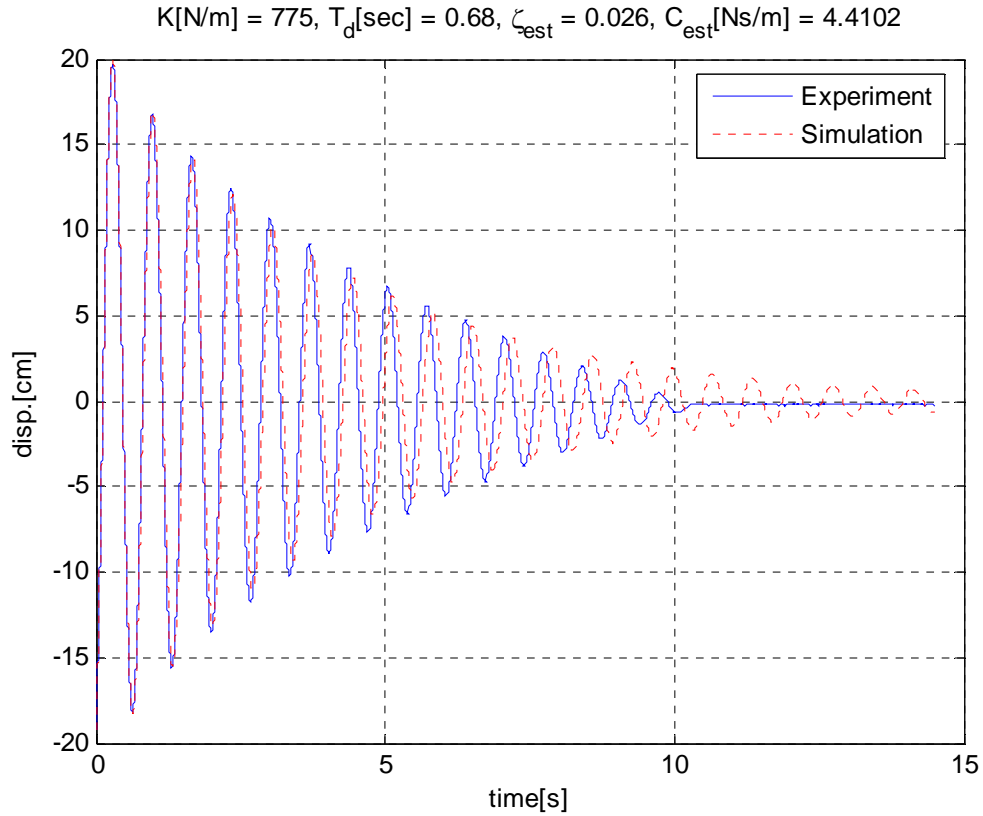


Figure 4-16. Comparison between free decay test and simulation

As shown in Figure 4-16, linear damping model is good for first 11 peaks but makes error when oscillating amplitude becomes small. Finally,  $f$  is given by Eq. (4-9).

$$f(\dot{y}) = 0.2683\dot{y}^3 - 2.6265\dot{y}^2 + (10.3846 + 4.33)\dot{y} + 8.1392, \dot{y} > 0, \quad (4-9)$$

$$f(\dot{y}) = 0.3625\dot{y}^3 + 2.8255\dot{y}^2 + (10.3216 + 4.33)\dot{y} - 7.5587, \dot{y} < 0.$$

### 4.3.2. Validation of Nonlinear Static Damping Model

To verify the estimated damping model, extensive experiments are performed and compared with simulation results with the damping model found in the previous section. In each experiment, the motor generated sinusoidal force together with the spring force whose stiffness was 1000N/m. 17 forcing frequencies were considered and for each forcing frequency, 2 to 14 amplitude values were applied. Input force particulars are summarized in Table 4-6.

Table 4-6. Input force particulars

Forcing Frequency	Amplitude													
0.5Hz	10N	15N												
0.6Hz	10N	15N												
0.7Hz	10N	15N												
0.8Hz	10N	15N	20N	25N	30N	40N	50N	60N	70N	80N	90N	100N	110N	120N
0.9Hz	10N	15N	20N	25N	30N	40N	50N	60N	70N	80N	90N	100N	110N	115N
1.0Hz	10N	15N	20N	25N	30N	40N	50N	60N	100N					
1.1Hz	10N	15N	20N	30N	40N	50N	60N	70N	80N					
1.2Hz	10N	15N	20N	25N	30N	35N	40N	50N	60N					
1.3Hz	10N	15N	20N	25N	30N	40N	50N							
1.35Hz	10N	15N	20N	25N	30N	40N								
1.4Hz	10N	15N	20N	25N	30N	35N								
1.45Hz	10N	15N	20N											
1.5Hz	10N	15N	20N											
1.55Hz	10N	15N												
1.6Hz	10N	15N												
1.65Hz	10N	15N	20N											
1.7Hz	10N	15N	20N											

The motor driving force was applied for two minutes. To eliminate transient effects due to initial conditions, only the data of the last 40 seconds of each run were used for system identification. Simulation model used for validation is shown in Figure 4-17.

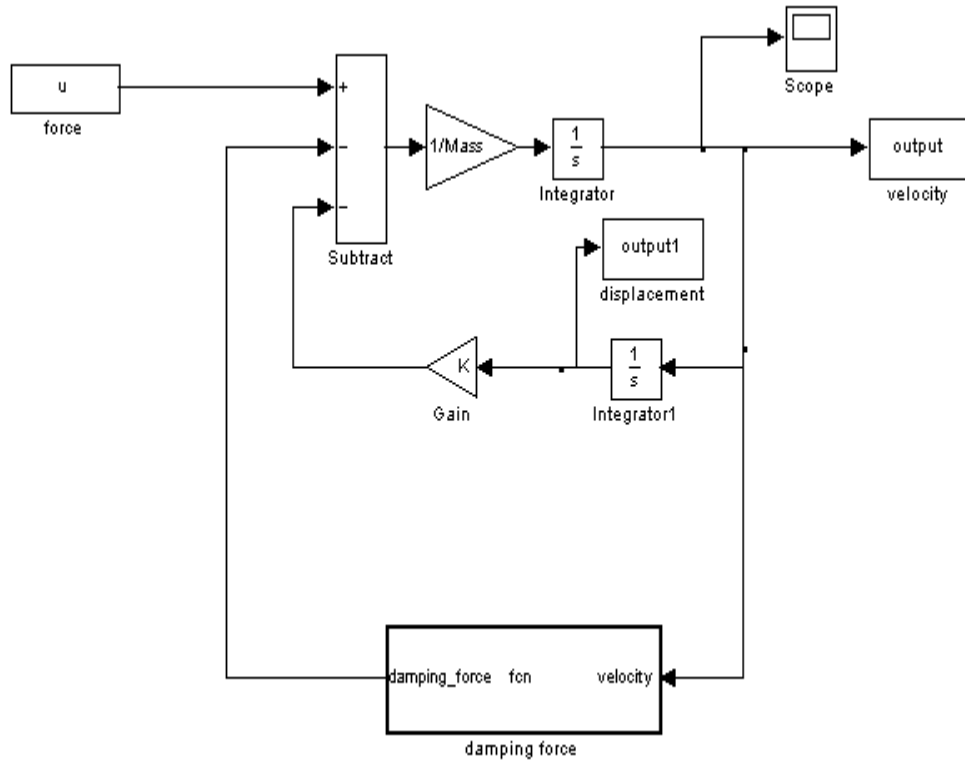


Figure 4-17. Simulation model for validation of damping model

Table 4-7 Comparison between experiment and simulation

	0.8Hz	0.9Hz	1.0Hz	1.1Hz	1.2Hz	1.3Hz	1.35Hz	1.4Hz	1.45Hz	1.5Hz	1.55Hz	1.6Hz	1.65Hz	1.7Hz
10N	Red	Red	Red	Red	Red	Red	Red	Blue	Blue	Blue	Red	Red	Red	Red
15N	Red	Red	Red	Red	Red	Blue	Blue	Blue	Blue	Red	Red	Red	Red	Red
20N	Blue	Blue	Blue	Blue	Blue	Blue	Blue	Blue	Blue	Red	White	White	White	Red
25N	Blue	Blue	Blue	White	Blue	Blue	Blue	Blue	Blue	White	White	White	White	White
30N	Blue	Blue	Blue	Blue	Blue	Blue	Blue	Blue	White	White	White	White	White	White
35N	White	White	Blue	White	Blue	White	White	Blue	White	White	White	White	White	White
40N	Blue	Blue	Blue	Blue	Blue	Blue	Blue	White	White	White	White	White	White	White
50N	Blue	Blue	Blue	Blue	Blue	Blue	White	White	White	White	White	White	White	White
60N	Blue	Blue	Blue	Blue	Blue	White	White	White	White	White	White	White	White	White
70N	Blue	Blue	White	Blue	White	White	White	White	White	White	White	White	White	White
80N	Blue	Blue	White	Blue	White	White	White	White	White	White	White	White	White	White
90N	Blue	Blue	White	White	White	White	White	White	White	White	White	White	White	White
100N	Blue	Blue	Blue	White	White	White	White	White	White	White	White	White	White	White
110N	Blue	Blue	White	White	White	White	White	White	White	White	White	White	White	White
115N	White	Blue	White	White	White	White	White	White	White	White	White	White	White	White
120N	Blue	White	White	White	White	White	White	White	White	White	White	White	White	White

Experiments not performed	Good agreement $\max\left(\frac{y_{\text{experiment}} - y_{\text{simulation}}}{y_{\text{experiment}}}\right) < 0.1$	Poor agreement $\max\left(\frac{y_{\text{experiment}} - y_{\text{simulation}}}{y_{\text{experiment}}}\right) > 0.1$
---------------------------	--	--

As shown in Table 4-7, poor agreement between experiment and simulation occurs when forcing amplitude is small. Poor agreement is observed in cases of 30N of forcing amplitude at 1.5Hz and 1.7Hz, too. Some representative results of poor and good agreement are shown in Figure 4-18 through Figure 4-23 and Figure 4-24 through Figure 4-26, respectively.

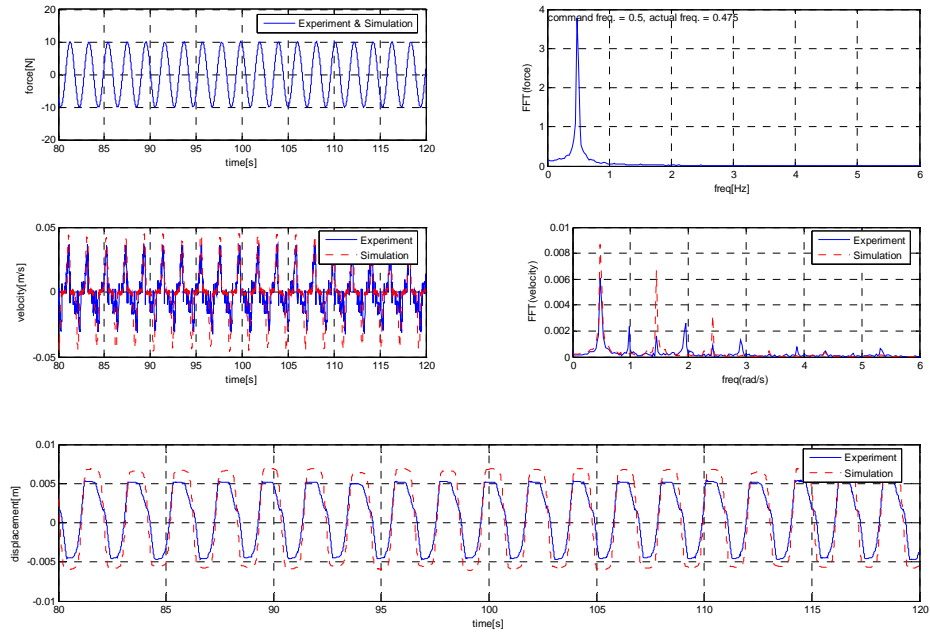


Figure 4-18. Comparison between experiment and simulation - forcing amplitude = 10N, forcing frequency = 0.5Hz

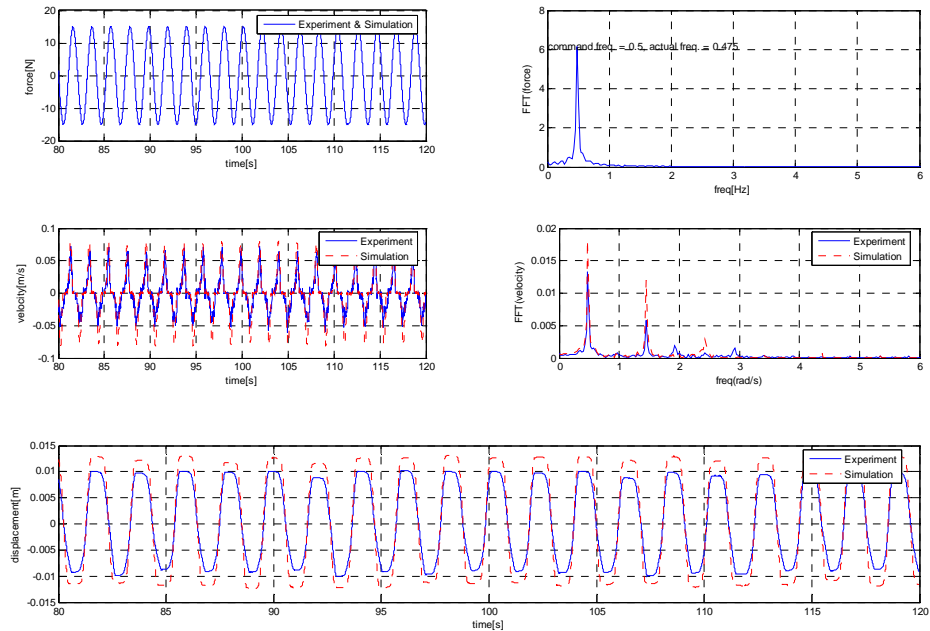


Figure 4-19. Comparison between experiment and simulation - forcing amplitude = 15N, forcing frequency = 0.5Hz

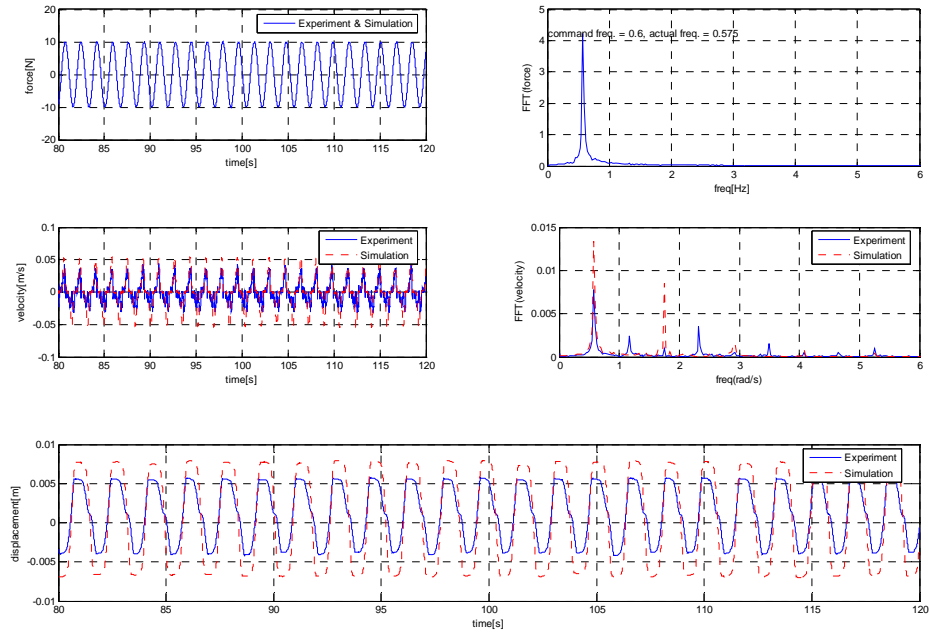


Figure 4-20. Comparison between experiment and simulation - forcing amplitude = 10N, forcing frequency = 0.6Hz

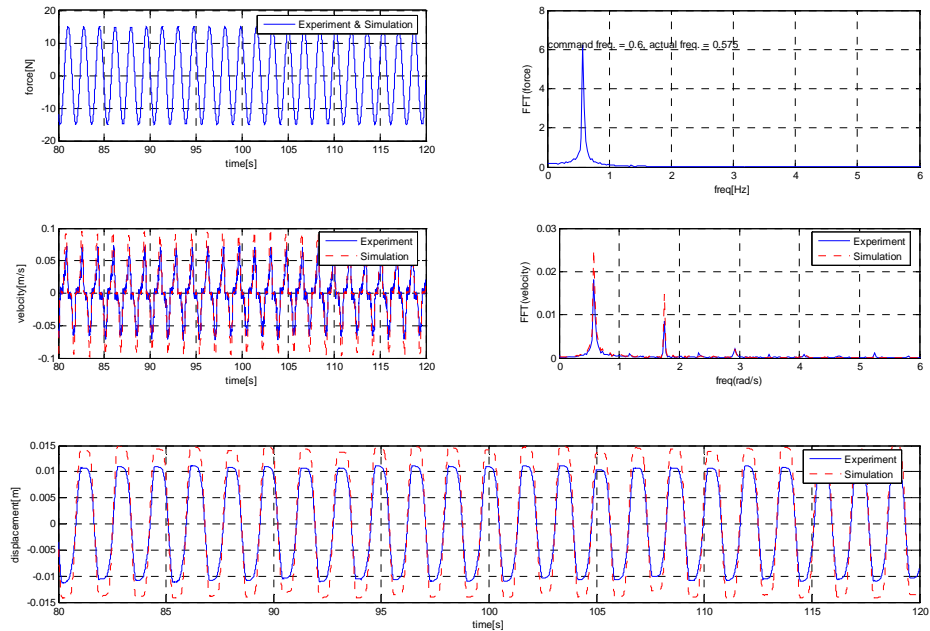


Figure 4-21. Comparison between experiment and simulation - forcing amplitude = 15N, forcing frequency = 0.6Hz

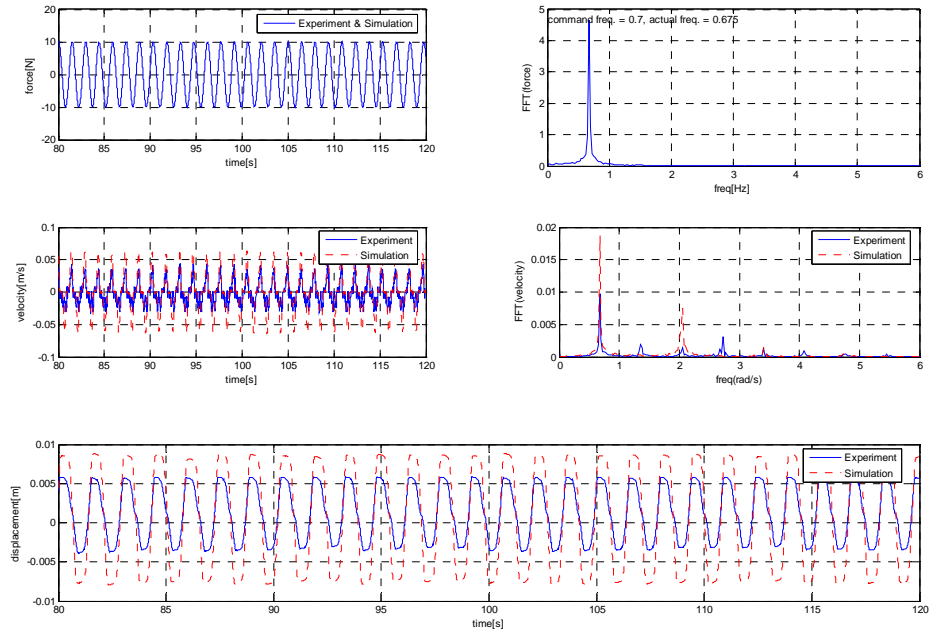


Figure 4-22. Comparison between experiment and simulation - forcing amplitude = 10N, forcing frequency = 0.7Hz

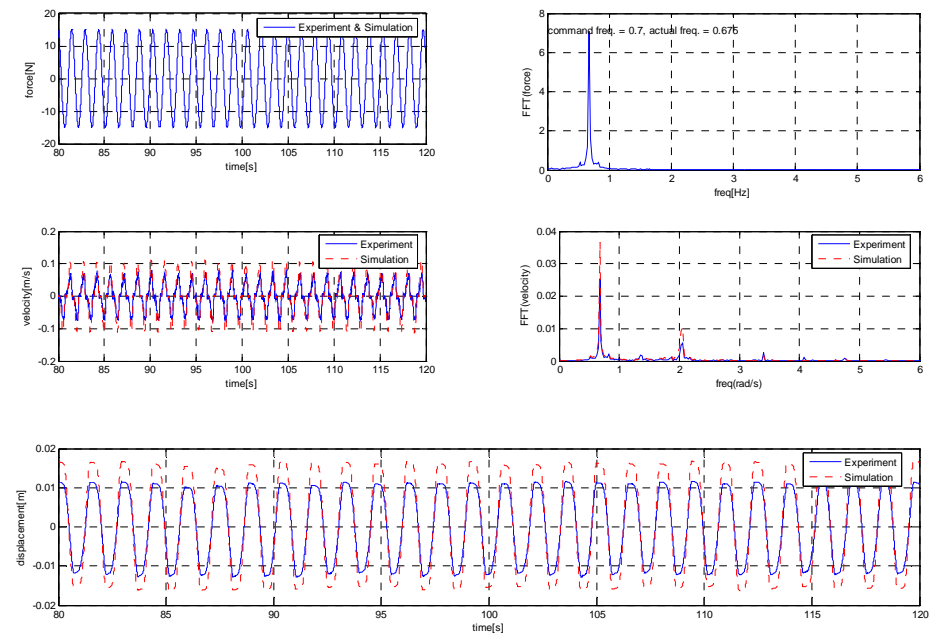


Figure 4-23. Comparison between experiment and simulation - forcing amplitude = 15N, forcing frequency = 0.7Hz



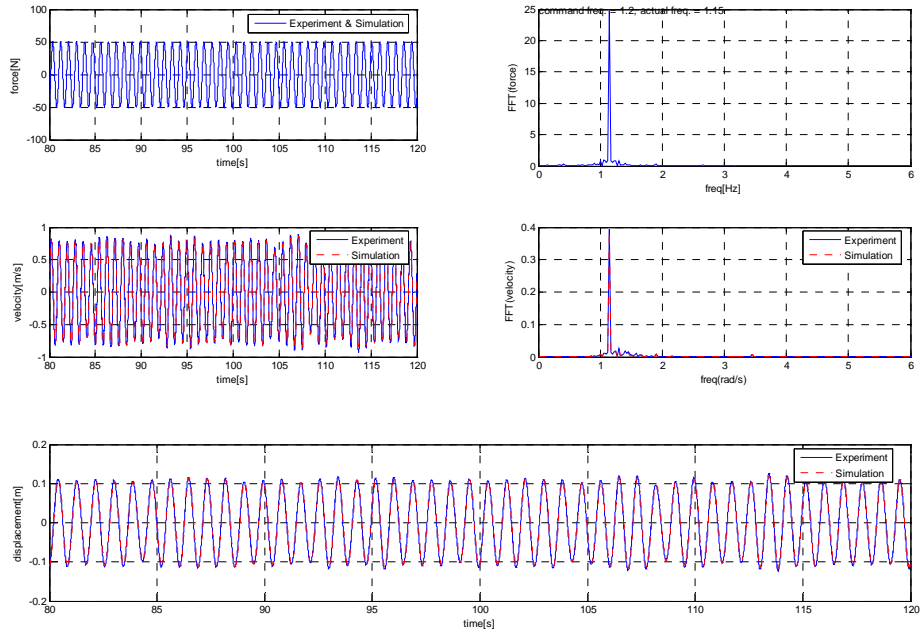


Figure 4-24. Comparison between experiment and simulation - forcing amplitude = 50N, forcing frequency = 1.2Hz

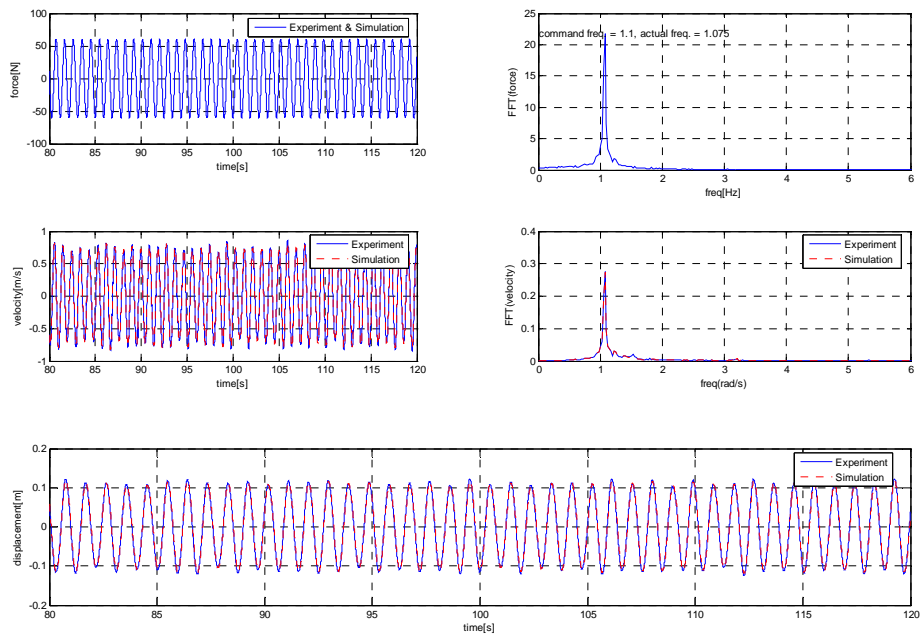


Figure 4-25. Comparison between experiment and simulation - forcing amplitude = 60N, forcing frequency = 1.1Hz

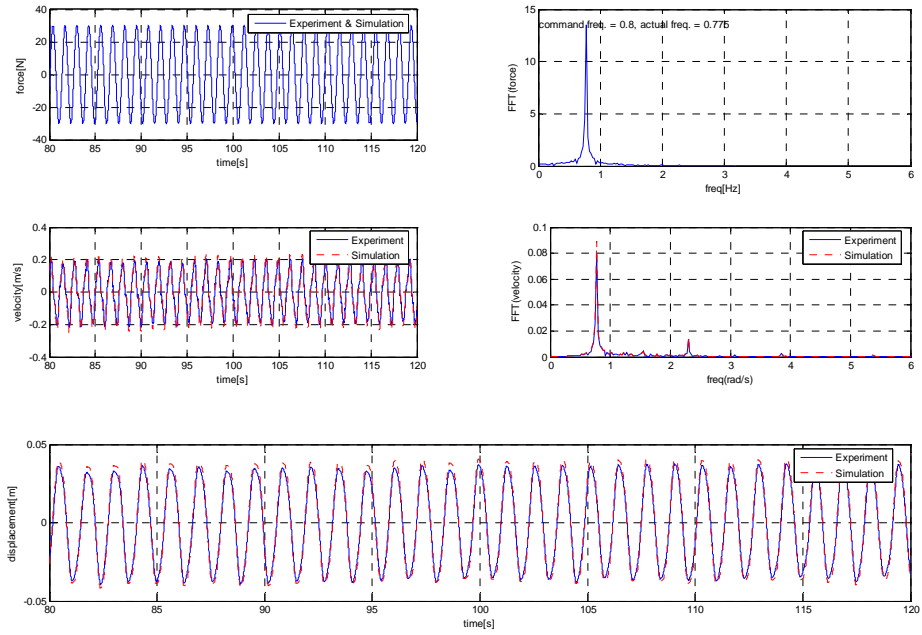


Figure 4-26. Comparison between experiment and simulation - forcing amplitude = 30N, forcing frequency = 0.8Hz

### 4.3.3. Controller Design and Validation by VIV Experiments

#### 4.3.3.1. Controller Design

By utilizing the estimated damping model  $f(\dot{y})$  in Eq. (4-9), a controller is designed in Eq. (4-10).

$$F_{motor} = f(\dot{y}) - c_{virtual}\dot{y} - k_{virtual}y, \quad (4-10)$$

where  $c_{virtual}$  and  $k_{virtual}$  are programmable damping coefficient and spring constant respectively. Sampling time for the controller is 5 ms. Generated force by Eq. (4-10) results in practically linear m-c-k system.

#### 4.3.3.1. Validation of the Designed Controller by VIV Experiments

The equation of motion for the  $V_{CK}$  VIVACE model undergoing VIV after compensating damping force of the system is given as:

$$m\ddot{y} + c_{virtual}\dot{y} + k_{virtual}y = f_{fluid}(t). \quad (4-11)$$

The designed controller in (4-10) is validated by comparing the amplitudes of cylinder undergoing VIV with the  $V_{CK}$  VIVACE model to those with real springs. To compare the amplitudes of the cylinder in VIV, inertial mass, damping coefficient and spring constant of both systems should be as close as possible. Since inertial mass of the  $V_{CK}$  VIVACE

model is larger than that of the VIVACE model with real springs by  $m_{eff}$  which is estimated in Table 3-4, 2.0 kg of weight is added to the VIVACE model with real springs.  $c_{virtual}$  is set to the same as  $c_{bearing}$  which is estimated as 4.4 Ns/m in Section 4.3.1. Finally,  $k_{virtual}$  of the V<sub>CK</sub> VIVACE model is programmed to be the same as that of real springs. In order to estimate spring constant  $k$  of real springs, free decay tests were performed 10 times and Eq. (3-9) was used for each result of free decay tests. Results of free decay tests are summarized in Table 4-8.

Table 4-8. Results of free decay tests to identify real spring constants  $k$

Test No	1	2	3	4	5
$k$	766.05	766.05	757.96	734.46	742.17
Test No.	6	7	8	9	10
$k$	750.01	750.01	786.84	774.26	755.79
Avg.	755.79		Std.	16.02	

Figure 4-27 shows comparison of amplitude ratio ( $A/D$ ) with the VIVACE model with real springs to that with the V<sub>CK</sub> VIVACE model.

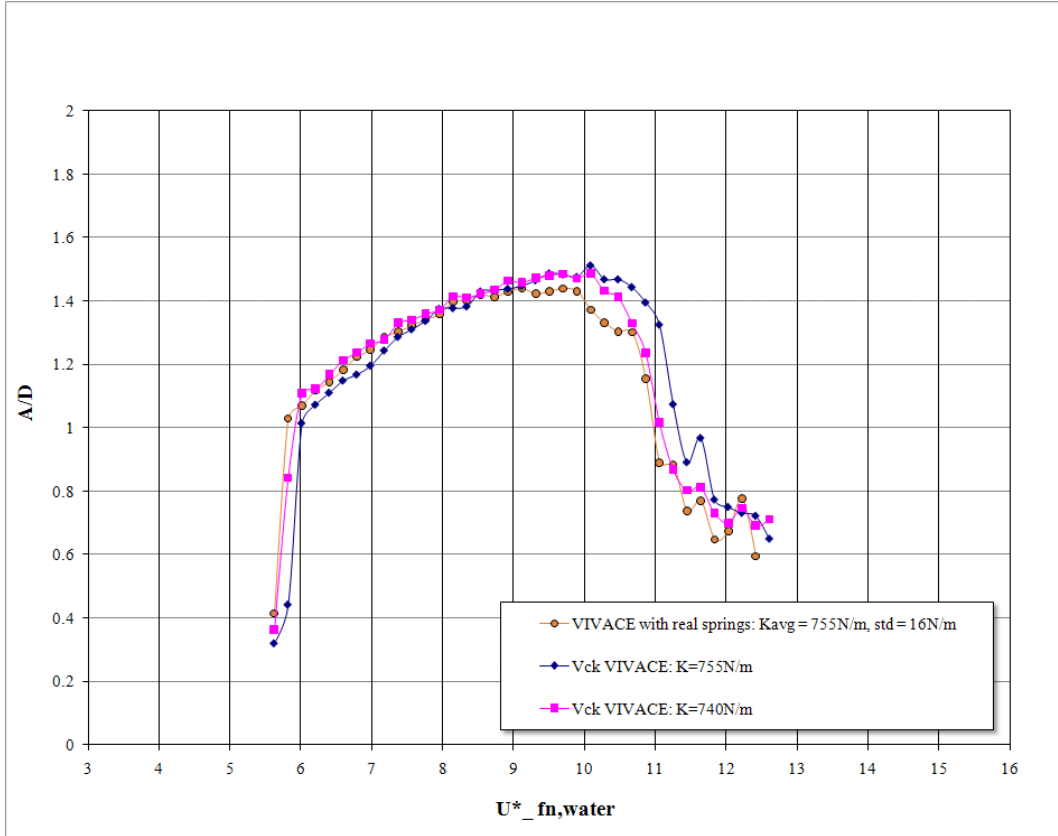


Figure 4-27. Comparison of  $A/D$  with the VIVACE model with real springs to that with the  $V_{CK}$  VIVACE model with NS damping model

As shown in Figure 4-27,  $A/D$  graph with  $k_{virtual} = 755 \text{ N/m}$  is slight shifted to right compared with that obtained with the VIVACE model with real springs. However,  $A/D$  graphs of the  $V_{CK}$  VIVACE model with  $k_{virtual} = 740 \text{ N/m}$  which is within the 1 standard deviation shows good agreement with that of the VIVACE model with real springs. Hence, we can conclude the designed virtual damper/spring system with the nonlinear static damping model proposed in this section produces good performance in VIV experiments. However, there still remains room for improvement in the velocity regime where the static friction dominates based on the validation results of the system identification.

## CHAPTER 5.

### IDENTIFICATION OF NONLINEAR DYNAMIC DAMPING MODEL AND CONTROLLER DESIGN

As shown in section 4.3.2, nonlinear static damping model does not yield good performance when amplitude of velocity is too small due to static friction effect. Thus, we need nonlinear dynamic damping model to take static friction into account.

#### 5.1. Dynamic Damping Model Identification

##### 5.1.1. Damping Force Calculation using $y$ and $dy/dt$

To select a proper structure of the dynamic damping model, we need to investigate the relationship between  $\dot{y}$  and  $f$ . However, since only  $y$  and  $\dot{y}$  are measured from the V<sub>CK</sub> VIVACE apparatus, we need to evaluate  $f$  using measured  $y$  and  $\dot{y}$ . From Eq. (2-9) the equation of motion of V<sub>CK</sub> VIVACE apparatus is given in Eq. (5-1) when the motor produces monochromatic sinusoidal force with amplitude  $A$  and frequency  $\Omega$  together with spring force with stiffness  $k$ .

$$m\ddot{y} = F_{motor} - f = A\cos(\Omega t + \varphi) - ky - f. \quad (5-1)$$

Then damping force  $f$  can be expressed as:

$$f = A\cos(\Omega t + \varphi) - m\ddot{y} - ky. \quad (5-2)$$

One way to estimate  $\ddot{y}$  is to differentiate  $\dot{y}$  numerically. However, it is well known that numerical differentiation amplifies high frequency noise, which makes result of system identification unreliable. Thus, we need to design a low-pass filter to rule out the noise caused by the numerical differentiation. To design a proper low-pass filter, frequency response of  $\dot{y}$  and  $d\dot{y}/dt$  for various  $A$  and  $\Omega$  are investigated. Figure 5-1 shows a typical frequency response of numerically differentiated  $\dot{y}$ .

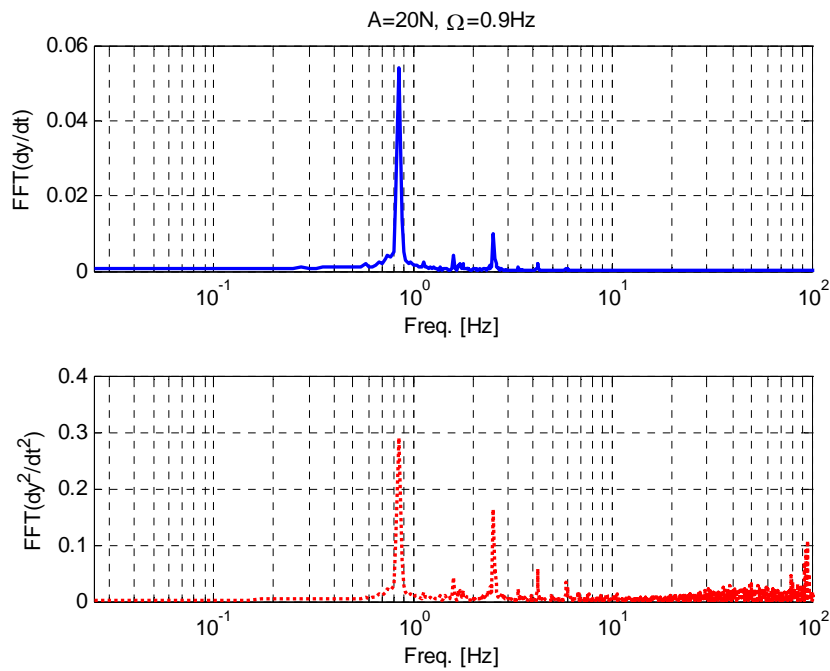


Figure 5-1. Frequency response of  $\dot{y}$  and  $\ddot{y}$  for  $A = 20\text{N}$  and  $\Omega = 0.9\text{ Hz}$

As seen from Figure 5-1, numerical differentiation amplifies noise around 100 Hz. To attenuate noise around that frequency region, the low-pass filter in Eq. (5-3) is used and both filtered and unfiltered  $\ddot{y}$  of a selected result are compared in Figure 5-2.

$$\mathbf{G}_{LF}(s) = \frac{900^3}{(s + 900)^3}. \quad (5-3)$$

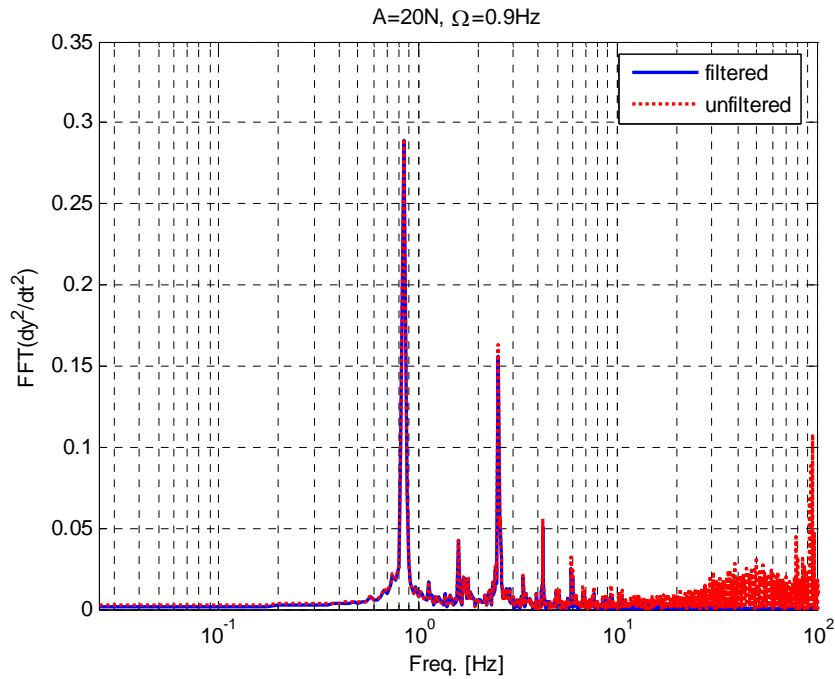


Figure 5-2. Comparison between filtered and unfiltered  $\ddot{y}$  for  $A = 20\text{N}$  and  $\Omega = 0.9\text{ Hz}$

It is shown from Figure 5-2 that the designed low-pass filter sufficiently rules out noise at high frequency region without affecting much to signals we need. Finally, the damping force  $f(y, \dot{y}, \ddot{y})$  that will be used as the output for system identification is given as:



$$f(y, \dot{y}, \ddot{y}) = \mathbf{L}^{-1}[\mathbf{G}_{LF}(s) \cdot \mathbf{L}[A\cos(\Omega t + \varphi) - m\ddot{y} - ky]], \quad (5-4)$$

where,  $\mathbf{L}[\cdot]$  is Laplace transform and  $\mathbf{L}^{-1}[\cdot]$  is inverse Laplace transform. respectively.

### 5.1.2. Validation of Calculated $f$

Damping force  $f(y, \dot{y}, \ddot{y})$  in Eq. (5-4) is validated by comparing it with simulated damping force from Eq. (4-9) which is nonlinear static damping model found in Section 4.3.1. Since Eq. (4-9) turned out to be accurate except when amplitude of velocity of oscillation is small, accuracy of Eq. (5-4) can be guaranteed if damping forces from Eq. (4-9) and Eq. (5-4) agree well with each other in the middle and high velocity region. Selective time histories of displacement, damping force and frequency response from both simulation and experimental data are shown in Figure 5-3 through Figure 5-5. As seen from the graphs, calculated  $f$  using Eq. (5-4) show very good agreements with the generated damping force with Eq. (4-9) even though slight phase lag exists in the filtered signals.

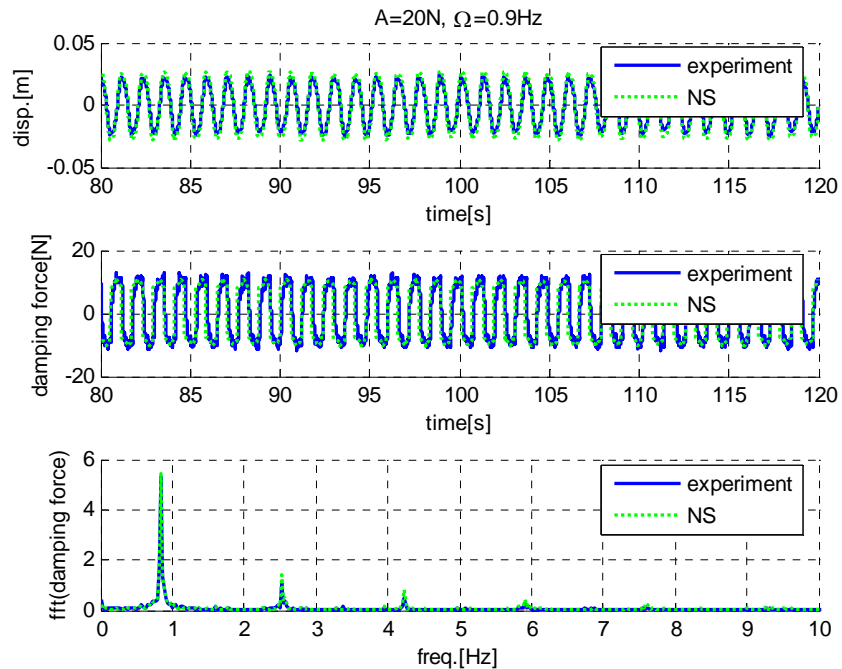


Figure 5-3. Comparison of displacement, damping force and frequency response between simulation and experimental results for  $A = 20N$  and  $\Omega = 0.9 Hz$

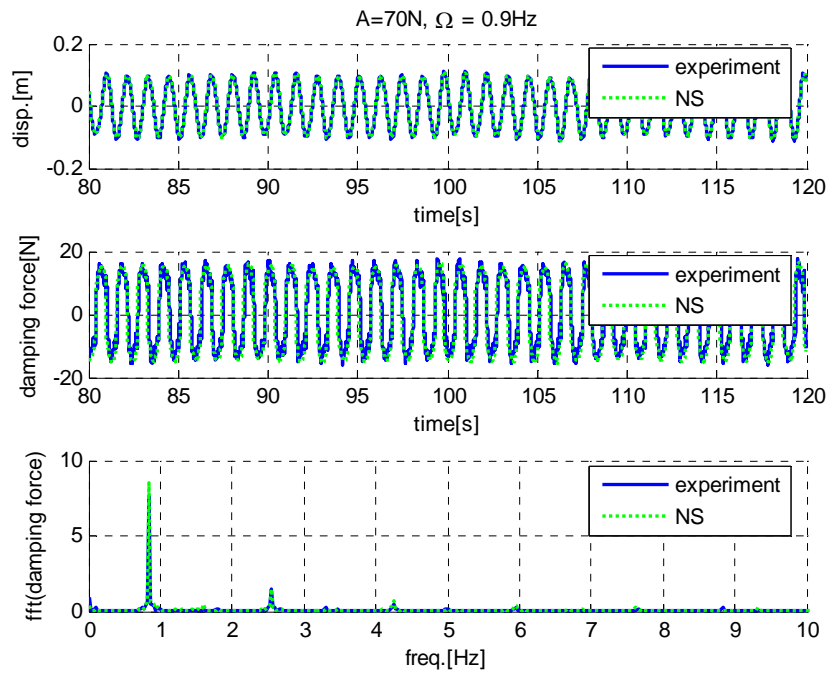


Figure 5-4. Comparison of displacement, damping force and frequency response between simulation and experimental results for  $A = 70\text{N}$  and  $\Omega = 0.9\text{ Hz}$

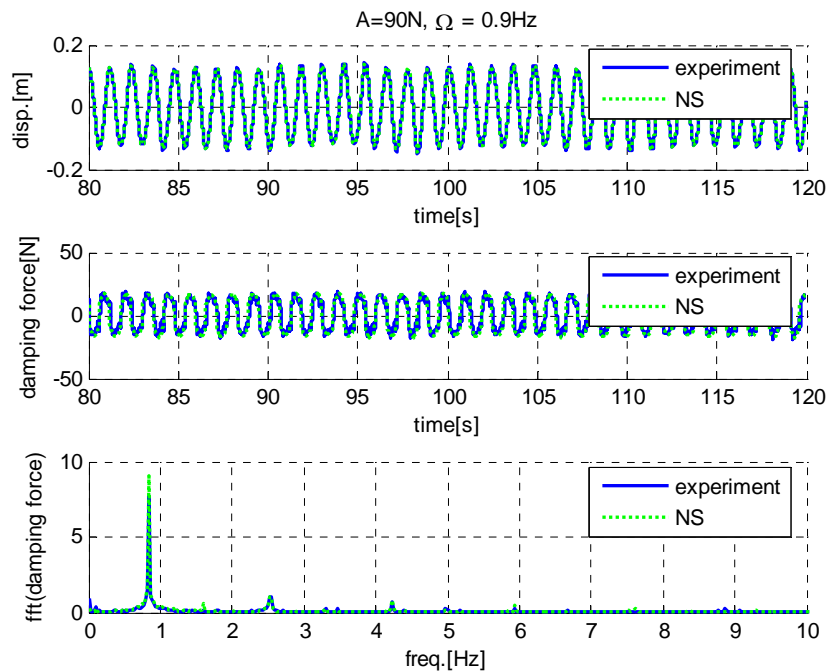


Figure 5-5. Comparison of displacement, damping force and frequency response between simulation and experimental results for  $A = 90\text{N}$  and  $\Omega = 0.9\text{ Hz}$

### 5.1.3. Autoregressive Friction Modeling in the Velocity Dead Zone

Figure 5-6 shows an experimental result of calculated damping force using Eq. (5-4) in low velocity regime. We can see a hysteresis caused by friction which cannot be modeled with nonlinear static damping models.

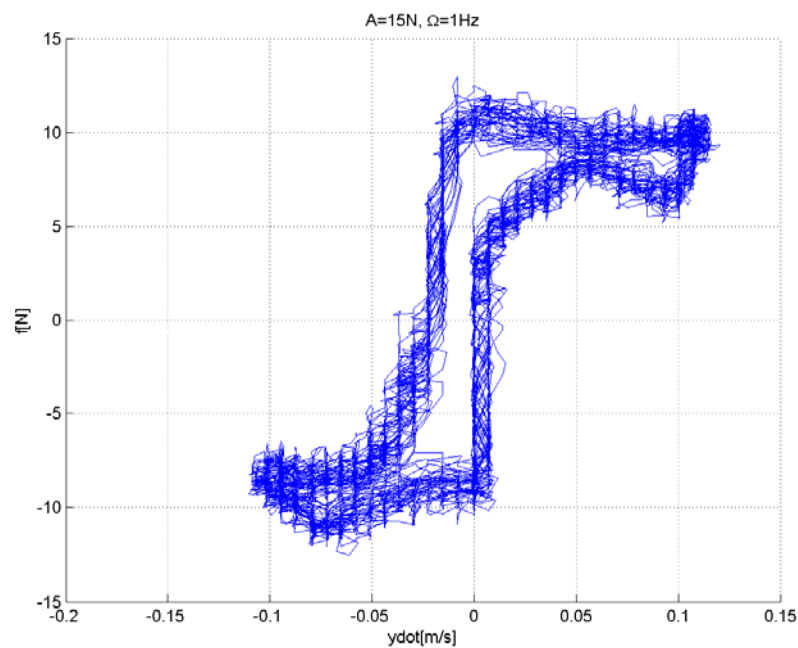


Figure 5-6.  $f$  vs.  $\dot{y}$  for  $A = 15$ N and  $\Omega = 1$  Hz

The nonlinearity of the static characteristic depicting the dependence of friction on velocity causes the model to fail to predict the friction time series when velocity is in the vicinity of zero. This deficiency is prominent in the range of friction values that corresponds to near-zero velocity is defined as the dead zone. In the dead zone the velocity-friction characteristic cannot be inverted to be used for the prediction of the friction force. In this respect, the following ‘complementary’ model named LARNOS

(Linear Autoregression combined with NONlinear Static model) is introduced. The LARNOS model combines the nonlinear static model that is valid outside a certain vicinity of zero. In specific the full friction model is of the following form.

$$f_n = u_{STEP}(|\dot{y}_n| - v_{thres}) \cdot \Psi(\dot{y}_n) + u_{STEP}(v_{thres} - |\dot{y}_n|) \cdot \sum_{k=1}^N a_k f_{n-k}. \quad (5-5)$$

In the above  $u_{STEP}(\cdot)$  stands for the unit Heaviside step function and the indices  $n$  and  $(n - k)$  are samples with respect to time of the friction force,  $f$ , and cylinder velocity,  $v$ , signals. The threshold velocity,  $v_{thres}$ , is a positive model constant adjusting the size of the zero velocity vicinity within which the LAR model is active. The LAR model is defined by its order  $N$  and the weight value set,  $v_{thres}$ ,  $k = 1, \dots, N$ . Finally,  $\Psi(\cdot)$  is a symbolic representation of the nonlinear static dependence of the friction force upon the current velocity value.

A more sophisticated transition from the LAR to the static model and vice versa, rather than the stepwise one employed, could have been used and will be investigated in the future. As seen in the formula above, the LAR term of the friction force continuously tracks the signal's dynamics and keeps driving the prediction when velocity lies in the dead zone.

The LAR term needs to be checked for stability so that (a) the friction signal eventually gets to zero when the cylinder is brought to a halt; (b) the friction signal does not diverge

when driven by its initial condition. Stability of the LAR term is guaranteed by verifying that all of its poles, i.e. the roots of the LAR component's characteristic polynomial defined by  $p_c(z^{-1}) = 1 - \sum_{k=1}^N a_k z^{-k}$ , lie in the open unit disk region of the complex plane.

It should be noted here that stability of the LAR term makes it incapable to operate on a standalone basis. Indeed, the linear and asymptotically stable LAR term will eventually go to zero when driven solely by some arbitrary friction initial conditions. In this respect, the static nonlinear function of velocity is the innovation process of the model that makes sure that the friction force does not go to zero as energy is injected in the system, which eventually is manifested as kinetic energy of the oscillating VIVACE cylinder.

The LARNOS model calibration is taking place in three phases:

- a) Calibration of the standalone nonlinear static model (NOS) that has been presented on a physical basis earlier
- b) Calibration of the linear autoregressive component (LAR)
- c) Calibration of the switch-over from submodel to submodel; since the changeover will be stepwise the only parameter to calibrate is the velocity threshold at which it actually occurs.

For (b) the Least Square Error (LSE) estimation method can be straightforwardly employed. Specifically, the NOS model component is omitted from the friction force estimation formula yielding the following.

$$\hat{f}_n = \sum_{k=1}^N a_k f_{n-k} = a_1 f_{n-1} + a_2 f_{n-2} + \dots + a_N f_{n-N}. \quad (5-6)$$

Taking advantage of the  $M$  values of friction force calculated directly from the experimental data series as well as  $N$  initial conditions for the model the model coefficients were calculated in order to minimize the cumulative square error of autoregressive friction force estimation as follows.

$$\hat{E}(a_1, a_2, \dots, a_N) = \hat{E}(\vec{a}) = \sum_{n=0}^{M-1} (f_n - \hat{f}_n)^2, \quad (5-7)$$

$$\vec{a} = [a_1, a_2, \dots, a_N]^T.$$

Function  $\hat{E}(\vec{a})$  in the above is a positive definite scalar function of the model coefficient vector  $\vec{a}$ . It can be argued (Ljung 1999) that function  $\hat{E}(\vec{a})$  demonstrates a minimum at this value of  $\vec{a} = \vec{a}_{OPT}$  for which the following condition holds.

$$\nabla \hat{E} \Big|_{\vec{a}=\vec{a}_{OPT}} = 0 \Leftrightarrow \frac{\partial \hat{E}}{\partial a_q} \Big|_{\vec{a}=\vec{a}_{OPT}} = 0, \forall q = 1, \dots, N. \quad (5-8)$$

Here some manipulation is needed to obtain a final result.

$$\frac{\partial \hat{E}}{\partial a_q} = \frac{\partial}{\partial a_q} \sum_{n=0}^{M-1} (f_n - \hat{f}_n)^2 = \frac{\partial}{\partial a_q} \sum_{n=0}^{M-1} \left( f_n - \sum_{k=1}^N a_k f_{n-k} \right)^2, \quad (5-9)$$

↓

$$\frac{\partial \hat{E}}{\partial a_q} = -2 \sum_{n=0}^{M-1} f_{n-q} \left( f_n - \sum_{k=1}^N a_k f_{n-k} \right), q = 1, \dots, N.$$

In effect, the condition in equation (5-8) is transformed to the following algebraic set of  $N$  linear equations with  $N$  unknowns.

$$\begin{aligned} a_1 \sum_{n=0}^{M-1} f_{n-q} f_{n-1} + a_2 \sum_{n=0}^{M-1} f_{n-q} f_{n-2} + \dots + a_N \sum_{n=0}^{M-1} f_{n-q} f_{n-N} \\ = a_1 \sum_{n=0}^{M-1} f_n f_{n-q}, q = 1, \dots, N. \end{aligned} \quad (5-10)$$

In the algebraic set above, one can observe the cross and autocorrelation terms appearing as coefficients to the unknowns that are the unknown LAR model coefficients. Further simplification is possible based on the assumption that the friction force signal is stationary and ergodic. However, for the sake of brevity these remarks are omitted here and can be sought after in literature (Ljung 1999).

For a given finite temporal window of length  $M$ , a unique solution can be obtained for the LAR model coefficients. Note that if the friction signal structure is that of white (a.k.a. uncorrelated) noise then the coefficients will be all equal to zero because the right-hand side constant terms in equation (5-10) will be equal to zero whilst, on the left-hand side, only the diagonal terms will appear. This mathematically reflects the fact that white noise



samples cannot be estimated by observing past signal samples, since such noise is uncorrelated.

Finally, the value of the estimation's cumulative square error  $\hat{E}(\vec{a} = \vec{a}_{OPT})$  at the optimal coefficient set  $\vec{a}_{OPT}$  provides a measure of the adequacy of the model order  $N$  to yield acceptable estimation of the time series. In case that this error significant nonzero value then one should attempt to increase the model order by at least one and then follow the same procedure to obtain the expanded coefficient set. Alternatively, to test acceptability of the estimation process, one can run equation (5-6) in simulation and then observe on a plot how well estimated friction force  $\hat{f}_n$  tracks the experimentally determined friction force values  $f_n$ .

In this application, dynamic order  $N$  of LAR term is chosen as 4. For convenience,  $f_n$  is normalized using (5-11) before applying the LSE estimation.

$$f_{n(nomalized)} = \frac{f_n - \text{MINF}}{\text{MAXF} - \text{MINF}} = \frac{f_n - (-27.71)}{28.71 - (-27.71)}. \quad (5-11)$$

In the above equation, MAXF and MINF are maximum and minimum values of  $f_n$  respectively. Elements of  $a_{OPT}$  obtained by the LSE estimation are listed in Table 5-1. For the LSE estimation, 22000 data points which are properly selected to cover all tests shown in Table 4-6 are used.

Table 5-1. Estimated elements of  $a_{OPT}$  in LAR model

$a_1$	$a_2$	$a_3$	$a_4$
1.8073	-1.3832	0.5382	0.0333

Figure 5-7 shows the normalized  $f$  and output of LAR model. Achieved  $\hat{E}(\vec{a} = \vec{a}_{OPT})$  is 7.078.

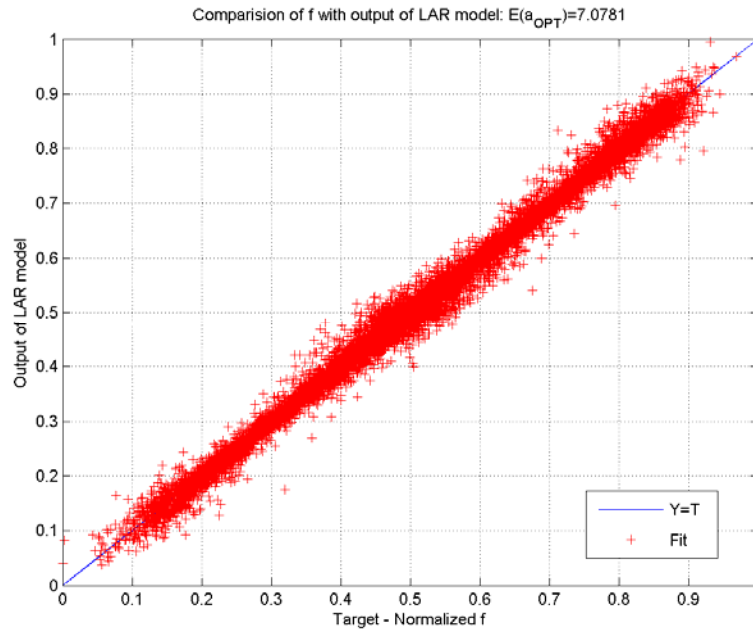


Figure 5-7. Comparison of normalized  $f$  with the output of AR model

Table 5-2 lists roots of characteristic polynomial of the LAR model. As shown in Table 5-2, the stability of the LAR model is verified since absolute values of all roots of  $p_c(z^{-1})$  are smaller than 1.

Table 5-2. Roots of the  $p_C(z^{-1})$  of LAR term

Roots of $p_C(z^{-1})$	0.9945	0.4334+0.6586i	0.4334-0.6586i	-0.0539
------------------------	--------	----------------	----------------	---------

Finally,  $v_{thres}$ , the threshold value of velocity in Eq. (5-5) is determined as 0.001 m/s by tuning process. The selective plots shown in Figure 5-8 to Figure 5-9 provide validation of LARNOS model. From the figures, it is shown that LARNOS model has better performance than the nonlinear static damping model in low range. Also, LARNOS model shows good results in high velocity regime as expected.

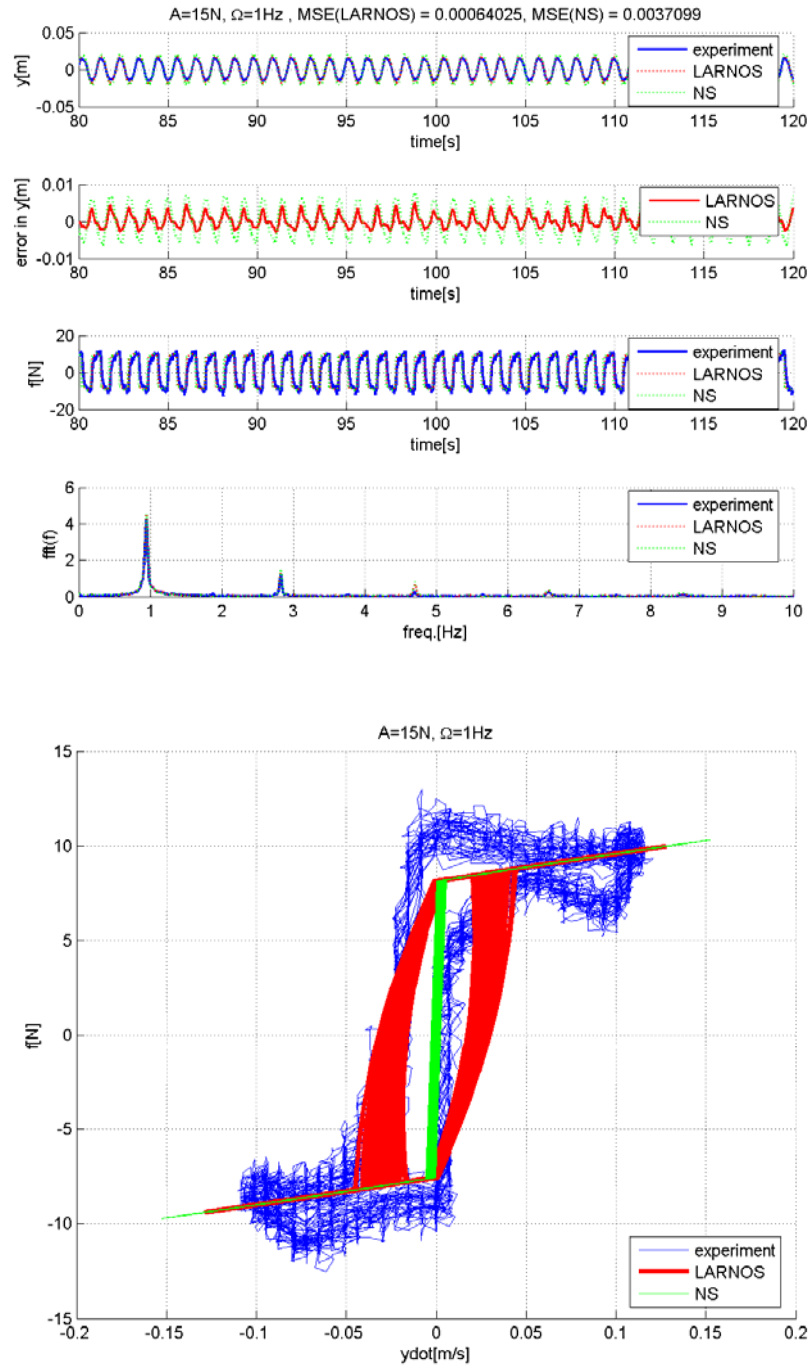


Figure 5-8. Comparison of NS and LARNOS model with experimental result for  $A = 15\text{N}$  and  $\Omega = 1.0\text{ Hz}$

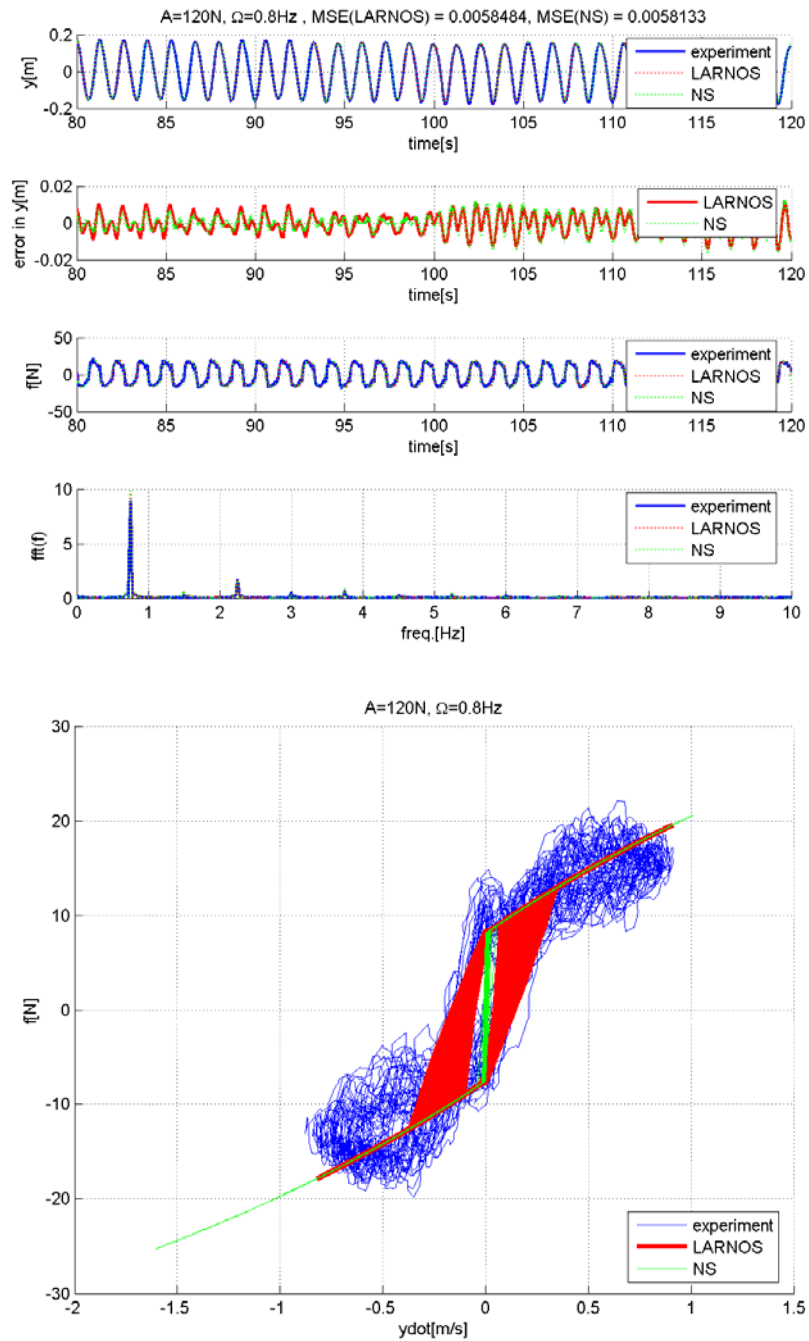


Figure 5-9. Comparison of NS and LARNOS model with experimental result for  $A = 120\text{N}$  and  $\Omega = 0.8\text{ Hz}$

## 5.2. Controller Design and Verification

By utilizing the estimated damping model  $f(\dot{y})$  in Eq. (5-5), a controller is designed in Eq. (5-12).

$$F_{motor} = f - c_{virtual}\dot{y} - k_{virtual}y, \quad (5-12)$$

where  $c_{virtual}$  and  $k_{virtual}$  are programmable damping coefficient and spring constant respectively. Sampling time for the controller is 5 ms. Generated force by Eq. (5-12) results in practically linear m-c-k system.

### 5.2.1. Validation of the Designed Controller by VIV Experiments

The designed controller in Eq. (5-12) is validated with the same way described in Section 4.3.3.1. Figure 5-10 shows amplitude ratio ( $A/D$ ) achieved with the VIVACE model with real springs, the  $V_{CK}$  VIVACE model with NS and LARNOS damping model, respectively. As shown in Figure 5-10, while  $A/D$  graph of the  $V_{CK}$  VIVACE with NS model agrees well with that of that of the VIVACE model with real springs with  $k_{virtual} = 740$  N/m,  $A/D$  graph of the  $V_{CK}$  VIVACE with LARNOS model shows good agreement with that of the VIVACE model with real springs even with estimated real spring stiffness  $k_{virtual} = 755$  N/m itself. Thus, it is verified the  $V_{CK}$  system built with LARNOS model produces better performance than with NS model for VIV experiments as expected. It is also shown that the designed virtual damper/spring system can effectively replace springs and action of generator.

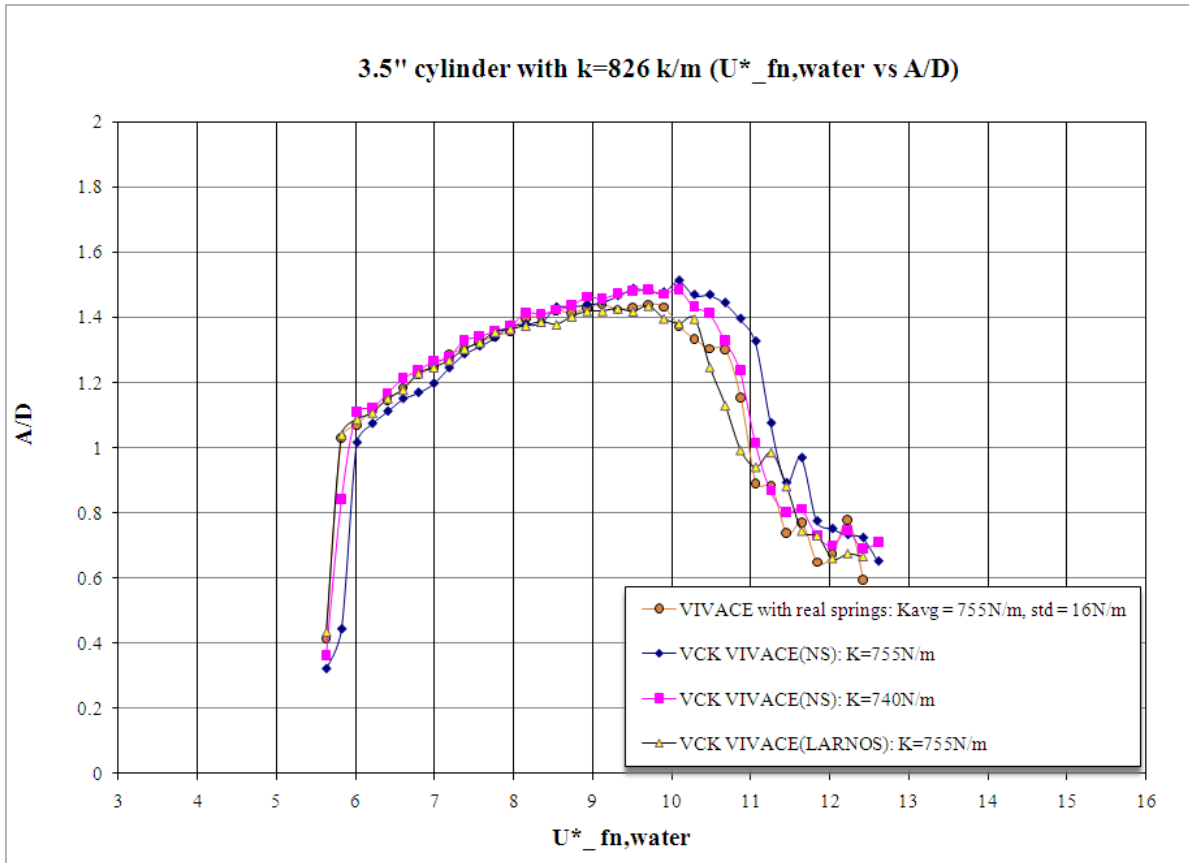


Figure 5-10. Comparison of  $A/D$  with VIVACE model with real springs to that with V<sub>CK</sub> VIVACE model



## **PART B: VIVACE POWER CURVE**

### **CHAPTER 6.**

#### **HIGH DAMPING VIV FOR POWER HARNESSING USING THE VIVACE CONVERTER**

##### **6.1. Experimental Facility**

Experiments on VIV and -harnessing energy using the  $V_{CK}$  VIVACE model are conducted in the Low Turbulence Free Surface Water (LTFSW) Channel at the Marine Hydrodynamics Lab of the UoM. LTFSW Channel is two-story high and recirculates approximately 8,000 gallons of water with maximum velocity of 2m/s. It has a main test section of about 10 ft in length, 1 m in width and 0.8m in depth. During the experiments, water depth is maintained at 71 cm. The measured background turbulence level is less than 0.1% of the free surface velocity, which is acceptable for the experiments (Walker et al. 1996).

## 6.2. Experimental Results for High Damping VIV

Extensive experiments with a 8.89 cm (3.5 in) smooth cylinder were performed varying  $k_{virtual}$  and  $c_{virtual}$  using the  $V_{CK}$  VIVACE model in the LTFSW Channel. The flow velocity was varied from 0.4 m/s to 1.4 m/s. Values of the  $k_{virtual}$  used in the experiments were 400, 600, 800, 1000, 1200, 1400, 1600 and 1800 N/m. For each  $k_{virtual}$ , five virtual  $\zeta_{harn}$  values were used defined as:

$$\zeta_{harn} = \frac{c_{harn}}{2\sqrt{mk_{virtual}}} . \quad (6-1)$$

The  $\zeta_{harn}$  values tested were 0, 0.04, 0.08, 0.12, and 0.16. Total damping of the system is given as:

$$\zeta_{total} = \frac{c_{bearing} + c_{harn}}{2\sqrt{mk_{virtual}}} . \quad (6-2)$$

Amplitude ratios ( $A/D$ ) for each combination of  $k_{virtual}$  and  $\zeta_{harn}$  were found by averaging the highest 10 peak amplitudes. The frequency of oscillation ( $f_{osc}/f_{n,water}$ ) is calculated by an FFT of the entire signal even in the desynchronization range where VIV becomes intermittent.

## 6.2.1. Effect of Damping on VIV

The most significant characteristics of VIV response are the range of synchronization, the amplitude of oscillation  $A/D$ , and the frequency of oscillation ( $f_{osc}/f_{n,water}$ ). The effects of damping on those are presented in the following three subsections.

### 6.2.1.1. Range of Synchronization

Amplitude ratios ( $A/D$ ) versus current velocity ( $U$ ), reduced velocity ( $U^*$ ), and Reynolds number ( $Re$ ) for different values of  $\zeta_{harn}$  for each  $k_{virtual}$  are compiled in Figure 6-1 to Figure 6-8. The following observations can be made:

- (a) For all  $k_{virtual}$  cases, synchronization starts with a jump in  $A/D$  when  $\zeta_{harn}$  is 0. In this case, total system damping only consists of damping from bearings,  $c_{bearing}\dot{y}$ .
- (b) As  $\zeta_{harn}$  increases, the onset of synchronization becomes more gradual.
- (c) With smaller values of  $\zeta_{harn}$ , the upper end of synchronization shifts to higher  $U^*$ .
- (d) Similarly to the onset of synchronization, synchronization ends with a jump in  $A/D$  when  $\zeta_{harn}$  is small. As  $\zeta_{harn}$  increases  $A/D$  curve decreases gradually. As a result, for each  $k_{virtual}$  case, the case that  $\zeta_{harn} = 0$  has the broadest range of synchronization and it becomes narrower as  $\zeta_{harn}$  increases.
- (e) The end of synchronization occurs around  $U^* = 9 - 10$ . At that point, VIV becomes intermittent but remains persistent until  $U^* = 10 - 15$  depending on  $k_{virtual}$  and  $\zeta_{harn}$ .

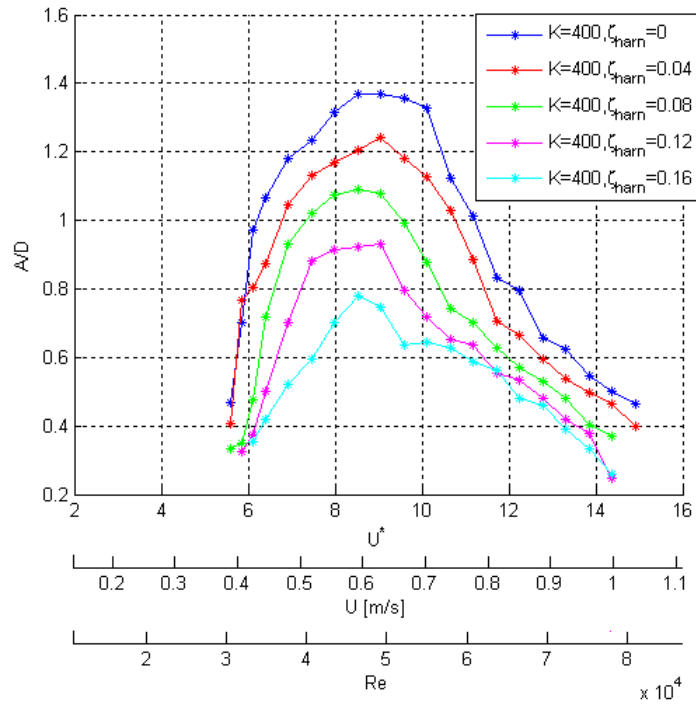


Figure 6-1.  $A/D$  vs.  $U^*$ ,  $U$  and  $Re$  for  $k_{virtual} = 400N/m$  and various values of  $\zeta_{harn}$

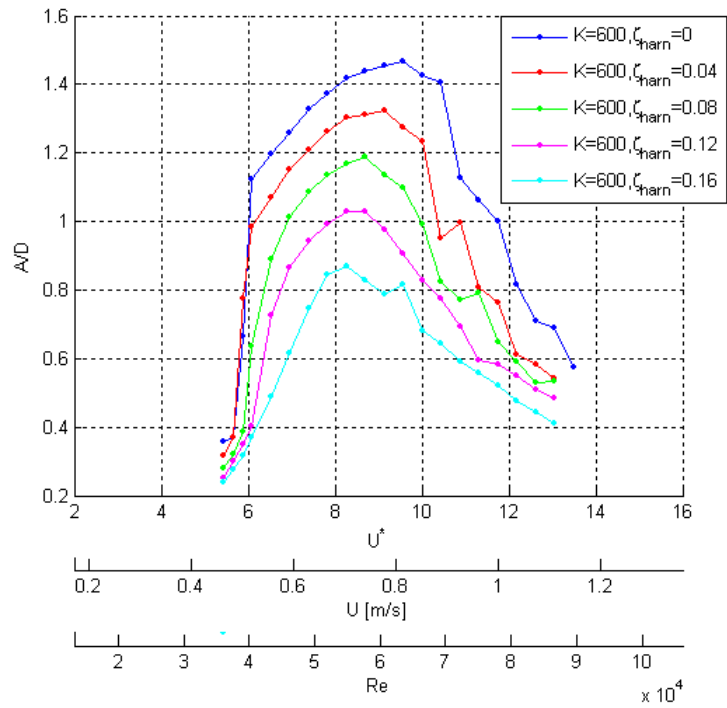


Figure 6-2.  $A/D$  vs.  $U^*$ ,  $U$  and  $Re$  for  $k_{virtual} = 600N/m$  and various values of  $\zeta_{harn}$

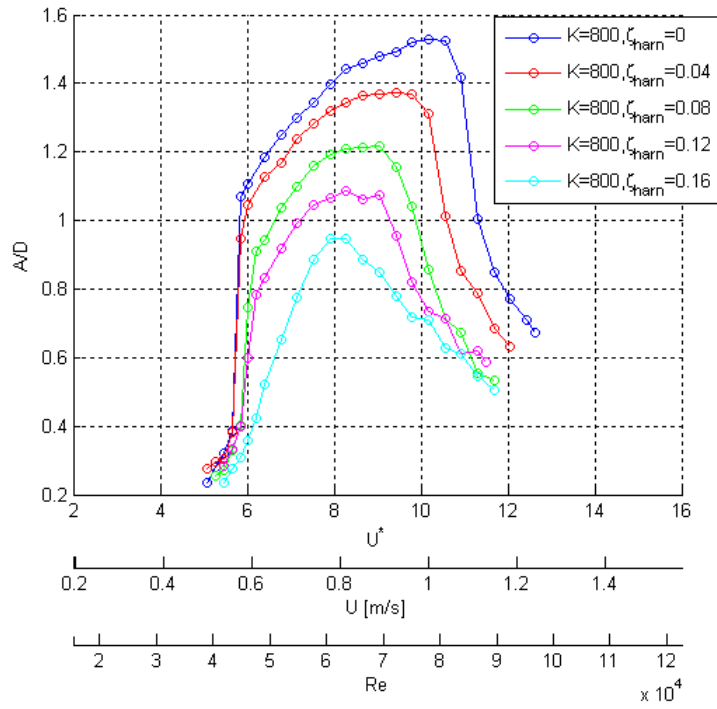


Figure 6-3.  $A/D$  vs.  $U^*$ ,  $U$  and  $Re$  for  $k_{virtual} = 800N/m$  and various values of  $\zeta_{harn}$

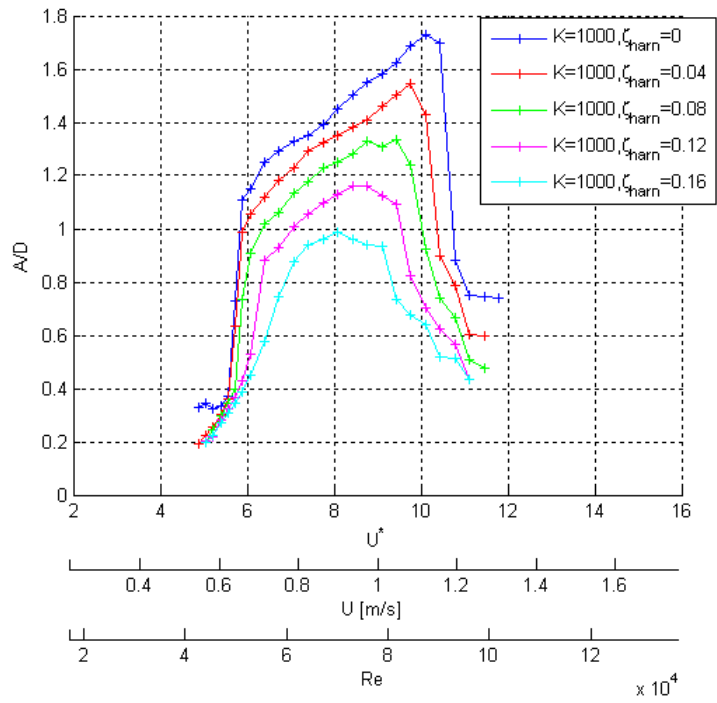


Figure 6-4.  $A/D$  vs.  $U^*$ ,  $U$  and  $Re$  for  $k_{virtual} = 1000N/m$  and various values of  $\zeta_{harn}$

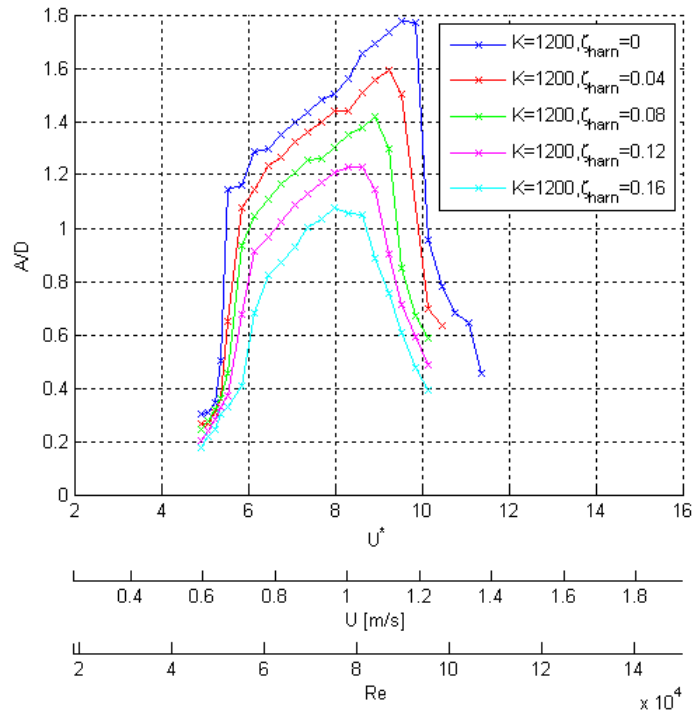


Figure 6-5.  $A/D$  vs.  $U^*$ ,  $U$  and  $Re$  for  $k_{virtual} = 1200N/m$  and various values of  $\zeta_{harn}$

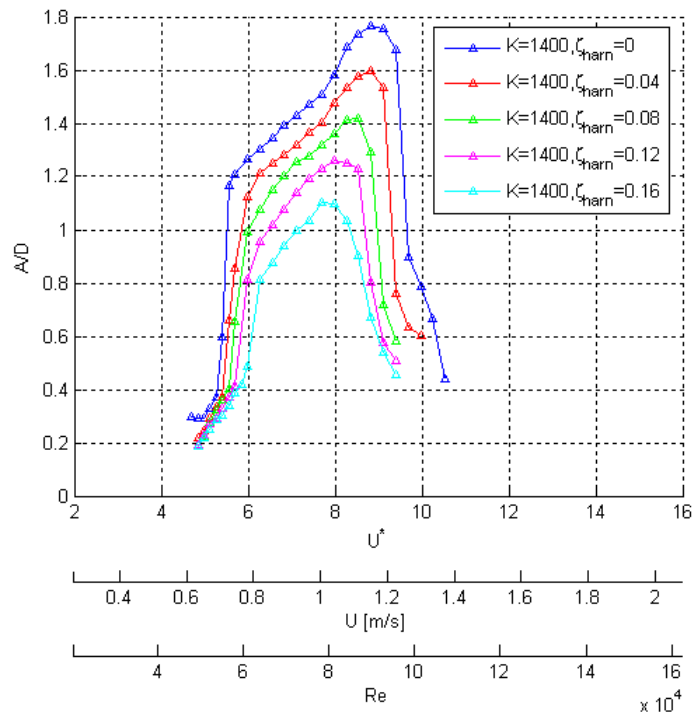


Figure 6-6.  $A/D$  vs.  $U^*$ ,  $U$  and  $Re$  for  $k_{virtual} = 1400N/m$  and various values of  $\zeta_{harn}$

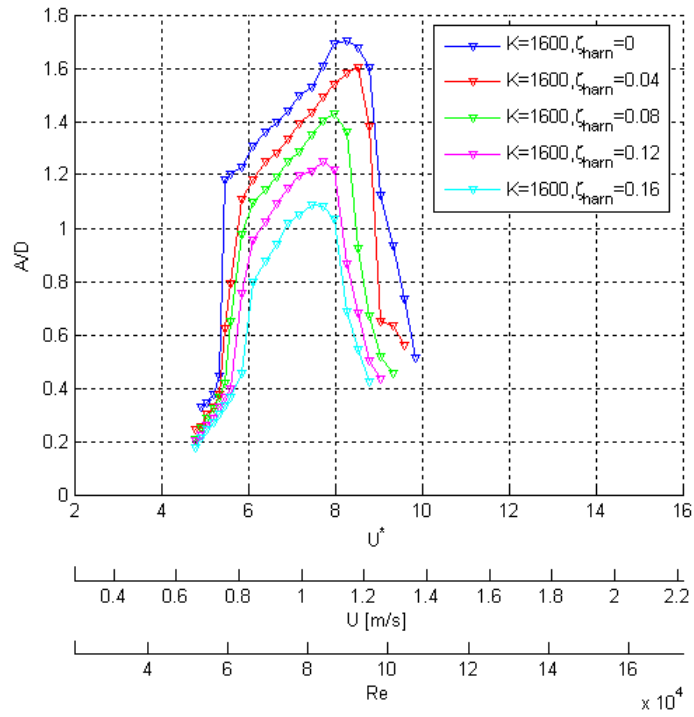


Figure 6-7.  $A/D$  vs.  $U^*$ ,  $U$  and  $Re$  for  $k_{virtual} = 1600N/m$  and various values of  $\zeta_{harn}$

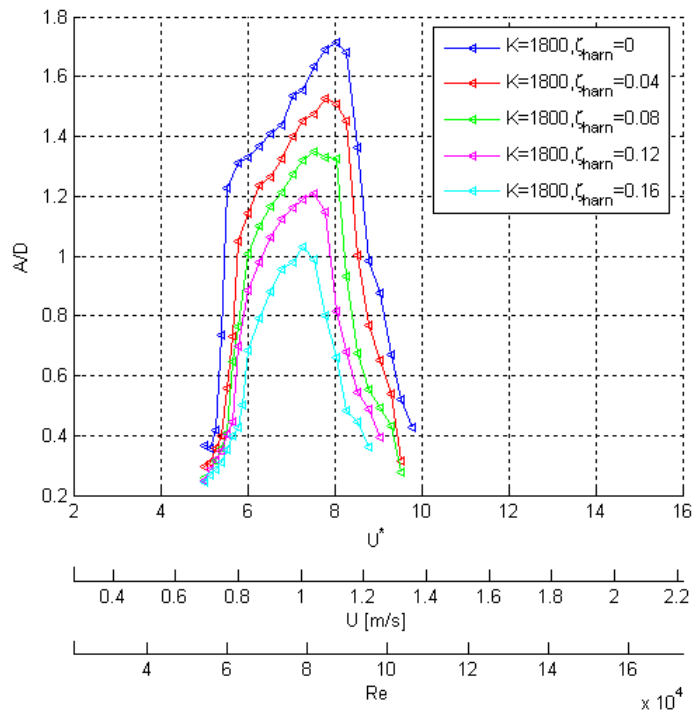


Figure 6-8.  $A/D$  vs.  $U^*$ ,  $U$  and  $Re$  for  $k_{virtual} = 1800N/m$  and various values of  $\zeta_{harn}$

### 6.2.1.2. Amplitude of Oscillation

Based on the same amplitude ratio  $A/D$  graphs in Figure 6-1 to Figure 6-8, the following observations can be made:

- (f) For all cases, it is obvious that the upper branch is not followed by a lower branch; it is followed by desynchronization.
- (g) The upper branch amplitude is not constant. On the contrary,  $A/D$  increases with Reynolds number showing a strong dependence of VIV on Reynolds.
- (h) For all values of  $k_{virtual}$ , the amplitude of oscillation,  $A/D$  is reduced with increasing  $\zeta_{harn}$ . This is expected as the mechanical energy in the VIVACE Converter, which was converted from the hydrokinetic energy of the fluid flow, is dissipated more with higher  $\zeta_{harn}$ . As  $\zeta_{harn}$  increases by 0.04,  $A/D$  reduces by about 0.1 in the middle of the synchronization range, which occurs around  $U^*$  of 7 to 8.
- (i) The maximum values of  $A/D$  for each combination of  $k_{virtual}$  and  $\zeta_{harn}$  are summarized in Table 6-1.



Table 6-1. Maximum amplitude ratio for each combination of  $k_{virtual}$  and  $\zeta_{harn}$

$\zeta_{harn}$	$k_{virtual} = 400$ N/m			$k_{virtual} = 600$ N/m			$k_{virtual} = 800$ N/m			$k_{virtual} = 1000$ N/m		
	$\zeta_{total}$	U[m/s]	Max. A/D	$\zeta_{total}$	U[m/s]	Max. A/D	$\zeta_{total}$	U[m/s]	Max. A/D	$\zeta_{total}$	U[m/s]	Max. A/D
0	0.033	0.59	1.37	0.027	0.81	1.47	0.024	1.00	1.53	0.021	1.1	1.73
0.04	0.073	0.63	1.24	0.067	0.78	1.32	0.064	0.92	1.37	0.061	1.07	1.54
0.08	0.113	0.59	1.09	0.107	0.74	1.19	0.104	0.89	1.22	0.101	1.04	1.34
0.12	0.153	0.63	0.93	0.147	0.74	1.03	0.144	0.81	1.09	0.141	0.92	1.16
0.16	0.193	0.59	0.78	0.187	0.7	0.87	0.184	0.81	0.95	0.181	0.89	0.99
$\zeta_{harn}$	$k_{virtual} = 1200$ N/m			$k_{virtual} = 1400$ N/m			$k_{virtual} = 1600$ N/m			$k_{virtual} = 1600$ N/m		
	$\zeta_{total}$	U[m/s]	Max. A/D	$\zeta_{total}$	$\zeta_{total}$	$\zeta_{total}$	$\zeta_{total}$	U[m/s]	Max. A/D	$\zeta_{total}$	U[m/s]	Max. A/D
0	0.019	1.15	1.78	0.018	1.15	1.77	0.017	1.15	1.7	0.016	1.84	1.71
0.04	0.059	1.11	1.59	0.058	1.15	1.6	0.057	1.18	1.6	0.056	1.15	1.52
0.08	0.099	1.07	1.42	0.098	1.11	1.42	0.097	1.11	1.43	0.096	1.11	1.35
0.12	0.139	1.00	1.23	0.138	1.04	1.26	0.137	1.07	1.25	0.136	1.11	1.21
0.16	0.179	0.96	1.07	0.178	1.00	1.1	0.177	1.03	1.09	0.176	1.07	1.03

(j) The maximum  $A/D$  value of 1.78 is achieved at  $U=1.15$  m/s for  $k_{virtual} = 1200$  N/m and  $\zeta_{harn} = 0$ .

(k) The velocity where maximum  $A/D$  is achieved decreases with increasing  $\zeta_{harn}$  for each  $k_{virtual}$ . Exception to this rule is observed for  $k_{virtual} = 400$  N/m where the velocity is about constant due to high values of damping  $\zeta_{total}$ .

### 6.2.1.3. Frequency of Oscillation

The frequency ratio ( $f_{osc}/f_{n,water}$ ) versus current velocity ( $U$ ), reduced velocity ( $U^*$ ), and Reynolds number ( $Re$ ) for different  $\zeta_{harn}$  values for each  $k_{virtual}$  are shown in Figure 6-9 through Figure 6-16. On the same figures, the Strouhal frequency is shown for comparison. The following observations can be made:

- (l) At the onset of synchronization for all values of  $k_{virtual}$  and  $\zeta_{harn}$ , the frequency of oscillation deviates from the Strouhal frequency as expected and collapses around 1.
- (m) At the end of synchronization, around  $U^* = 9 - 10$ , frequency ratio lines cross over at about  $f_{osc}/f_{n,water} = 1.1$ .
- (n) During desynchronization where  $U^* = 10 - 15$  depending on  $k_{virtual}$  and  $\zeta_{harn}$ , the intermittent VIV frequency increases until the end of the desynchronization range where the forcing frequency returns to the Strouhal frequency.
- (o) For low  $k_{virtual}$  values, all frequency lines nearly collapse. With increasing  $k_{virtual}$ , the spread between the frequency lines becomes significant. Lines still cross at around  $U^* = 9$ ,  $f_{osc}/f_{n,water} = 1.1$ .

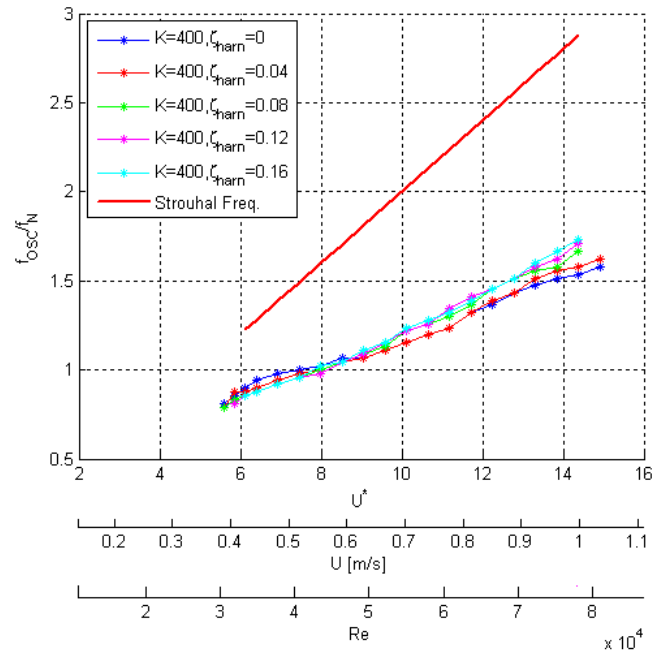


Figure 6-9.  $f_{osc}/f_{n,water}$  vs.  $U^*$ ,  $U$  and  $Re$  when  $k_{virtual} = 400\text{N/m}$  for various values of  $\zeta_{harn}$

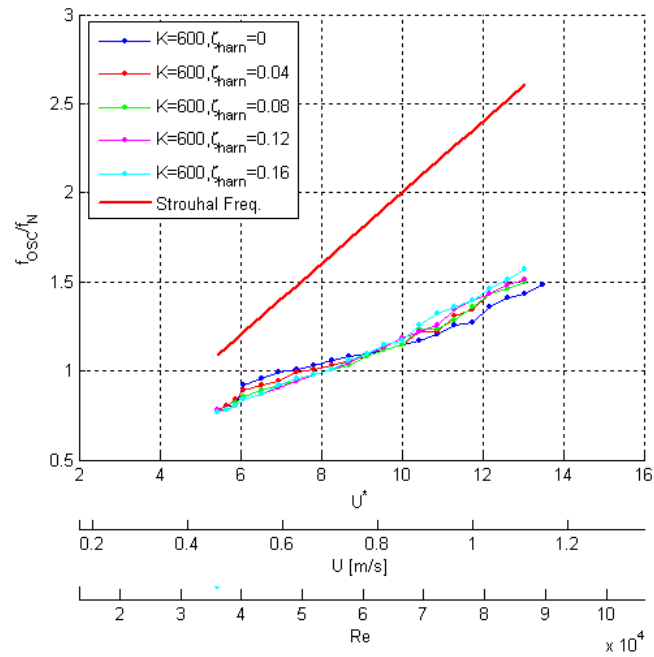


Figure 6-10.  $f_{osc}/f_{n,water}$  vs.  $U^*$ ,  $U$  and  $Re$  when  $k_{virtual} = 600\text{N/m}$  for various values of  $\zeta_{harn}$

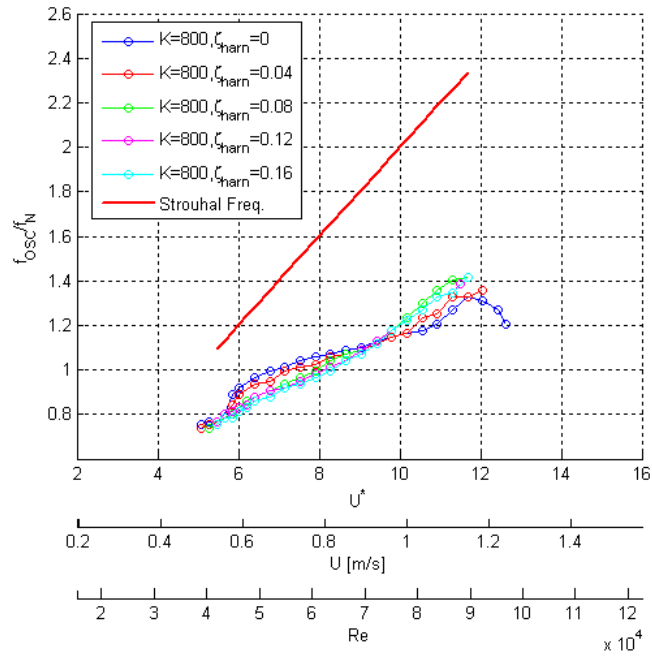


Figure 6-11.  $f_{osc}/f_{n,water}$  vs.  $U^*$ ,  $U$  and  $Re$  when  $k_{virtual} = 800\text{N/m}$  for various values of  $\zeta_{harn}$

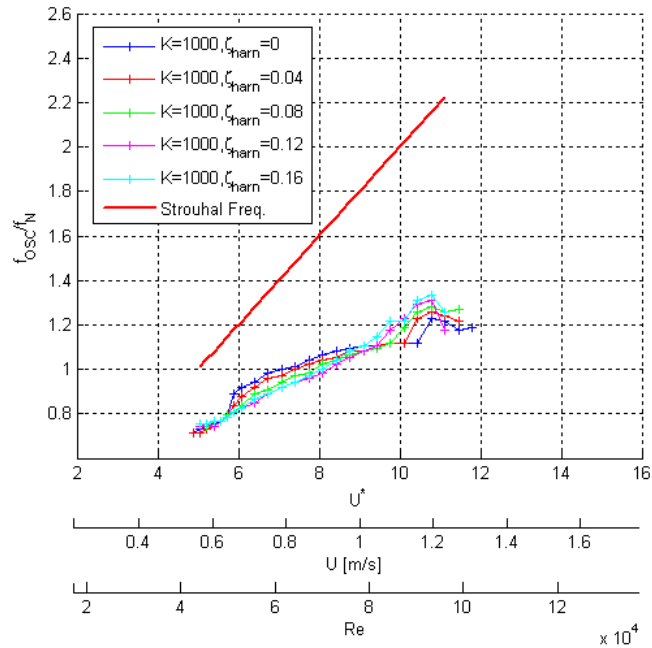


Figure 6-12.  $f_{osc}/f_{n,water}$  vs.  $U^*$ ,  $U$  and  $Re$  when  $k_{virtual} = 1000\text{N/m}$  for various values of  $\zeta_{harn}$

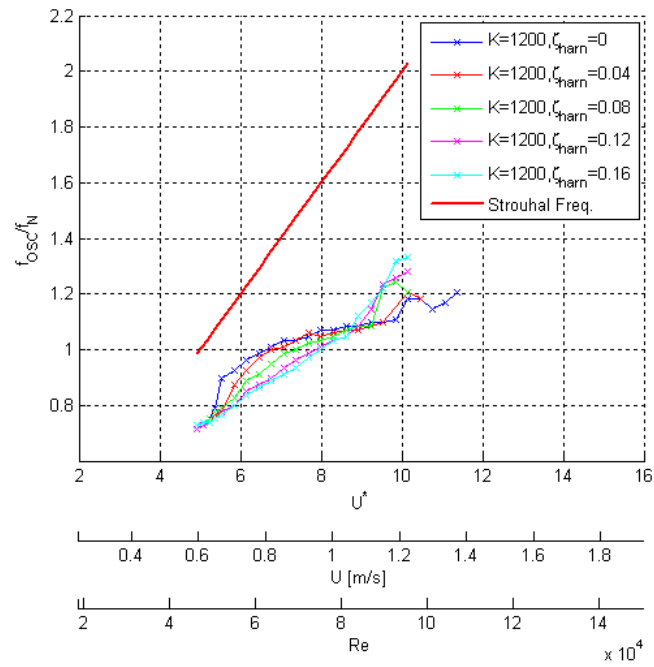


Figure 6-13.  $f_{osc}/f_{n,water}$  vs.  $U^*$ ,  $U$  and  $Re$  when  $k_{virtual} = 1200N/m$  for various values of  $\zeta_{harn}$

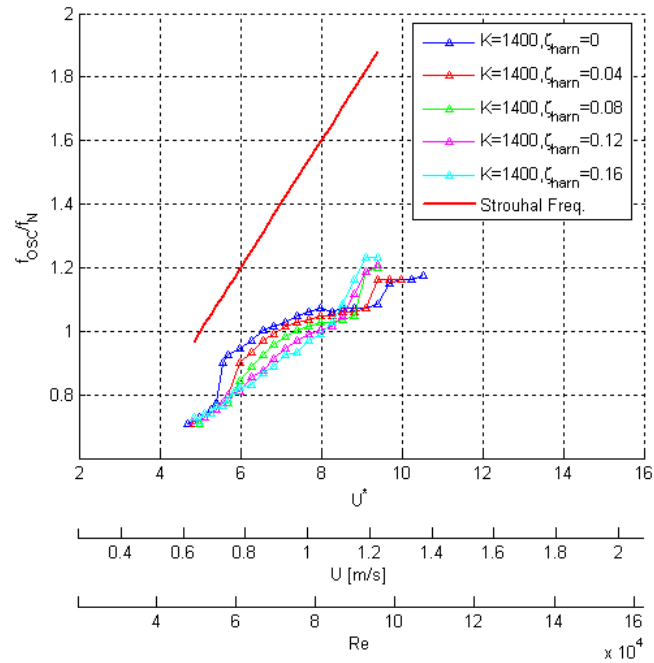


Figure 6-14.  $f_{osc}/f_{n,water}$  vs.  $U^*$ ,  $U$  and  $Re$  when  $k_{virtual} = 1400N/m$  for various values of  $\zeta_{harn}$

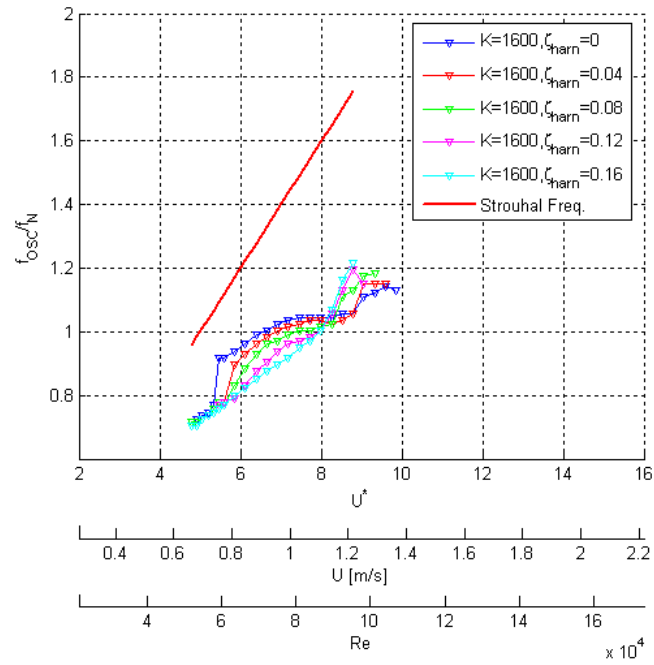


Figure 6-15.  $f_{osc}/f_{n,water}$  vs.  $U^*$ ,  $U$  and  $Re$  when  $k_{virtual} = 1600$  N/m for various values of  $\zeta_{harn}$

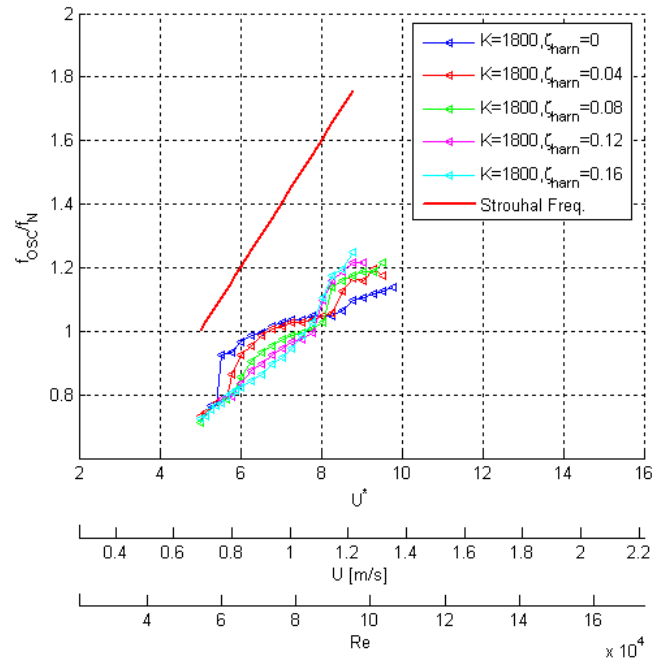


Figure 6-16.  $f_{osc}/f_{n,water}$  vs.  $U^*$ ,  $U$  and  $Re$  when  $k_{virtual} = 1800$  N/m for various values of  $\zeta_{harn}$

## 6.2.2. Effect of Stiffness K on VIV

The data presented in Figure 6-1 through Figure 6-8, are plotted in Figure 6-17 through Figure 6-21 for a given  $\zeta_{harn}$  and  $k_{virtual}$  as parameter. The independent variable is  $U$  and/or  $Re$ ;  $U^*$  has been removed as an independent variable to prevent collapsing of several figures into one. The following observations can be made:

- (p) As  $k_{virtual}$  increases the range of synchronization moves to higher velocity as expected. Specifically,  $f_{n,water}$  increases proportional to the square root of  $k_{virtual}$  while the synchronization range remains about constant with  $4 - 5 < U^* < 9 - 10$ . This is important for energy harnessing. Figure 6-17 through Figure 6-21 show the relation between flow velocity and appropriate  $k_{virtual}$ . Thus, with a simple change of  $k_{virtual}$ , VIVACE can achieve optimal energy harnessing without any mass adjustment or ballasting.
- (q) High values of  $\zeta_{total}$  result in more gradual onset of synchronization and more gradual desynchronization. This observation has an impact on the power envelop generated for the VIVACE Converter in Section 7.5.
- (r) The high lift regime TrSL3 comes to an end around  $Re = 10^5$  as shown in Figure 6-22. It is followed by TrBL0 which has lower but still high lift. Finally, TrBL1 has very low lift resulting in low amplitude VIV followed by full suppression of VIV in the transition from laminar to turbulent flow. Accordingly, as flow velocity increases and  $k_{virtual}$  is increased to move the synchronization range to higher velocity desynchronization becomes sharper. The challenge of VIV suppression in the flow transition region is overcome using passive turbulence control (Bernitsas and Raghavan 2007; Bernitsas and Raghavan 2008).

(s) As shown in Figure 6-17 and Table 6-1, maximum  $A/D$  for each graph increases with  $k_{virtual}$  up to 1200 N/m. It slightly decreases for higher speeds and  $k_{virtual}$ . This is consistent with the magnitude of lift as we move from the TrSL3 to TrBL0 flow regime.



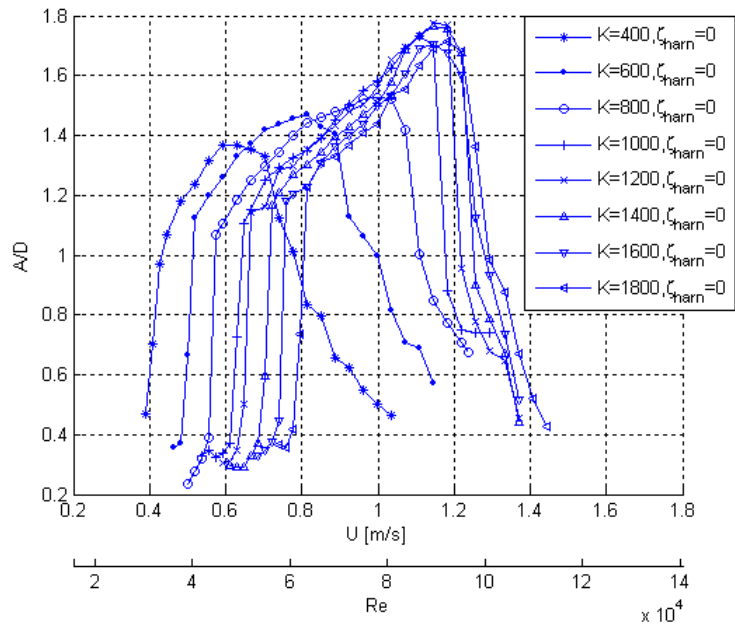


Figure 6-17. Amplitude ratios for  $\zeta_{harn} = 0$  for various values of  $k_{virtual}$

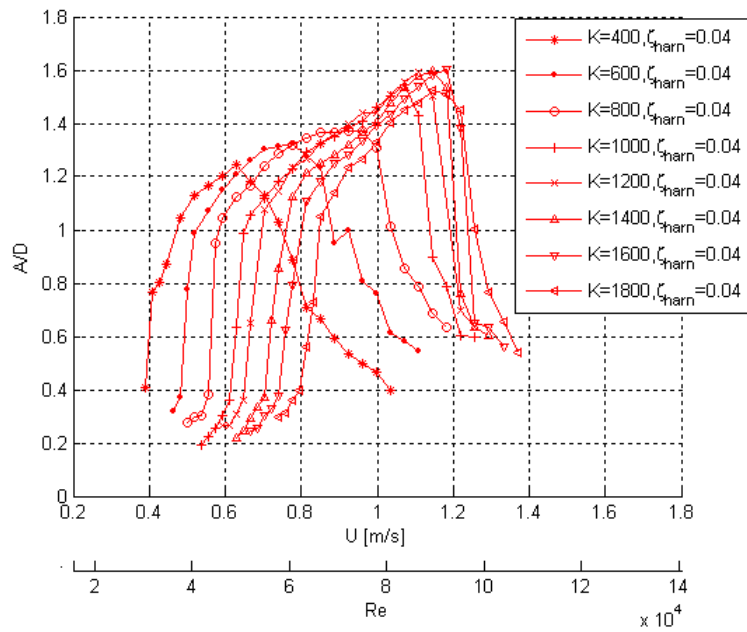


Figure 6-18. Amplitude ratios for  $\zeta_{harn} = 0.04$  for various values of  $k_{virtual}$

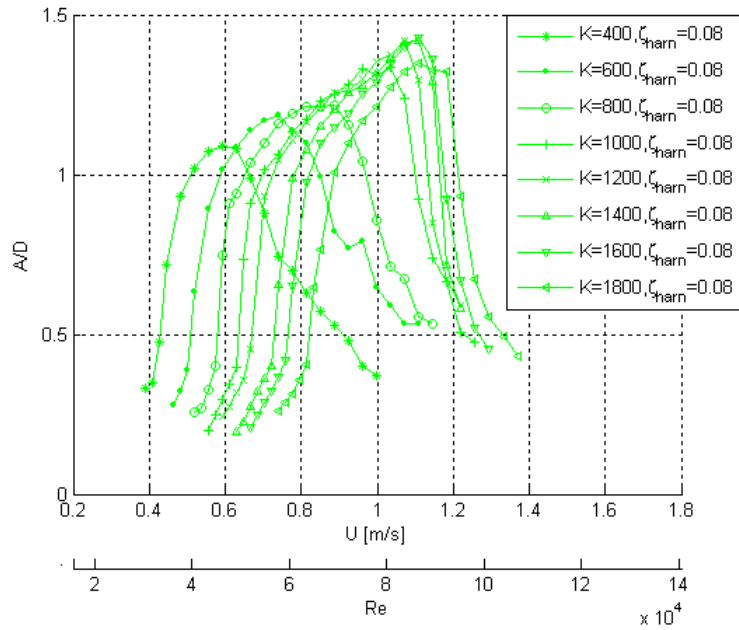


Figure 6-19. Amplitude ratios for  $\zeta_{harn} = 0.08$  for various values of  $k_{virtual}$

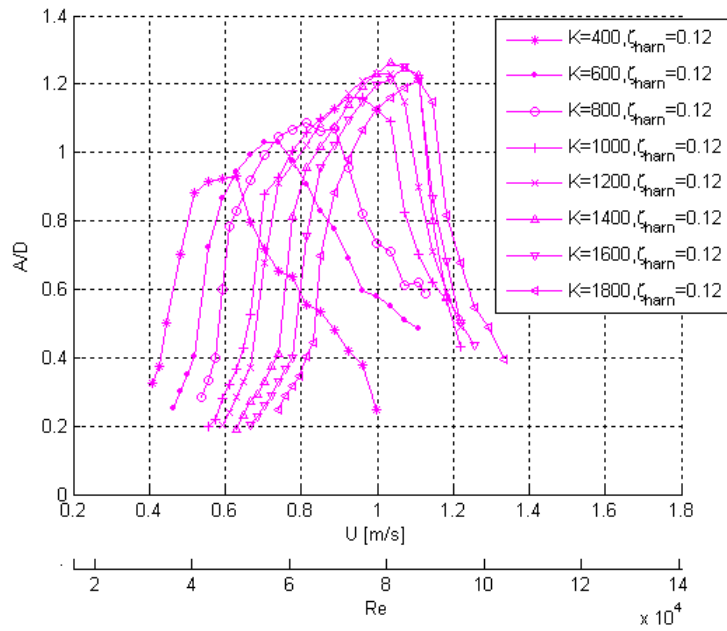


Figure 6-20. Amplitude ratios for  $\zeta_{harn} = 0.12$  for various values of  $k_{virtual}$

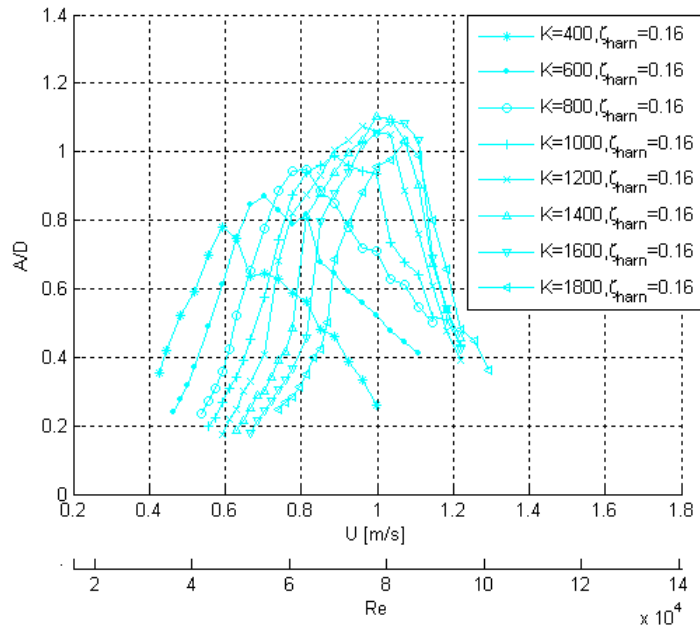


Figure 6-21. Amplitude ratios for  $\zeta_{harn} = 0.16$  for various values of  $k_{virtual}$

Drag and lift coefficients

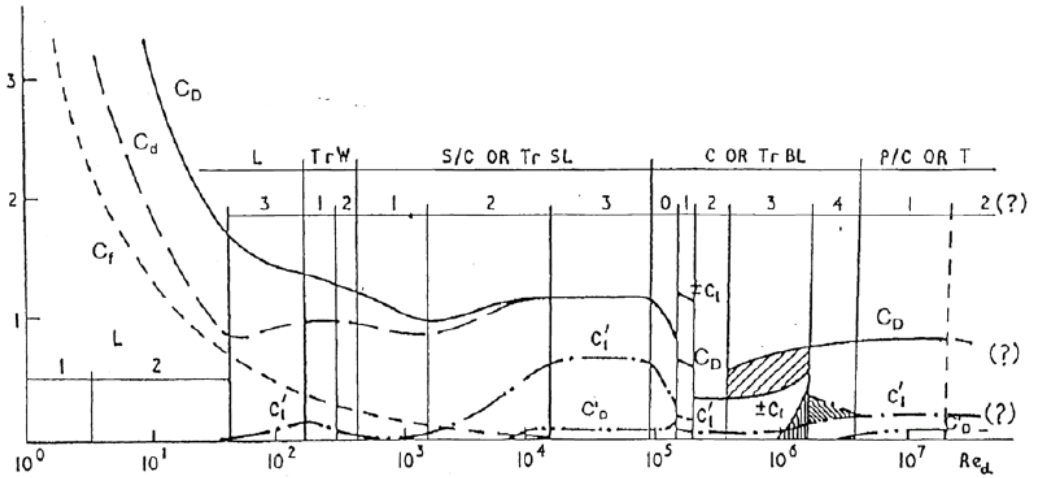


Figure 6-22. Drag and lift coefficients for a stationary circular cylinder (Zdravkovich 1990).

We can see that all data points of  $A/D$  in synchronization zone in Figure 6-17 fall in the TrSL3 when  $k_{virtual} \leq 1200$  N/m. In TrSL3 regime, the oscillating lift coefficient

remains almost constant with high values. However  $k_{virtual} > 1200$  N/m the end of synchronization starts falling into TrBL0 regime where the oscillating lift coefficient starts reducing. Considering  $\zeta_{total}$ s corresponding  $\zeta_{harm}$  is 0 for each  $k_{virtual}$  in Table 6-1 do not have significant difference, we can conclude that Reynolds number affects  $A/D$  in the synchronization range.

# CHAPTER 7.

## OPTIMAL POWER HARNESSING

From the results presented in CHAPTER 6, the power harnessed by the VIVACE Converter is calculated in this section and the power envelop is generated. The mathematical model of harnessed and dissipated power is summarized in Section 4.1. Results are compared to the theoretical upper limit. Energy density is also calculated.

### 7.1. Mathematical Model of Harnessed Power and Dissipated Power

The action of the generator in the VIVACE Converter to the oscillating component is modeled with damping term  $c_{harn}\dot{y}$ . Since the damping force from the bearings exists even in the physical VIVACE models, the equation of motion of the  $V_{CK}$  VIVACE model undergoing VIV in the water is given as:

$$m\ddot{y} + (c_{bearing} + c_{harn})\dot{y} + k_{virtual}y = f_{fluid}(t), \quad (7-1)$$

To obtain harnessed and dissipated power with the virtual  $V_{CK}$  VIVACE Converter, the left hand side of Eq. (7-1) is integrated after multiplying it by the instantaneous velocity  $\dot{y}$  and averaged over the cycle period  $T_{cyl}$ . This yields:

$$P_{VIVACE} = \frac{1}{T_{cyl}} \int_0^{T_{cyl}} (m\ddot{y} + (c_{bearing} + c_{harn})\dot{y} + k_{vitrual}y)\dot{y}dt . \quad (7-2)$$

If we assume that the VIV response is approximately sinusoidal the only nonzero term in Eq. (7-2) on the left hand side will be the damping term. This results in the power of the V<sub>CK</sub> VIVACE Converter:

$$P_{VIVACE} = \frac{1}{T_{cyl}} \int_0^{T_{cyl}} (c_{bearing} + c_{harn})\dot{y}^2 dt . \quad (7-3)$$

From Eq. (7-3), we obtain the harnessed and the dissipated power components of the V<sub>CK</sub> VIVACE Converter in Eq. (7-4) and Eq. (7-5), respectively.

$$P_{harn} = \frac{1}{T_{cyl}} \int_0^{T_{cyl}} c_{harn}\dot{y}^2 dt , \quad (7-4)$$

$$P_{dissip} = \frac{1}{T_{cyl}} \int_0^{T_{cyl}} c_{bearing}\dot{y}^2 dt . \quad (7-5)$$

The harnessed power in Eq. (7-4) is either dissipated at a heat bank (resistor box) or made available as electrical power. The power in Eq. (7-5) is dissipated in the form of heat through friction between bearings and shafts. Even if the VIV motion is not sinusoidal Eq. (7-4) and (7-5) are still valid. In that case, the  $\ddot{y}$  and  $y$  terms in Eq. (7-2) would dissipate additional energy that has been converted from hydrokinetic to mechanical.

## 7.2. Harnessed Power Calculation using Experimental Results

For each combination of  $k_{virtual}$  and  $\zeta_{harn}$ ,  $P_{harn}$  in Eq. (7-4) is calculated using a trapezoidal integration scheme with 0.01 second time step. 30 cycles of time history of  $P_{harn}$  are used to obtain averaged  $P_{harn}$ . It should be emphasized that all data points are used to average the harnessed power not just the top 10 peaks as in plotting  $A/D$  in Figure 7-1 through Figure 7-8.

The calculated harnessed power,  $P_{harn}$ , is presented for each value of  $k_{virtual}$  in Figure 7-1 though Figure 7-8. The following observations can be made:

- (t) For  $\zeta_{harn} = 0$ , no energy can be harnessed. For high values of  $\zeta_{harn}$ , the VIV amplitude is reduced resulting in less hydrokinetic energy converted to mechanical energy. As expected, an optimal value of  $\zeta_{harn}$  exists which allows maximum energy harnessing while maintaining VIV under high damping. This is observed for all values of  $k_{virtual}$  in Figure 7-1 though Figure 7-8.
- (u) In spite of the high number of tests performed, the resolution in  $\zeta_{harn}$  is less than desired resulting in an optimum  $\zeta_{harn} = 0.12$  for all  $k_{virtual}$  values tested. Nevertheless, the power envelop generated in Section 4.5 is sufficiently smooth.

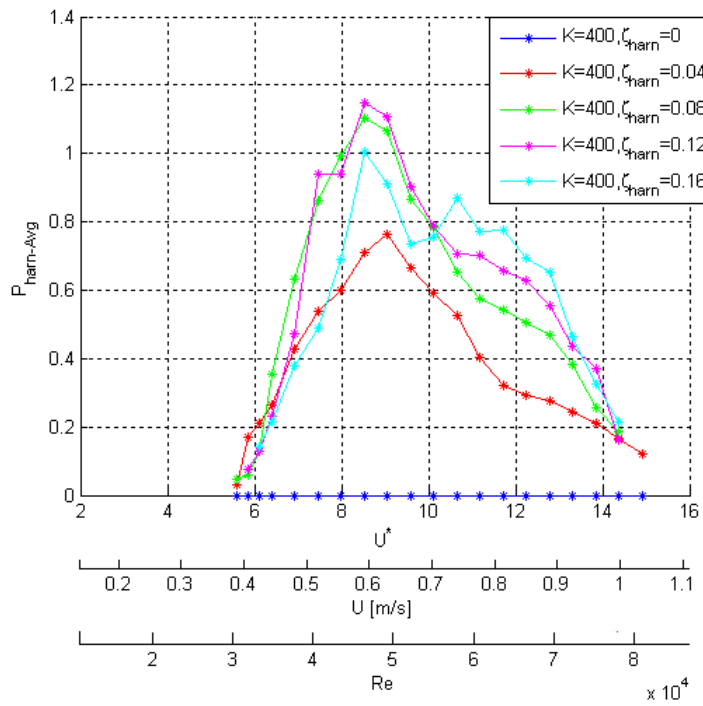


Figure 7-1. 30 cycle-averaged  $P_{harn}$  for  $k_{virtual} = 400$  N/m

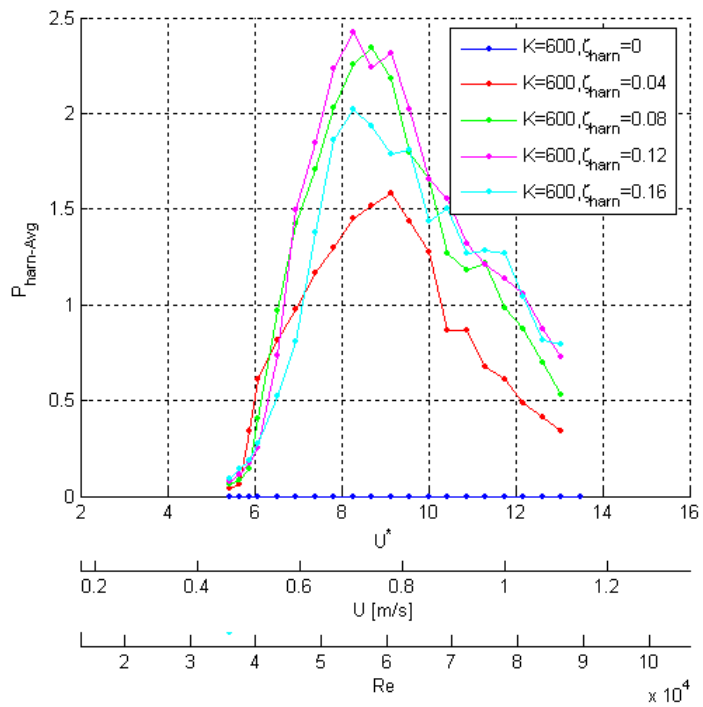


Figure 7-2. 30 cycle-averaged  $P_{harn}$  for  $k_{virtual} = 600$  N/m



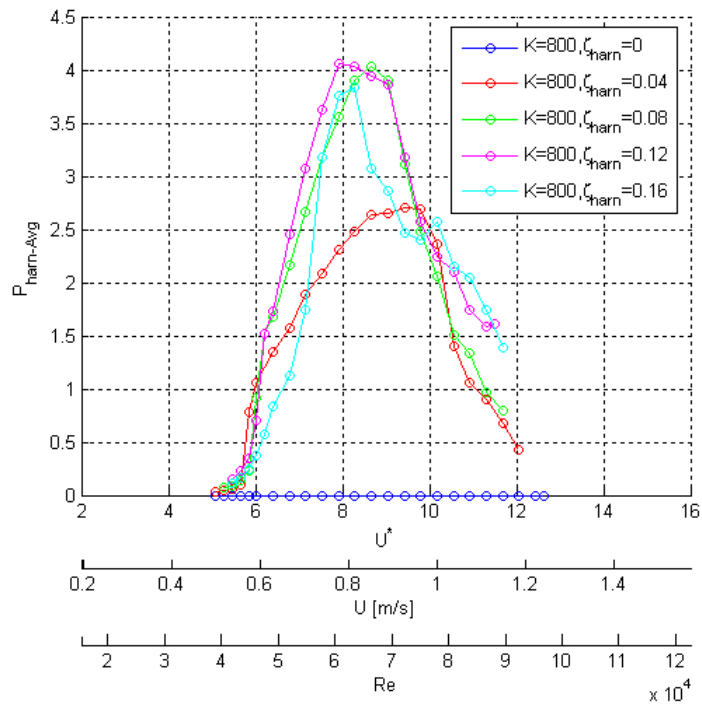


Figure 7-3. 30 cycle-averaged  $P_{harn}$  for  $k_{virtual} = 800$  N/m

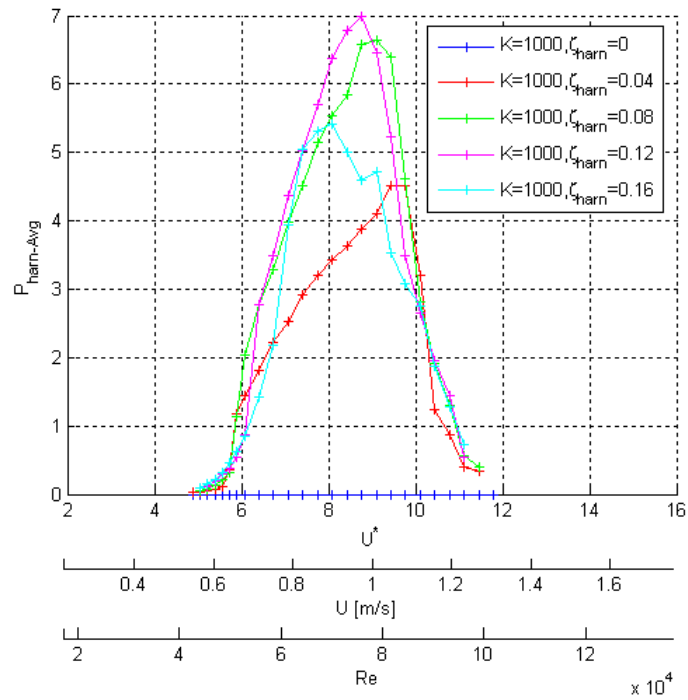


Figure 7-4. 30 cycle-averaged  $P_{harn}$  for  $k_{virtual} = 1000$  N/m

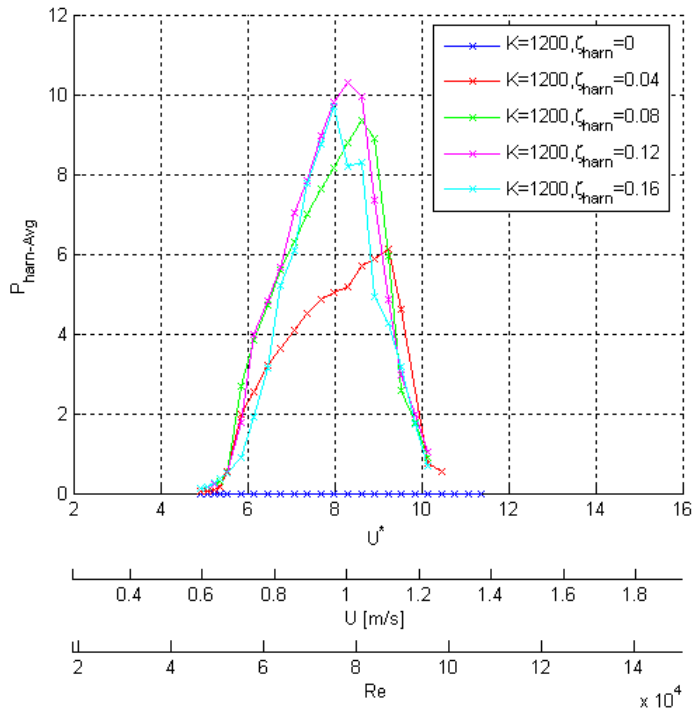


Figure 7-5. 30 cycle-averaged  $P_{harm}$  for  $k_{virtual} = 1200$  N/m

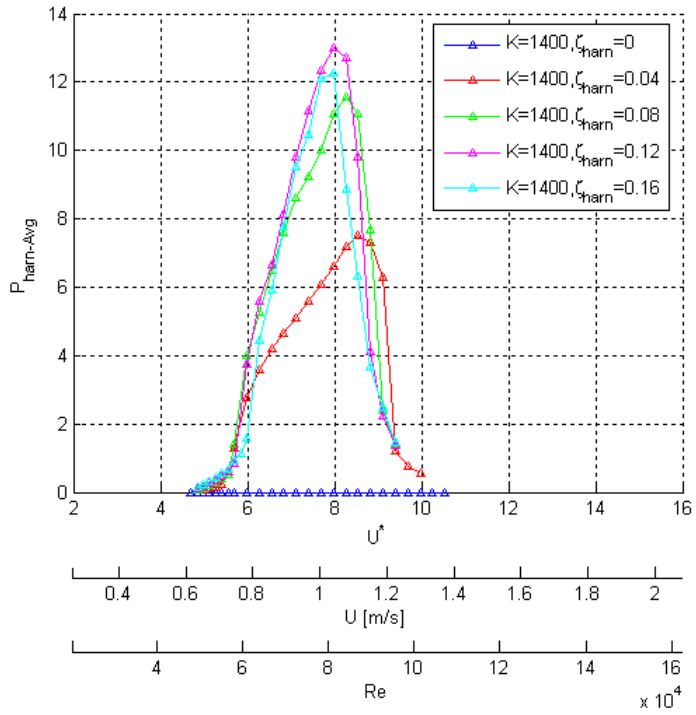


Figure 7-6. 30 cycle-averaged  $P_{harm}$  for  $k_{virtual} = 1400$  N/m

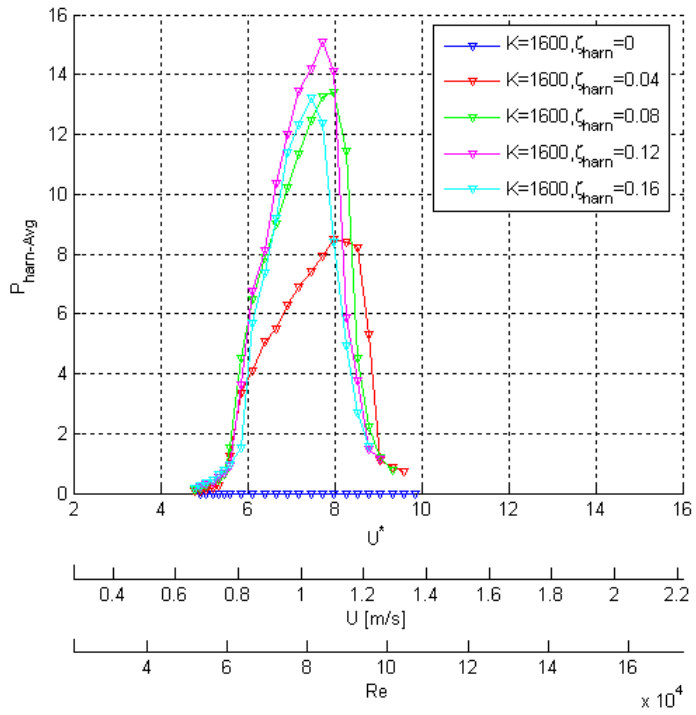


Figure 7-7. 30 cycle-averaged  $P_{harm}$  for  $k_{virtual} = 1600$  N/m

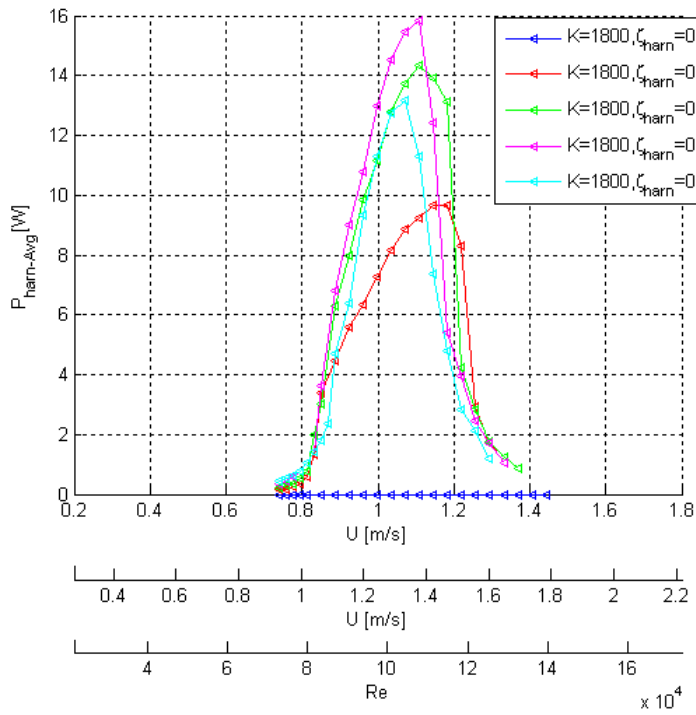


Figure 7-8. 30 cycle-averaged  $P_{harm}$  for  $k_{virtual} = 1800$  N/m

### 7.3. Theoretical Power Limit of V<sub>CK</sub> VIVACE model

The theoretical upper limit of the power that can be harnessed from a steady uniform flow has been calculated by Betz (Cuevas et al. 2006). Accordingly, this limit can be calculated for the flow in the LTFSW Channel as follows.

Let  $U$  and  $U'$  be the flow velocity upstream and downstream of the V<sub>CK</sub> VIVACE apparatus, respectively. Then, the mean flow velocity through the V<sub>CK</sub> VIVACE model is:

$$\tilde{U} = \frac{U + U'}{2}. \quad (7-6)$$

Utilizing Eq.(7-6), the mass flow rate through the cross section area of the channel is calculated as:

$$\dot{m}_{flow} = \rho W_{channel} D_{channel} \tilde{U} = \rho W_{channel} D_{channel} (U + U')/2, \quad (7-7)$$

where  $W_{channel}$  and  $D_{channel}$  are the width of the channel and water depth, respectively.

The converted power from the flow to the converter is the difference between the hydrokinetic energies upstream and downstream of the V<sub>CK</sub> VIVACE Converter. Thus, we have:

$$P = \frac{\dot{m}_{flow}}{2} (U^2 - U'^2) = \frac{\rho}{2} W_{channel} D_{channel} U^3 \left(1 + \frac{U'}{U}\right) \left[1 - \left(\frac{U'}{U}\right)^2\right]. \quad (7-8)$$

For fixed flow velocity  $U$ , the maximum power is harnessed when  $U'/U = 1/3$ . Thus, the theoretical power limit of  $P_{harn}$  is:

$$P_{max} = \frac{16\rho}{27} W_{channel} D_{channel} U^3 \approx 0.59 \cdot \frac{\rho}{2} W_{channel} D_{channel} U^3. \quad (7-9)$$

## 7.4. VIVACE Power Density

Power density is an important metric in comparing power devices and particularly renewable energy technologies. For the VIVACE Converter, calculations are based on the configuration shown in Figure 7-9. Specifically, to minimize cylinder interference based on model tests in the MRELab, a staggered configuration with 8 diameters center-to-center spacing in the direction of the flow and 5 diameters transversely is selected.

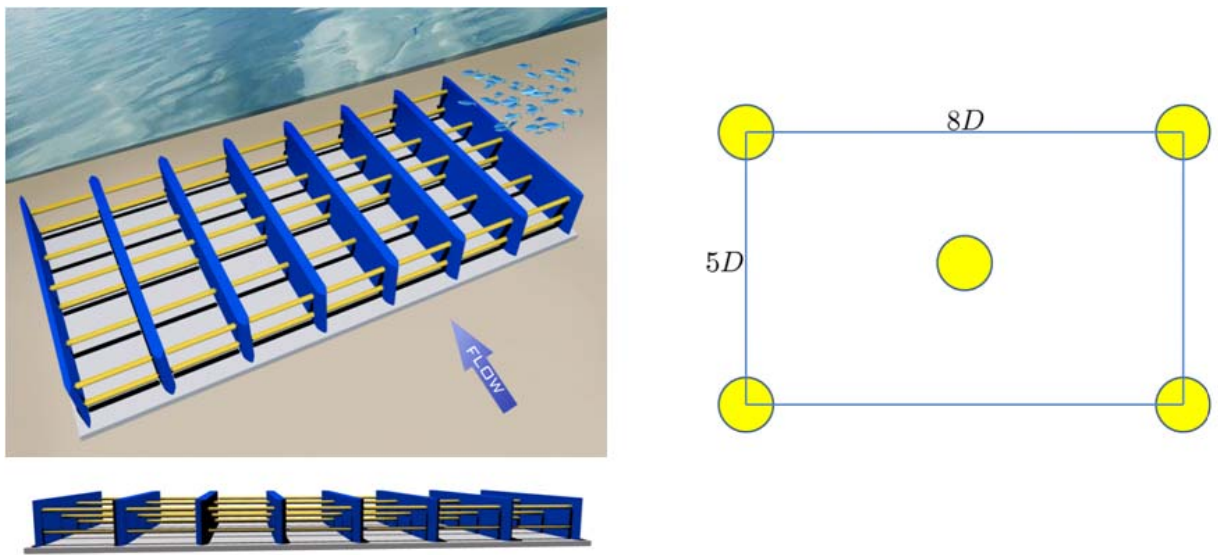


Figure 7-9. Configuration of cylinder deployment of the VIVACE Converter.

As a result, 2 cylinders are included in a volume of  $40D^2 \times L$ . Thus, the formula for calculating power density is:

$$\text{Power Density [W/m}^3\text{]} = \frac{2P_{harn}}{40D^2L}. \quad (7-10)$$

Based on Eq. (7-10) and the power envelop generated in Section 4.5, the power density for the VIVACE Converter is shown in Table 7-1. These results are assessed in Section 6 where power densities of some conventional and renewable sources of energy are compared.

## 7.5. Optimal Power Envelop of the $V_{CK}$ VIVACE Model

As explained in Section 7.2, the maximum harnessed power was achieved for  $\zeta_{harn} = 0.12$ . In Figure 7-10, the maximum power lines from Figure 7-1 through Figure 7-8 are superposed. The optimal power envelop is shown in

Figure 7-10 along with the dissipated power curve.

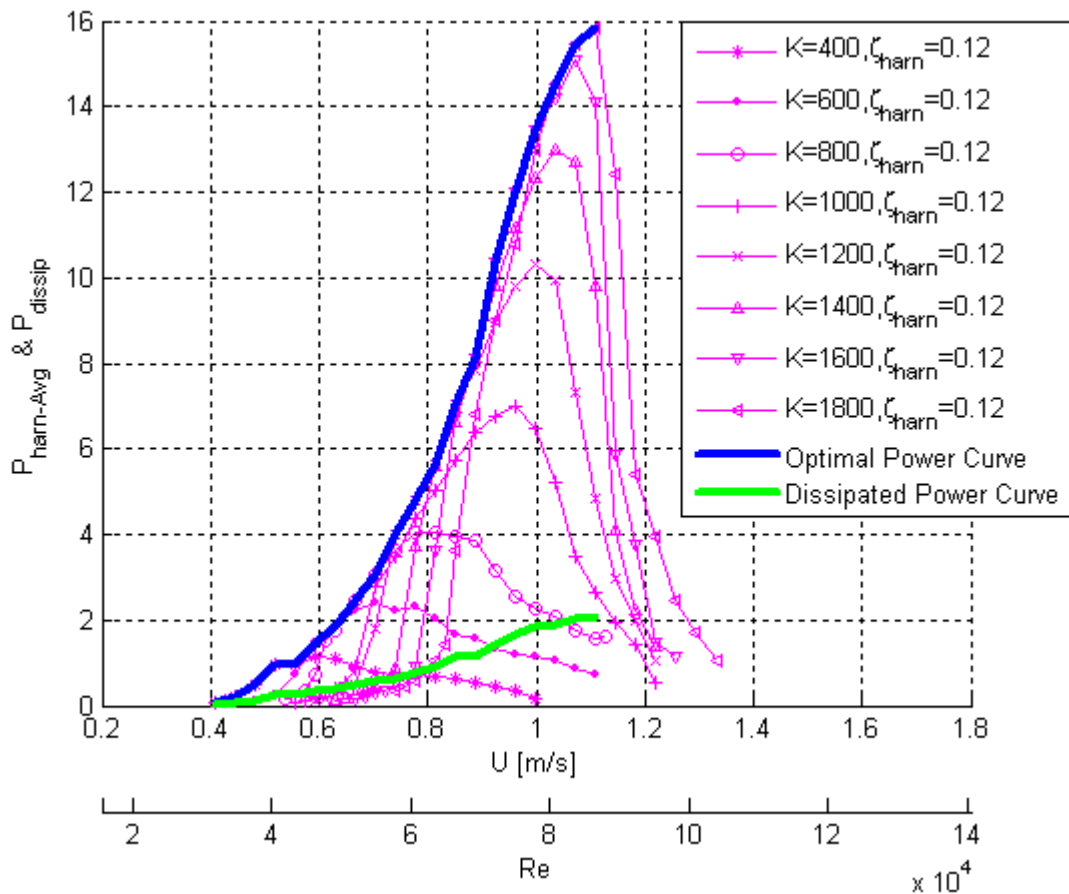


Figure 7-10. Optimal Power Envelop and Corresponding Dissipated Power

Figure 7-11 shows the various components of power at  $U = 1.04$  m/s which is approximately 2 knots. The latter is typical velocity of a river and consequently an



important number in assessing availability of power in low-head, low-speed hydrokinetic energy resources. Power charts for  $0.41 \text{ m/s} \leq U \leq 1.11 \text{ m/s}$  are shown in APPENDIX A.

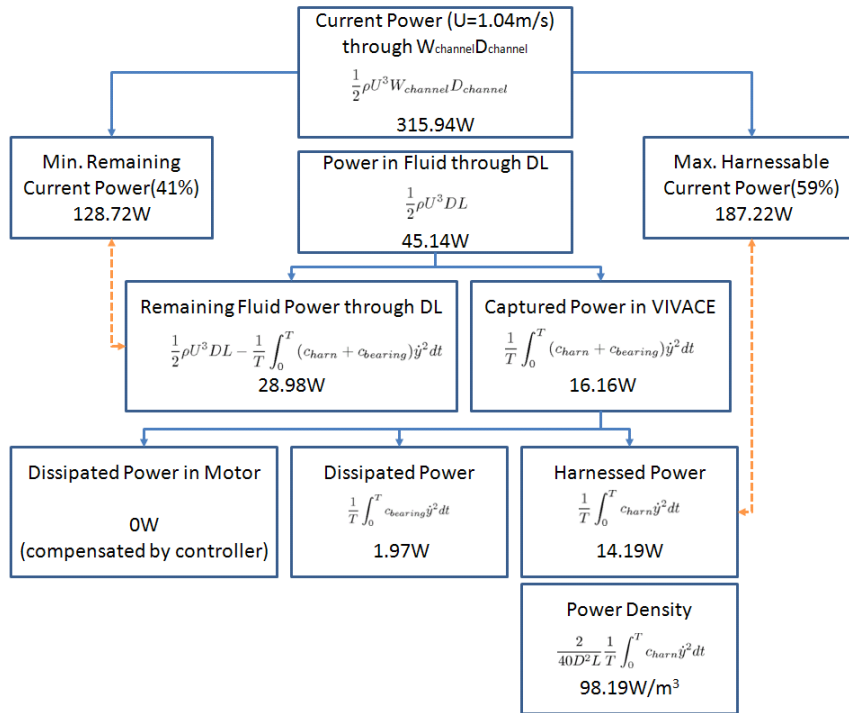


Figure 7-11. Power chart for  $U=1.04 \text{ m/s}$

The maximum  $P_{harn}$  achieved in this set of experiments is 15.85 W at flow speed of 1.11 m/s as shown in Table 7-1. Entries in Table 7-1 are calculated using the following equations:

Eq. (7-11) for the power in the LTFSW Channel

$$\text{Fluid Channel Power} = \frac{1}{2} \rho W_{channel} D_{channel} U^3 ; \quad (7-11)$$

Eq. (7-12) for the power through the cylinder projected area ( $DL$ ) in the direction of the flow

$$P_{fluid(DL)} = \frac{1}{2} \rho DLU^3; \quad (7-12)$$

Eq. (7-9) for the Betz limit, Eq. (7-3) for the power captured by VIVACE, Eq. (7-4) for the power harnessed by VIVACE, Eq. (7-5) for the power dissipated by bearings, and Eq. (7-10) for the power density. We can see from Table 7-1, that  $P_{harn}$  increases faster than  $U^3$  up to about  $U=1$  m/s. The maximum  $P_{harn}/P_{fluid(DL)}= 33.23\%$  was achieved at 0.96 m/s of flow velocity with a corresponding  $P_{harn}/P_{max} = 8.01\%$  .

Table 7-1. Power generated by the VIVACE Converter

Current Velocity [m/s]	Current Velocity [knots]	Fluid Channel Power [W] Eq. (7-11)	Betz's Limit [W] Eq. (7-9)	Fluid Power in DL [W] Eq. (7-12)	$P_{harm}$ by VIVACE [W] Eq. (7-4)	$P_{dissip}$ by VIVACE [W] Eq. (7-5)	Power Captured by VIVACE [W] Eq. (7-3)	VIVACE Power Density [W/m <sup>3</sup> ] Eq. (7-10)	$P_{harm}/P_{max} \times 100$ [%]	$P_{harm}/P_{fluid(DL)} \times 100$ [%]
0.41	0.797	19.16	11.36	2.74	0.08	0.02	0.1	0.54	0.68	2.84
0.44	0.855	24.87	14.74	3.55	0.24	0.06	0.3	1.6	1.57	6.51
0.48	0.933	31.62	18.74	4.52	0.47	0.13	0.6	3.27	2.53	10.48
0.52	1.011	39.49	23.4	5.64	0.94	0.26	1.2	6.51	4.02	16.68
0.55	1.069	48.57	28.78	6.94	0.94	0.26	1.2	6.51	3.27	13.56
0.59	1.147	58.95	34.93	8.42	1.49	0.34	1.83	10.33	4.28	17.73
0.63	1.225	70.71	41.9	10.1	1.85	0.42	2.27	12.79	4.41	18.29
0.67	1.302	83.94	49.74	11.99	2.45	0.48	2.93	16.97	4.93	20.45
0.70	1.361	98.72	58.5	14.1	3.07	0.6	3.67	21.23	5.25	21.76
0.74	1.438	115.14	68.23	16.45	4.00	0.64	4.64	27.65	5.86	24.30
0.78	1.516	133.29	78.99	19.04	4.81	0.77	5.58	33.29	6.09	25.26
0.81	1.575	153.25	90.82	21.9	5.65	0.91	6.56	39.11	6.22	25.82
0.85	1.652	175.11	103.77	25.02	7.03	1.12	8.15	48.62	6.77	28.09
0.89	1.730	198.96	117.9	28.43	8.13	1.13	9.26	56.27	6.90	28.61
0.92	1.788	224.88	133.26	32.13	10.37	1.44	11.81	71.78	7.79	32.29
0.96	1.866	252.96	149.9	36.14	12.01	1.66	13.67	83.08	8.01	33.23
1.00	1.944	283.29	167.87	40.47	13.43	1.86	15.29	92.93	8.00	33.18
1.04	2.022	315.94	187.22	45.14	14.19	1.97	16.16	98.19	7.58	31.44
1.07	2.080	351.02	208.01	50.15	15.11	2.09	17.2	104.52	7.26	30.12
1.11	2.158	388.59	230.28	55.52	15.85	2.07	17.92	109.65	6.88	28.54

## **CHAPTER 8.**

### **POWER DENSITY ASSESSMENT**

Comparison between energy sources is not readily possible as there are differences in availability, cost, geography, technology, efficiency, conditioning, storage, transportation, infrastructure, quality of energy source, renewability, politics, environmental impact, long-term sustainability, and other factors. Two facts are certain: First, that the energy challenge tops all relevant lists that have been published and it is likely to remain at the top in the foreseeable future. Second, that all financially competitive sources of energy have to be used until a long-term sustainable energy world-wide system is achieved in no more than 40-50 years.

In the short term of no more than 20 years, power density has emerged as a universal factor in comparing energy sources. It relates to cost, maintenance, space utilization, environmental impact, etc. The numerator is the amount of power that a combination of source-technology can deliver and the denominator is the entire volume that cannot be used simultaneously in any other way due to the presence of the power device. Power density is an important metric in benchmarking and comparing energy sources - conventional or alternative, depletable or renewable.

Of course, fossil fuels/technology and particularly Diesel engines deliver the highest ratio at about  $25,000\text{Watts/m}^3$ . The denominator in this metric should not be confused with the combustion volume typically used in car engine power density ratings. Renewable energy sources have the lowest power density.

While it is relatively straight-forward to measure the output power - averaged over a period of time to account for availability due to intermittent supply as in wind, wave, solar energies - what is included in the denominator requires further discussion. Here are some examples:

(i) Volume for Diesel engines includes all space occupied by the engine, fuel lines, support, vibration absorbers, etc where no other equipment can be placed. Whether it would include accessing space above and below would depend on space availability and cost, which varies greatly between large ships, speedboats, and motor vehicles. The value of  $25,000\text{Watts/m}^3$  mentioned for Diesel engines includes only the space occupied by the engine itself.

(ii) Wind turbines occupy land space and have considerable height – about 100m - where other wind turbines cannot be used. That three-dimensional space is definitely valuable and should be included in the denominator. The space above that, even though cannot be used by other windmills, is of no obvious value and should not be included.

(iii) Marine power converters vary widely. Wave buoys are surface point absorbers and typically are moored. They harness vertical hydrokinetic energy. In the denominator, the horizontal space between buoys in a two-dimensional farm should be used. What should the third dimension of the occupied volume be, the distance to the ocean bed where the presence of the mooring system precludes other use of the ocean space or the wave action

depth equal to about half the wave length? The footprint volume is probably reasonable to use defined as the surface area occupied times the water depth.

(iv) Wave attenuators, such as Pelamis, have a spread mooring system that precludes use of underwater ocean space far larger than the footprint volume of such a surface device. Which space should be included in the denominator, footprint or used volume?

(v) Water turbines have the same used and footprint volume and the denominator should include all volume downstream of turbines that is required before an other turbine is installed downstream in a farm. Footprint volume includes space from sea-surface to sea-bed since there is plenty of horizontal hydrokinetic energy that can be harnessed in that space.

(vi) In calculating the energy density of the VIVACE converter, the footprint volume should be used as well. VIVACE is designed as a three dimensional device that can harness energy from the complete volume it occupies. The obvious challenge of wake turbulence and its effect on downstream cylinders has been very well addressed based on passive turbulence control (Bernitsas and Raghavan 2007; Raghavan and Bernitsas 2008).

In the power density benchmarking performed among marine energy converters in Bernitsas et al. (2008, 2009) the footprint volume has been used for all devices. Next we examine the power density of wind turbines as they are a well established industry with clear market, production, cost, and environmental impact; and the power density of VIVACE based on data generated in Table 7-1.

Wind Power Density: The world largest wind farm is the Horse Hollow Wind Energy Center, Texas. It generates 735.5 MW with 291 GE Energy 1.5 MW wind turbines and 130 Siemens 2.3 MW wind turbines spread over an area of 190 km<sup>2</sup>. The rated wind

speed for the wind turbines is 12 m/s. For a wind availability of 30%, the actual wind power output is  $735.5\text{MW} \times 0.30 = 220.65\text{MW}$ . For a total height of the wind turbine of 115 m, the occupied volume is  $190 \text{ km}^2 \times 0.115 \text{ km} = 21.85 \text{ km}^3$ . Therefore the power density of the wind turbine is:

$$\begin{aligned} \text{Power Density(Wind Turbine, 12 m/s)} &= 220.65 \text{ MW}/21.85 \text{ km}^3 & (8-1) \\ &= 10.1 \text{ MW}/\text{km}^3. \end{aligned}$$

VIVACE Power Density: To compare the power density of the wind turbine with that of the VIVACE Converter, we need to find the water flow speed corresponding to the rated wind speed of 12 m/s. As the water to air density ratio is 830, the corresponding flow velocity  $U$  is:

$$\sqrt[3]{\frac{(12 \text{ m/s})^3}{830}} = 1.3 \text{ m/s}. \quad (8-2)$$

The maximum flow velocity achieved in the LTFWSW Channel experiments was 1.11 m/s as shown in Table 6. Since power is proportional to velocity cube, the power density envelop of the VIVACE Converter is curve-fitted by  $84.13U^3$ . Accordingly, the power density of the VIVACE Converter at the corresponding flow speed of 1.3 m/s is  $184.8\text{W}/\text{m}^3 = 184,800 \text{ MW}/\text{km}^3$ . Assuming an availability of water flow (including maintenance down-time) of 80% the power density of the VIVACE Converter is:

$$\begin{aligned}
 \text{Power Density(VIVACE, 1.3 m/s)} &= 184,800 \text{ MW/km}^3 \times 0.80 \\
 &= 147,840 \text{ MW/km}^3,
 \end{aligned}
 \tag{8-3}$$

resulting in a ratio of

$$\frac{\text{Power Density(VIVACE, 1.3 m/s)}}{\text{Power Density(Wind Turbine, 12 m/s)}} = \frac{147,840 \text{ MW/km}^3}{10.1 \text{ MW/km}^3} = 14,600
 \tag{8-4}$$

It is worth extrapolating the VIVACE Converter power density for two more speeds, 3 knots which is typical ocean current speed, and 6 knots where turbines are designed even though there are only seven sites of such water flow speed in the USA (Bedard et al. 2005).

For 3 knots,

$$\begin{aligned}
 \text{Power Density(VIVACE, 3 knots)} &= 309,000 \text{ MW/km}^3 \times 0.80 = 247,000 \text{ MW/km}^3 \\
 &= 247 \text{ W/m}^3
 \end{aligned}
 \tag{8-5}$$

For 6 knots,



$$\begin{aligned} \text{Power Density(VIVACE, 6 knots)} &= 2,475,000 \text{ MW/km}^3 \times 0.80 \\ &= 1,980,000 \text{ MW/km}^3 = 1,980 \text{ W/m}^3 \end{aligned} \tag{8-6}$$

Eq. (8-6) yields a value which is only about one order of magnitude less than the power density of Diesel engines. Even though achieving such power density for VIVACE is still 5 – 10 years in the future, it provides an achievable target for future development. Research in PTC and fish kinematics is required to achieve that target.

# **CHAPTER 9.**

## **CONCLUSIONS AND RECOMMENDATIONS**

In this chapter, the main findings and thesis contributions are presented. Suggestions for future research work are provided towards the end of this chapter. The findings of this study are first of its kind to the author's knowledge.

### 9.1. Main Findings and Thesis Contributions

This work is accomplished in two phases, PART. A and B.

In PART A, we have designed and built the  $V_{CK}$  VIVACE Converter. It consists of a cylinder, a belt and pulley transmission, a motor/generator, and a controller. The  $V_{CK}$  system enables conducting high number of model tests quickly as damping and springs are set by software rather than hardware. The controller provides a damper-force and spring-force feedback based on displacement and velocity measurements, thus introducing no additional artificial force-displacement phase lag, which would bias energy conversion.

The damping of even such a simple spring-damper-mass system is strongly nonlinear, even in air, particularly away from the system's natural frequency. This nonlinearity strongly affects modeling near the ends of the VIV synchronization range. System

identification (SI) in air reveals nonlinear viscous damping, static friction, and kinetic friction. The LARNOS model adopted successfully predicted the hysteresis phenomenon occurring in the zero velocity limit. The performance of the  $V_{CK}$  VIVACE model was verified by comparing the amplitude response characteristics ( $A/D$ ) with that of a VIVACE model with physical springs and damping.

In PART B, we have carried out extensive experiments in the velocity range  $0.40\text{m/s} < U < 1.11\text{m/s}$  using spring stiffness  $400\text{N/m} < k < 1800\text{N/m}$  to calculate the optimal harnessed power by the  $V_{CK}$  VIVACE Converter. Tests are performed for Reynolds number  $40,000 < Re < 120,000$  and damping  $0 < \zeta < 0.16$ . Section 6.2 deals with the experimental results for high damping VIV.

The main findings on the effect of damping are provided in sub-sections of Section 6.2.1. Findings on the effect of damping on range of synchronization, amplitude of oscillation, frequency of oscillation are summarized in subsections 6.2.1.1, 6.2.1.2, and 6.2.1.3, respectively.

The main findings on the effect of spring stiffness are provided in Section 6.2.2.

In CHAPTER 7, the optimal harnessed power is calculated. The maximum  $P_{harn}$  achieved is 15.85 W at flow speed of 1.11 m/s. The maximum  $P_{harn}/P_{fluid(DL)} = 33.23\%$  was achieved at 0.96 m/s of flow velocity with a corresponding  $P_{harn}/P_{max} = 8.01\%$ .

In CHAPTER 8, power density assessment of the  $V_{CK}$  VIVACE Converter has been made and is compared with the power density of Wind Turbines at corresponding

conditions. The achieved power density of the V<sub>CK</sub> VIVACE Converter 147,840 MW/km<sup>3</sup> is 14,600 times higher than that of wind turbines.

## 9.2. Recommendations for Future Research

Two major recommendations are made below for research to be performed as an immediate follow up development of this work:

- (a) Design, build, test and verify a virtual mass-damper-spring system by adding to the  $V_{CK}$  system developed in this work acceleration measurement and acceleration feedback control. This development will make it possible to study the effect of mass ratio ( $m^*$ ) on VIV. It has been reported in the literature that  $m^* < 0.54$  may result in perpetual VIV (Govardhan and Williamson 2002).  $V_{MCK}$  will make it possible to study further the effect of  $m^*$  on galloping and investigate avenues for even higher energy harnessing by VIVACE.
- (b) The biggest advantage of the VIVACE Converter compared to other energy converters is its three-dimensional nature. Wave buoys are point absorbers, liner attenuators like pelamis are line absorbers with basically 3-point absorption, oscillating water columns are surface absorbers, and turbines are also area absorbers. VIVACE can have 3-D distribution of cylinders in space. The challenge is to find the optimized special distribution of cylinders. For that purpose, four  $V_{CK}$  's have been built and need to be calibrated for simultaneous operation in the LTFWS Channel. Those will provide information on optimal distance of VIVACE Converters.

# APPENDIX A.

## VIVACE POWER CHARTS

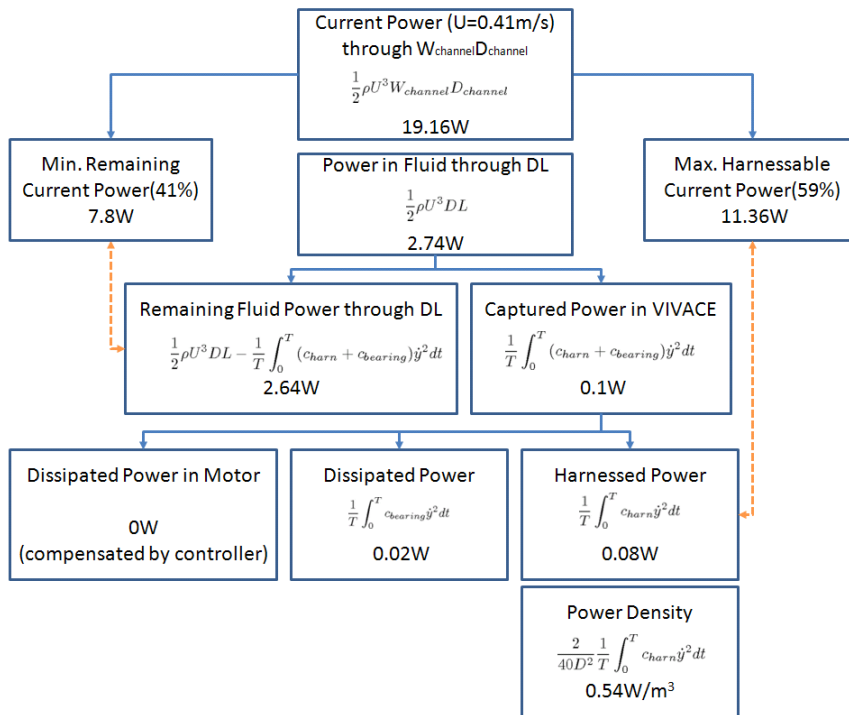


Figure A-1. Power chart for  $U=0.41$  m/s

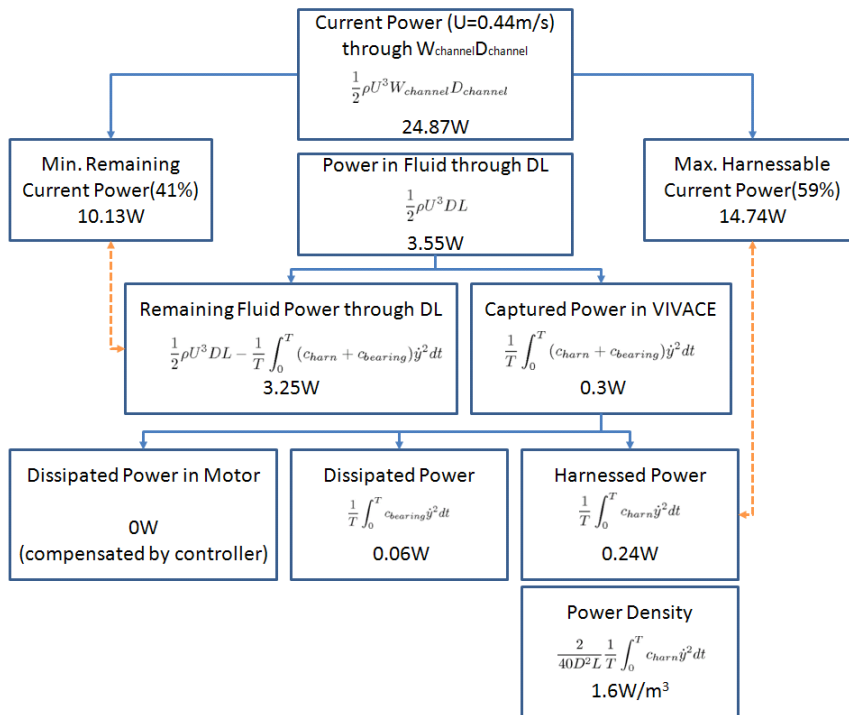


Figure A-2. Power chart for  $U=0.44$  m/s

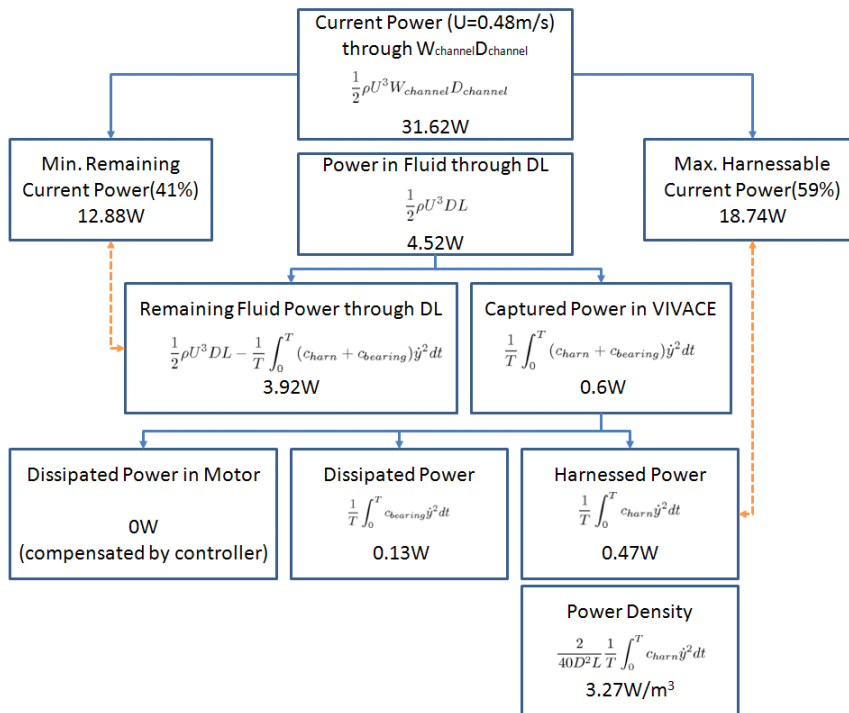


Figure A-3. Power chart for  $U=0.48$  m/s

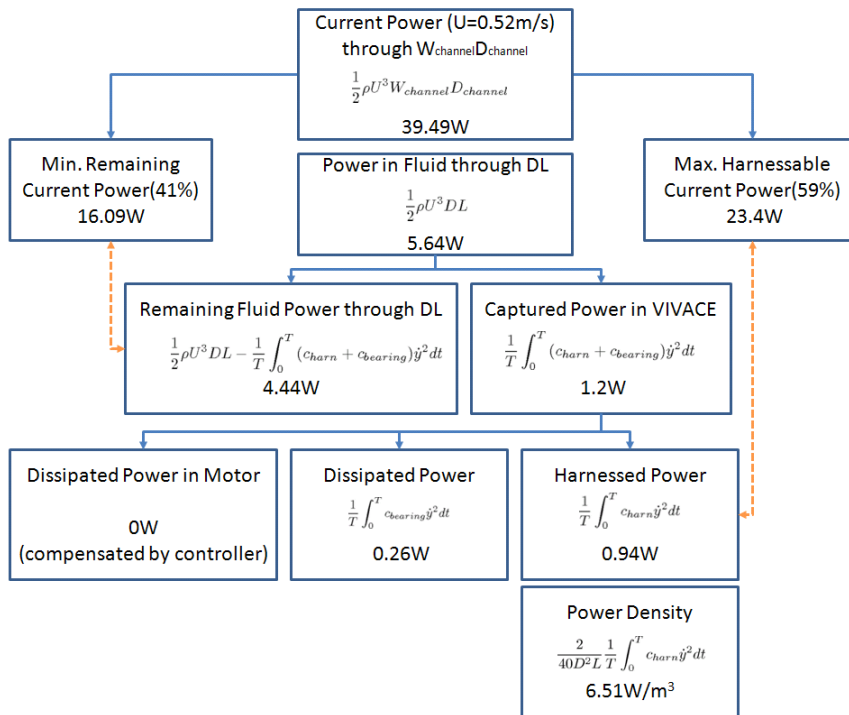


Figure A-4. Power chart for  $U=0.52$  m/s

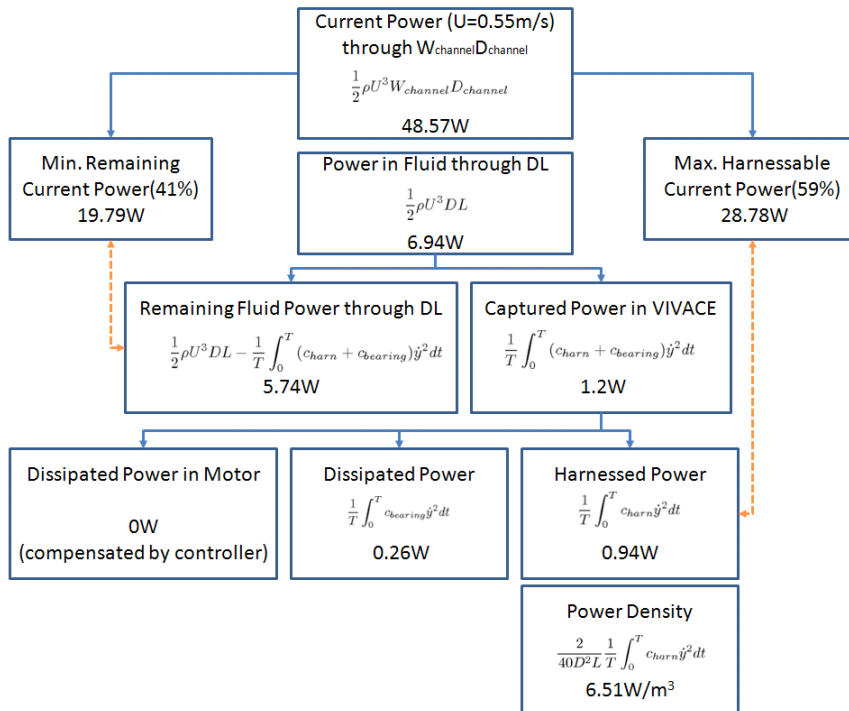


Figure A-5. Power chart for  $U=0.55$  m/s



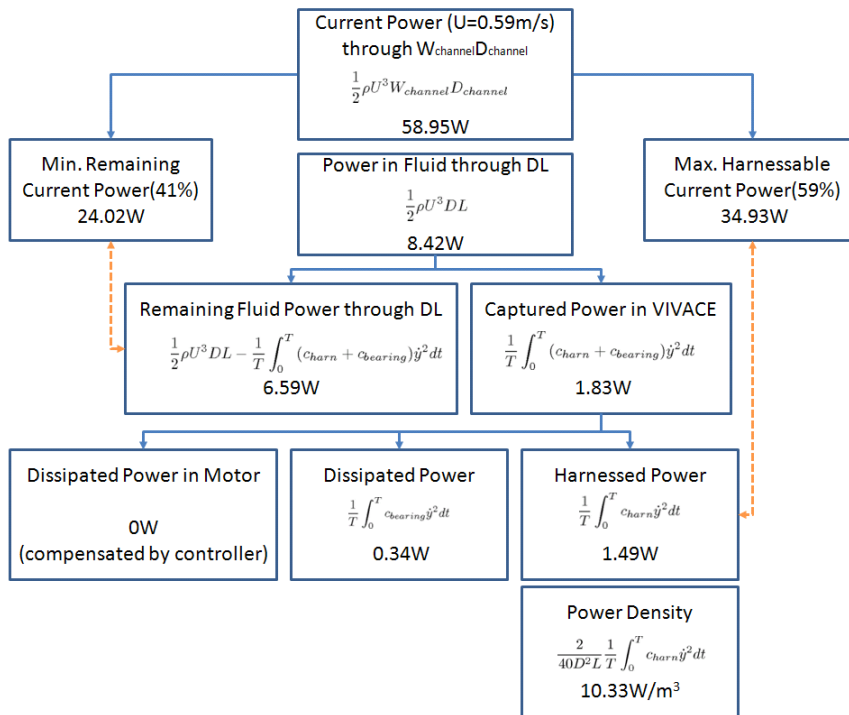


Figure A-6. Power chart for  $U=0.59$  m/s

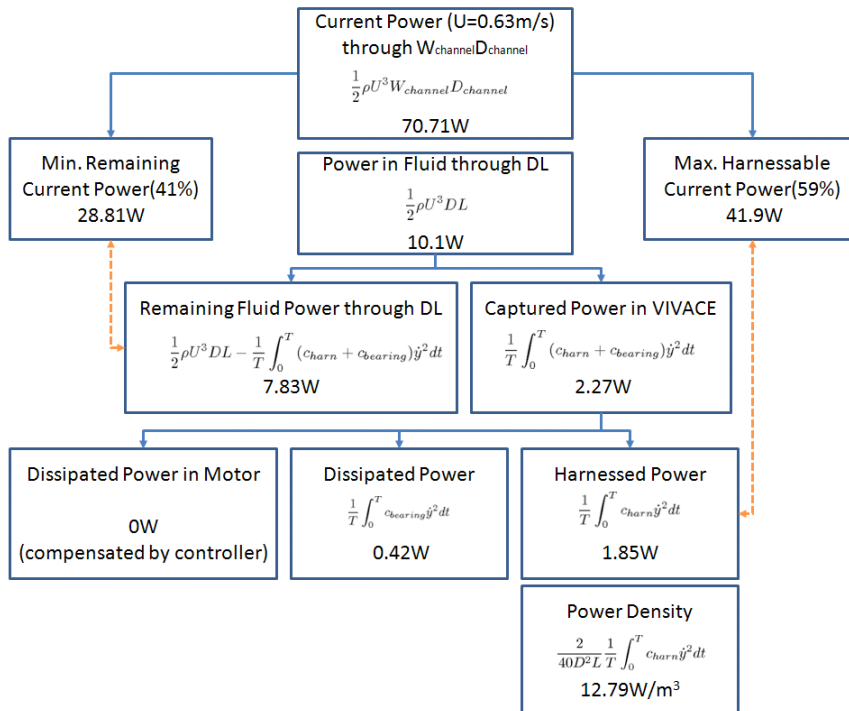


Figure A-7. Power chart for  $U=0.63$  m/s

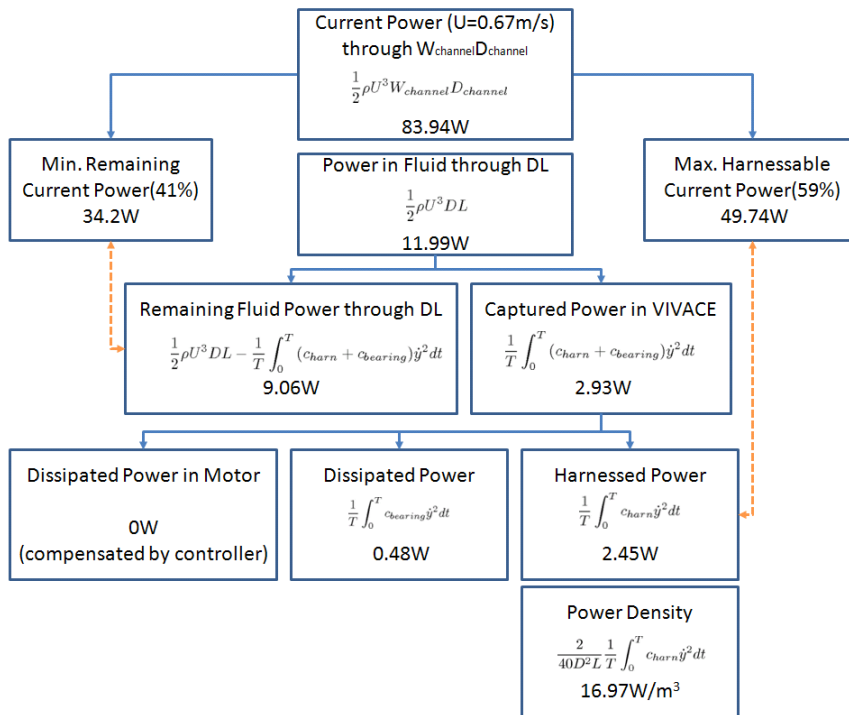


Figure A-8. Power chart for  $U=0.67$  m/s

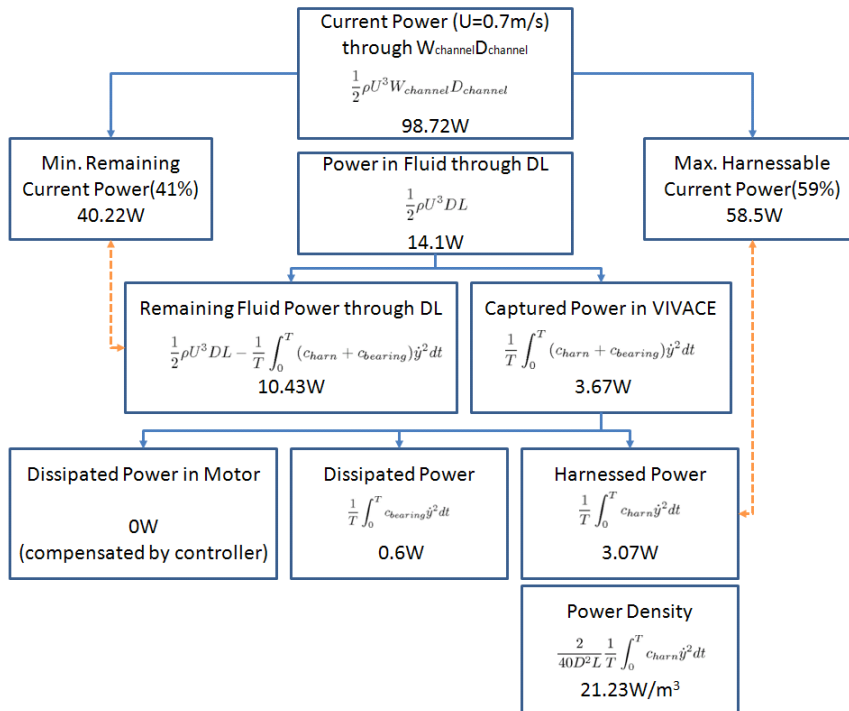


Figure A-9. Power chart for  $U=0.7$  m/s

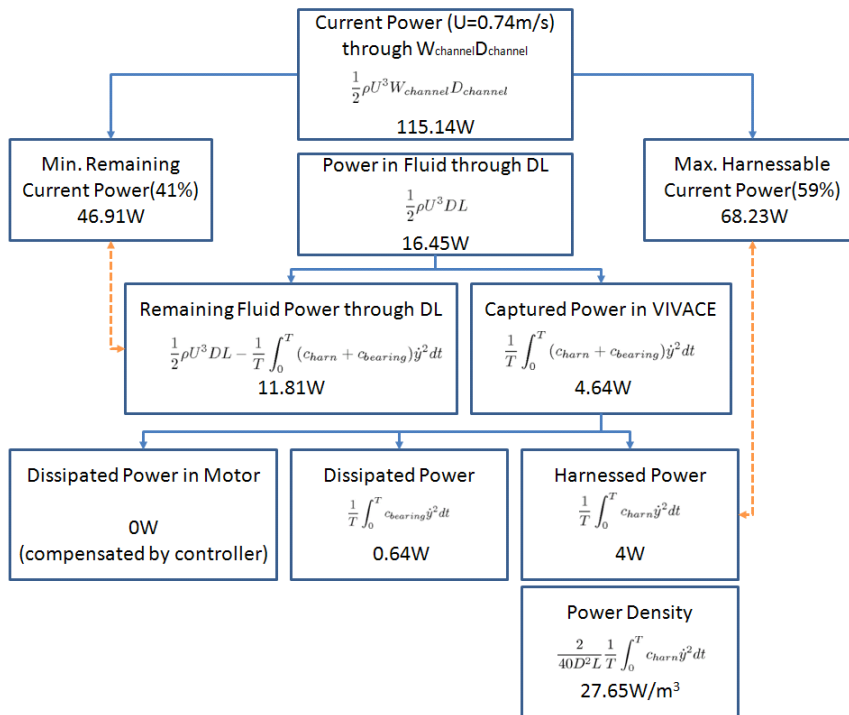


Figure A-10. Power chart for  $U=0.74$  m/s

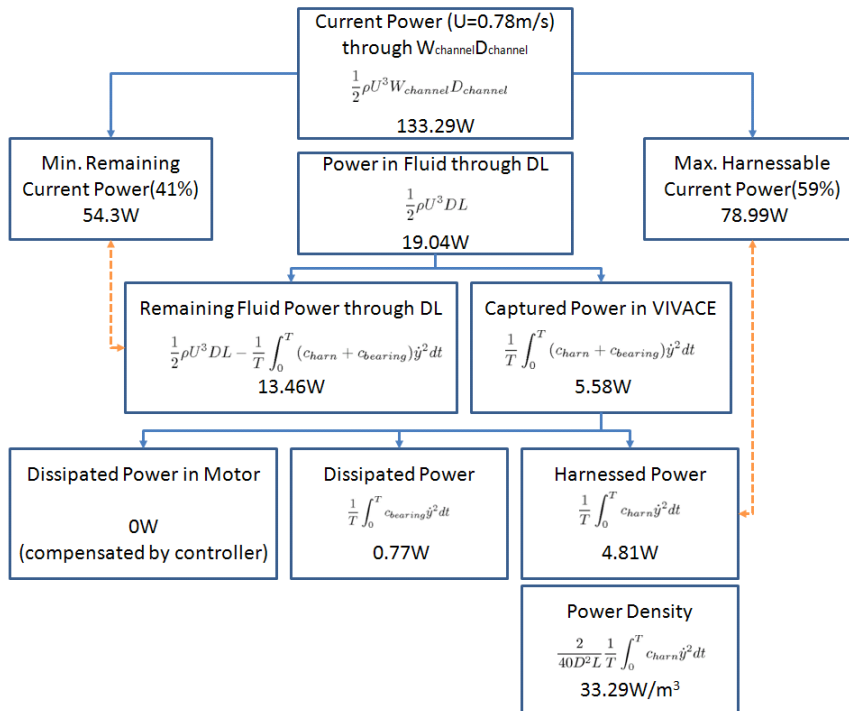


Figure A-11. Power chart for  $U=0.78$  m/s

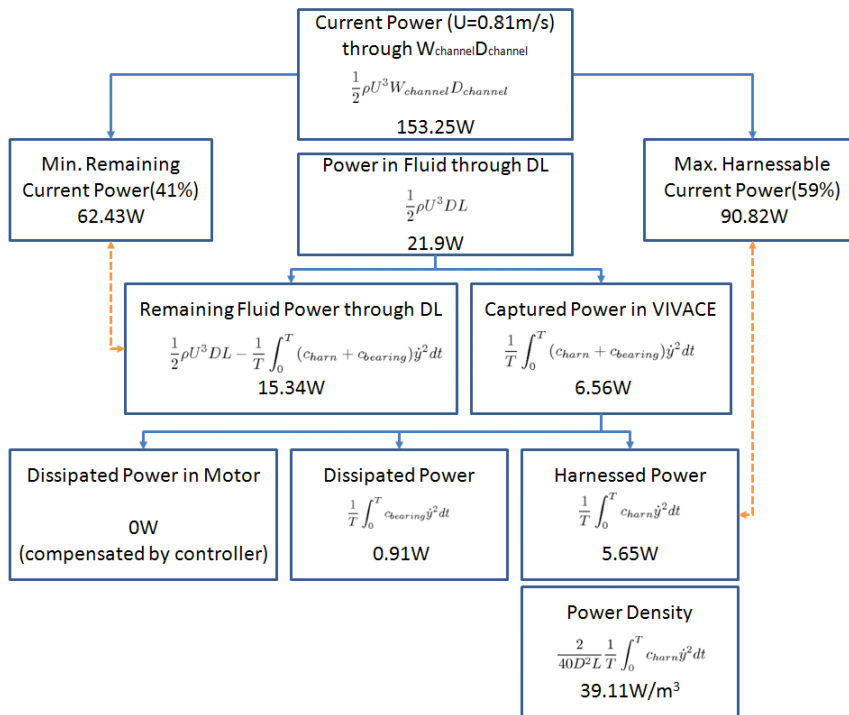


Figure A-12. Power chart for  $U=0.81$  m/s

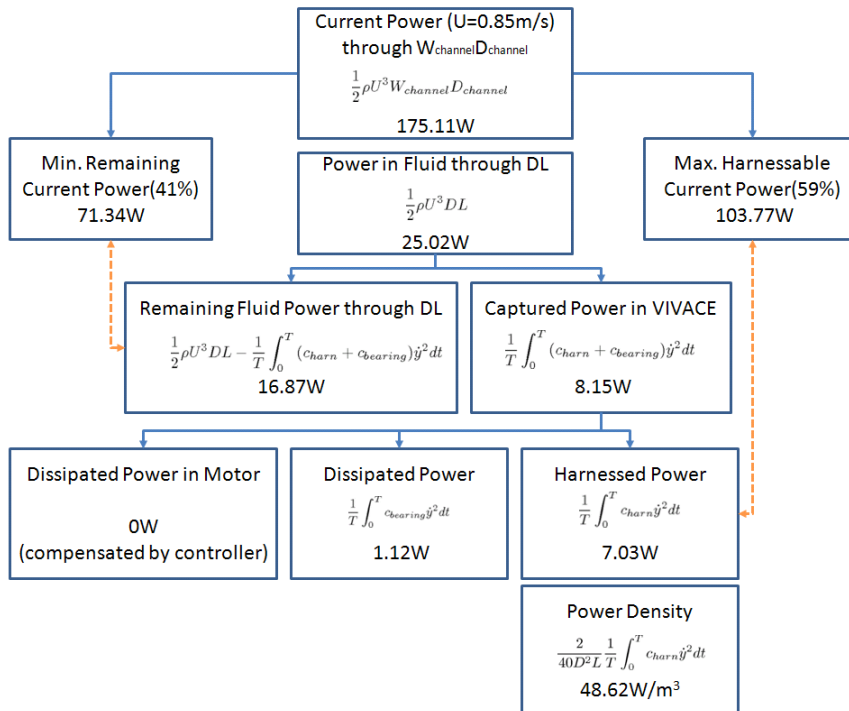


Figure A-13. Power chart for  $U=0.85$  m/s

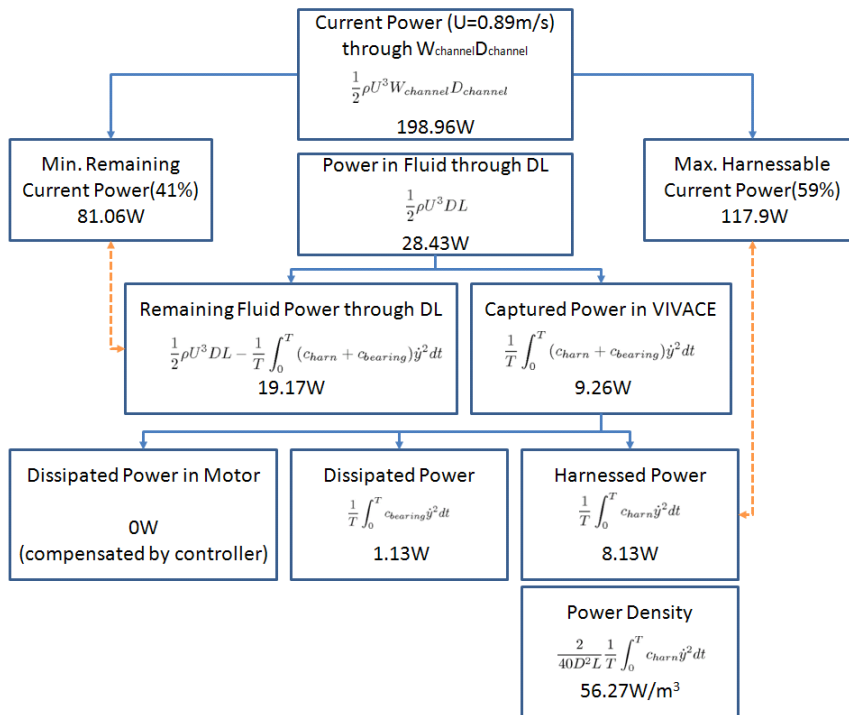


Figure A-14. Power chart for  $U=0.89$  m/s

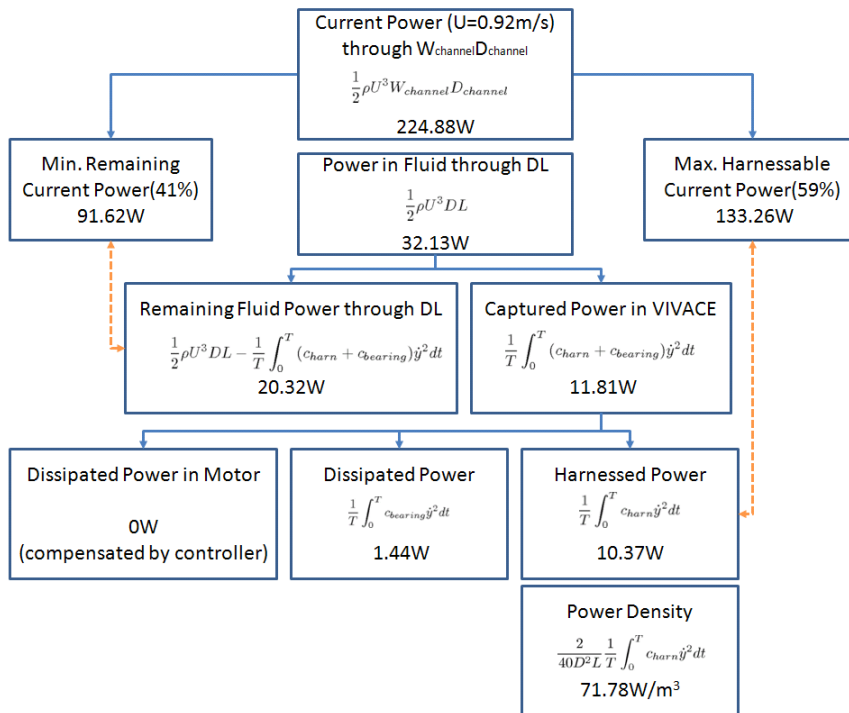


Figure A-15. Power chart for  $U=0.92$  m/s

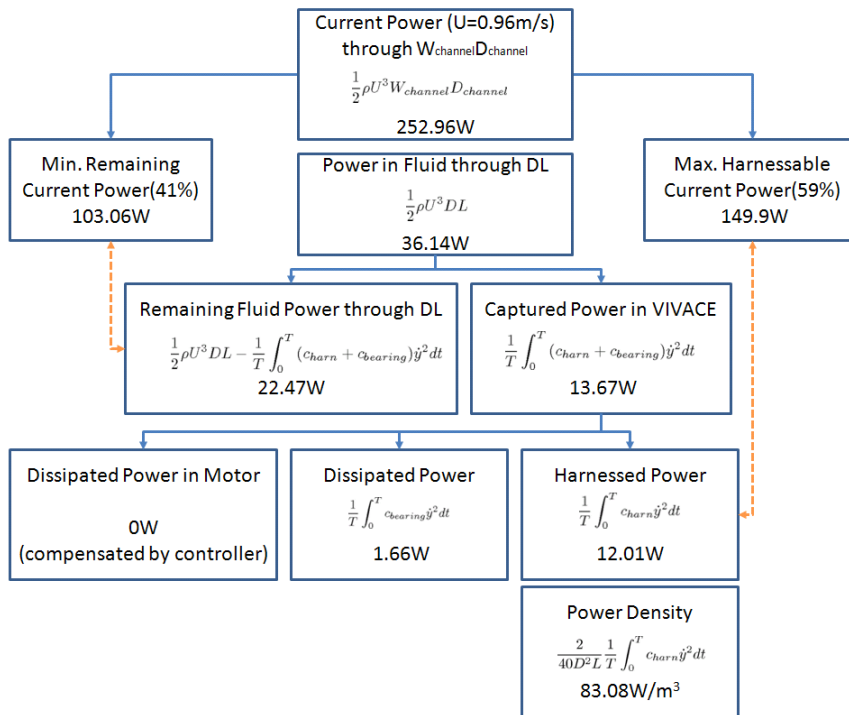


Figure A-16. Power chart for  $U=0.96$  m/s

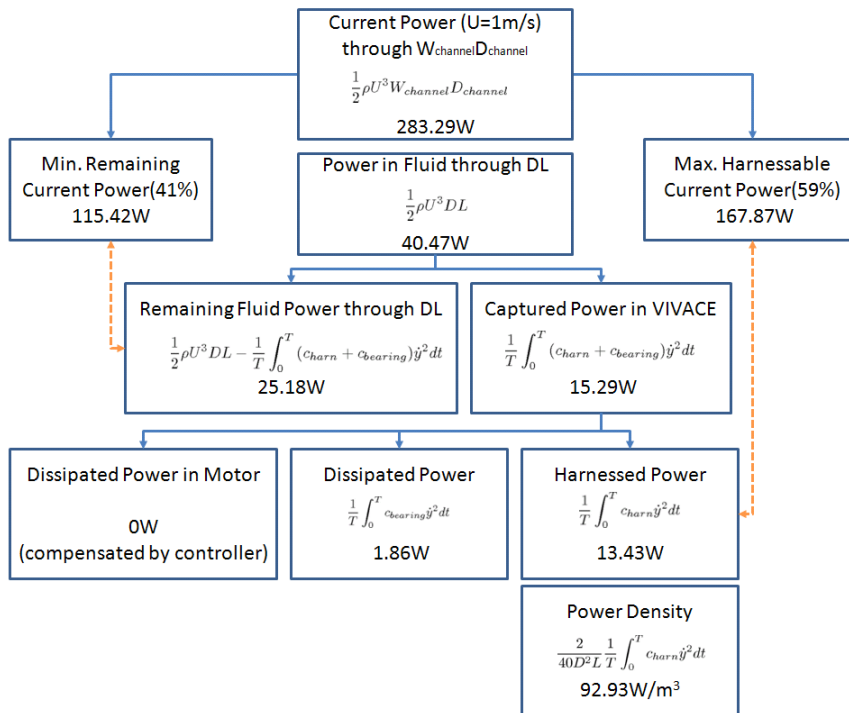


Figure A-17. Power chart for  $U=1$  m/s

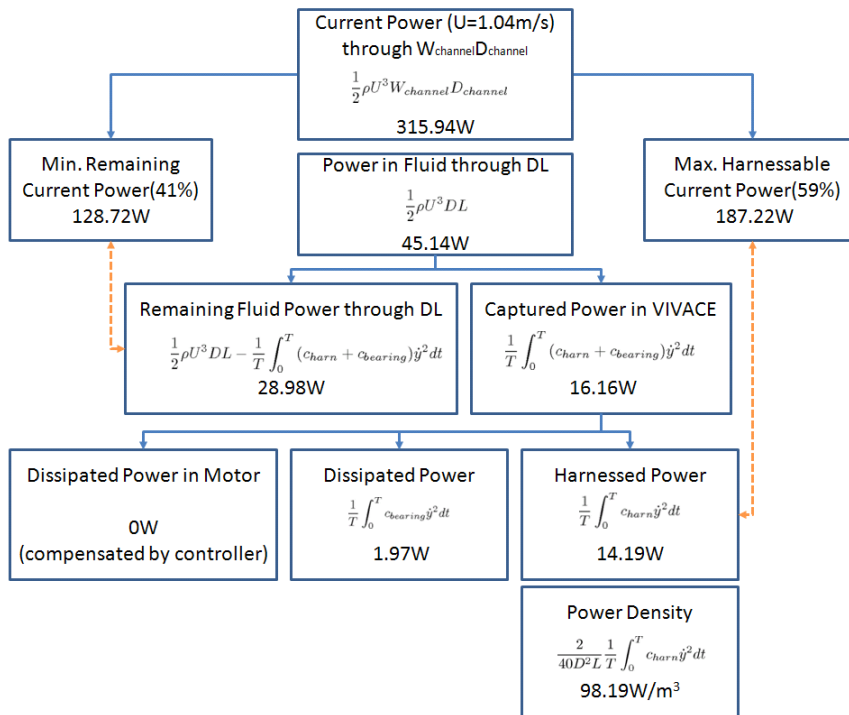


Figure A-18. Power chart for  $U=1.04$  m/s

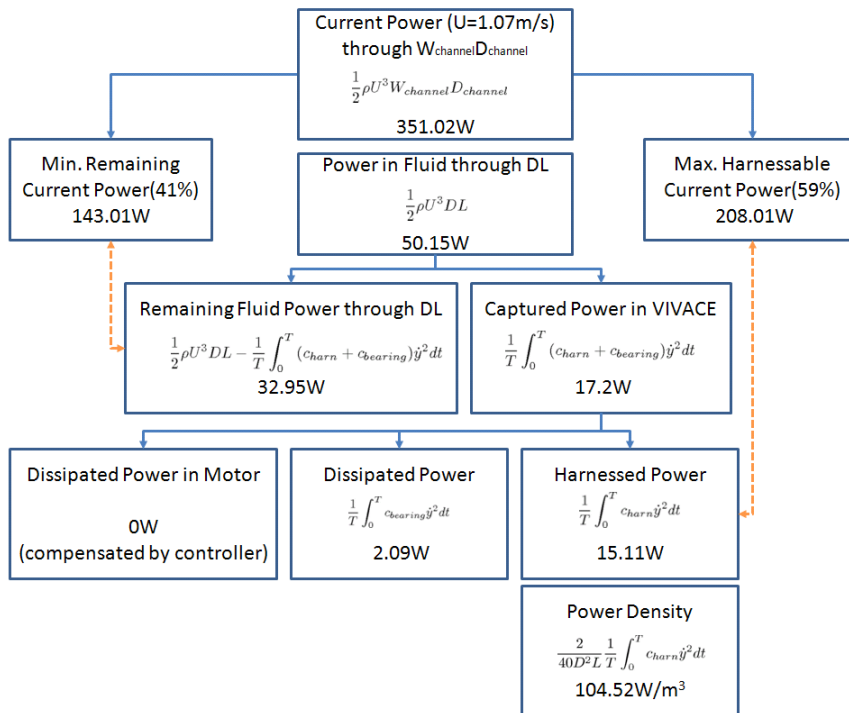


Figure A-19. Power chart for  $U=1.07$  m/s

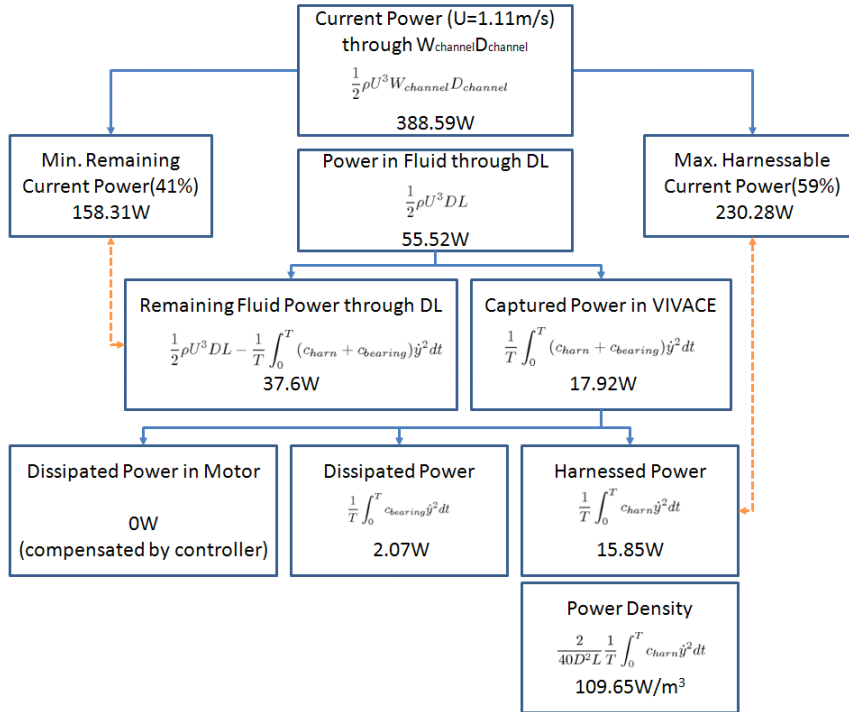


Figure A-20. Power chart for  $U=1.11$  m/s



## REFERENCES

- Bedard, R., Previsic, M., Siddiqui, O., Hagerman, G. and Robinson, M. (2005). Final Survey and Characterization Tidal In Stream Energy Conversion (TISEC) Devices, EPRI-TP-004 NA Report November 9, 2005.
- Bernitsas, M. M. and Raghavan, K. (2005a). Fluid motion energy converter. United States Patent and Trademark Office Serial No. 11/272,504.
- Bernitsas, M. M. and Raghavan, K. (2005b). Fluid motion energy converter. International Patent Application Serial No. PCT/US05/040773.
- Bernitsas, M. M. and Raghavan, K. (2007). Enhancement of vortex induced forces & motion through surface roughness control. U. S. P. a. T. O. Provisional Patent Application.
- Bernitsas, M. M. and Raghavan, K. (2008). "Reduction/Suppression of VIV of Circular Cylinders through Roughness Distribution at  $8 \cdot 10^3 < \text{Re} < 1.5 \cdot 10^5$ ." Journal of Offshore Mechanics and Arctic Engineering-Transactions of the Asme.
- Bernitsas, M. M., Raghavan, K. and Maroulis, D. (2007a). Effect of Free Surface on VIV for Energy Harnessing at  $8 \cdot 10^3 < \text{Re} < 1.5 \cdot 10^5$ . Proceedings of the 26th International Conference on Offshore Mechanics and Arctic Engineering (OMAE' 07), San Diego, California.
- Bernitsas, M. M., Raghavan, K., Ben-Simon, Y. and Garcia, E. M. H. (2008). "VIVACE (vortex induced vibration aquatic clean energy): A new concept in generation of clean and renewable energy from fluid flow." Journal of Offshore Mechanics and Arctic Engineering-Transactions of the Asme **130**(4): 041101-15.
- Bernitsas, M. M., Ben-Simon, Y., Raghavan, K. and Garcia, E. M. H. (2009). "The VIVACE Converter: Model Tests at High Damping and Reynolds Number Around  $10^5$ ." Journal of Offshore Mechanics and Arctic Engineering-Transactions of the Asme **131**(1): 1-13.
- Bishop, R. E. D. and Hassan, A. Y. (1964). "The lift and drag forces on a circular cylinder oscillating in a flowing fluid." Proceedings of the Royal Society (London) **277**: 51-75.
- Blevins, R. D. (1990). Flow-Induced Vibration, Van Nostrand Reinhold Co, NY.
- Carberry, J. (2002). Wake States of a Submerged Oscillating Cylinder and of a Cylinder Beneath a Free-Surface. Clayton, Monash University, Australia.

- Cavanagh, J. E., Clarke, J. H. and Price, R. (1993). Ocean Energy Systems. Renewable Energy: Sources For Fuels And Electricity. T. B. Johansson, H. Kelly, A. K. N. Reddy and R. Williams. Washington/London, Island Press: 513-548.
- Clark, R. O. (1999). Apparatus for generating electricity from flowing fluids. USPTO. **US Pat. 6153944**.
- Cuevas, S., Smolentsev, S. and Abdou, M. A. (2006). "On the flow past a magnetic obstacle." Journal of Fluid Mechanics **553**: 227-252.
- Feng, C. C. (1968). The measurements of vortex-induced effects in flow past a stationary and oscillating circular and D-section cylinders, University of British Columbia.
- Franklin, G. F., Powell, J. D. and Workman, M. L. (1998). Digital control of dynamic systems. Menlo Park, Calif., Addison-Wesley.
- Gopalkrishnan, R. (1993). Vortex induced forces on oscillating bluff cylinders. Department of Ocean Engineering, Massachusetts Institute of Technology.
- Govardhan, R. (2000). Vortex Induced Vibration of Two and Three Dimensional Bodies. Ithaca, Cornell University.
- Govardhan, R. and Williamson, C. H. K. (1999). "Modes of vortex formation and frequency response for a freely-vibrating cylinder." Journal of Fluid Mechanics.
- Govardhan, R. and Williamson, C. H. K. (2002). "Resonance forever: Existence of a critical mass and an infinite regime of resonance in vortex-induced vibration." Journal of Fluid Mechanics **473**(473): 147-166.
- Gowda, B. H. L. and Deshkulkarni, K. P. (1988). "Interference Effects on the Flow-Induced Vibrations of a Circular-Cylinder in Side-by-Side and Staggered Arrangement." Journal of Sound and Vibration **122**(3): 465-478.
- Hover, F. S., Miller, S. N. and Triantafyllou, M. S. (1997). "Vortex-induced vibration of marine cables: Experiments using force feedback." Journal of Fluids and Structures **11**(3): 307-326.
- Hover, F. S., Techet, A. H. and Triantafyllou, M. S. (1998). "Forces on oscillating uniform and tapered cylinders in crossflow." Journal of Fluid Mechanics **363**: 97-114.
- Huera-Huarte, F. J. and Bearman, P. W. (2009). "Wake structures and vortex-induced vibrations of along flexible cylinder-Part 1: Dynamic response." Journal of Fluids and Structures **25**(6): 969-990.
- Jauvtis, N. and Williamson, C. H. K. (2003). "Vortex-induced vibration of a cylinder with two degrees of freedom." Journal of Fluids and Structures **17**(7): 1035-1042.

- Johnson, C. T. and Lorenz, R. D. (1992). "Experimental identification in precise, position controlled mechanisms." IEEE transactions on industry applications **28**(6): 1392-1398.
- Karnopp, D. (1985). "Computer-Simulation of Stick-Slip Friction in Mechanical Dynamic-Systems." Journal of Dynamic Systems Measurement and Control-Transactions of the Asme **107**(1): 100-103.
- Khalak, A. and Williamson, C. H. K. (1999). "Motions, Forces and Mode Transitions in Vortex-Induced Vibrations at Low Mass-Damping." Journal of Fluids and Structures **13**(7-8): 813-851.
- Klamo, J. T., Leonard, A. and Roshko, A. (2005). "On the maximum amplitude for a freely vibrating cylinder in cross-flow." Journal of Fluids and Structures **21**(4): 429-434.
- Kubo, T., Anwar, G. and Tomizuka, M. (1986). Application of nonlinear friction compensation to robot arm control. Robotics and Automation, University of California, Berkeley, California.
- Ljung, L. (1999). System Identification: Theory for the User. NJ, Prentice Hall.
- Marine Turbines. <http://www.marineturbines.com/home.htm>
- Morse, T. L. and Williamson, C. H. K. (2009). "Prediction of vortex-induced vibration response by employing controlled motion." Journal of Fluid Mechanics **634**: 5-39.
- Norberg, C. (1994). "An Experimental Investigation of the Flow Around a Circular Cylinder - Influence of Aspect Ratio." Journal of Fluid Mechanics **258**: 287-316.
- Ogata, K. (1995). Discrete-time control systems. Englewood Cliffs, N.J., Prentice Hall.
- Pontes, M. T. and Falcao, A. (2001). Ocean energies: Resources and utilization. Proceedings of 18th WEC Congress, Buenos Aires.
- Price, S. J., Sumner, D., Smith, J. G., Leong, K. and Paidoussis, M. P. (2002). "Flow visualization around a circular cylinder near to a plane wall." Journal of Fluids and Structures **16**(2): 175-191.
- Raghavan, K. and Bernitsas, M. M. (2008). "Enhancement of High Damping VIV through Roughness Distribution for Energy Harnessing at  $8 \cdot 10^3 < Re < 1.5 \cdot 10^5$ ." Journal of Offshore Mechanics and Arctic Engineering-Transactions of the Asme.
- Raghavan, K., Bernitsas, M. M. and Maroulis, D. (2007). Effect of Reynolds Number on Vortex Induced Vibrations. *IUTAM Symposium*, Hamburg, Germany.
- Raghavan, K., Bernitsas, M. M. and Maroulis, D. (2007b). "Effect of Bottom Boundary on VIV for Energy Harnessing at  $8 \cdot 10^3 < Re < 1.5 \cdot 10^5$ ." Journal of Offshore Mechanics and Arctic Engineering-Transactions of the Asme **131**(2): 1-13.

- Sarpkaya, T. (1979). "Vortex-induced oscillations: A selective review." Journal of Applied Mechanics **46**(2): 241-258.
- Sarpkaya, T. (2004). "A critical review of the intrinsic nature of vortex-induced vibrations." Journal of Fluids and Structures **19**(4): 389-447.
- Schiller, L. and Linke, W. (1933). Pressure and Frictional Resistance of a Cylinder at Reynolds Numbers 5000 to 40000, National Advisory Committee Aeronautics, Technical Memorandum.
- Sheridan, J., Lin, J. C. and Rockwell, D. (1995). "Metastable states of a cylinder wake adjacent to a free surface." Physics of Fluids **7**(9): 2099-2101.
- Sumer, B. M. and Fredsøe, J. (1997). "Hydrodynamics around cylindrical structures." Hydrodynamics Around Cylindrical Structures.
- Szepessy, S. and Bearman, P. W. (1992). "Aspect ratio and end plate effects on vortex shedding from a circular cylinder." J. FLUID MECHANICS **234**: 191-217.
- Technomare (1996). Wave Energy Project Results: the Exploitation of Tidal Marine Currents. Non-Nuclear Energy R&D Component, EU JOULE contract.
- Thorpe, T. W. (1998). "'An Overview of Wave Energy Technologies'." An Overview of Wave Energy Technologies.
- Walker, D. T., Lyzenga, D. R., Ericson, E. A. and Lund, D. E. (1996). "Radar backscatter and surface roughness measurements for stationary breaking waves." Proceedings of the Royal Society - Mathematical, Physical and Engineering Sciences (Series A) **452**(1952): 1953-1984.
- WaveNet (2003). Results from the work of the European Thematic Network on Wave Energy, European Community.
- WEC (2001). Survey of Energy Resources. London, World Energy Council.
- Williamson, C. H. K. and Roshko, A. (1988). "Vortex formation in the wake of an oscillating cylinder." Journal of Fluid and Structure **2**(4, Jul. 1988): 355-381.
- Williamson, C. H. K. and Govardhan, R. (2004). "Vortex-induced vibrations." Annual review of fluid mechanics. Vol.36 2004: 413-55.
- WMCE (2003). Ocean Energy Systems, Status and Research and Development Priorities Wave and Marine Current Energy.
- Xiros, N. I. (2002). Robust Control of Diesel Ship Propulsion. London, Springer.
- Yoshitake, Y., Sueoka, A., Yamasaki, M., Sugimura, Y. and Ohishi, T. (2004). "Quenching of vortex-induced vibrations of towering structure and generation of electricity using Hula-Hoops." Journal of Sound and Vibration **272**(1-2): 21-38.

Zdravkovich, M. M. (1990). "Conceptual Overview of Laminar and Turbulent Flows Past Smooth and Rough Circular-Cylinders." Journal of Wind Engineering and Industrial Aerodynamics **33**(1-2): 53-62.